UNIVERSITÀ POLITECNICA DELLE MARCHE

FACOLTÀ DI INGEGNERIA

Corso di Laurea Magistrale in Biomedical Engineering

Tesi di Laurea:

Non-Invasive Small Vessels Imaging of Human Thyroid Using Motion-Corrected Power Doppler Imaging

Relatore:

Lorenzo Scalise, PhD

Candidata:

Eleonora Scardecchia

Correlatori:

Mostafa Fatemi, PhD

Azra Alizad, MD

Anno Accademico 2019-2020

Abstract

Imaging of microvascular pathways plays a significant role in detection of metastasis of cancerous masses in human thyroid. Contrast-free ultrasound based Doppler blood flow imaging is potentially useful to reduce the large number of benign findings of suspicious thyroid nodules. However, Doppler imaging of thyroid nodules is particularly demanding because the large motion due to its proximity with the carotid artery can impact both tissue clutter suppression and power Doppler (PD) integration. To address these issues, thyroid motion was estimated as components of axial and lateral displacements using a two-dimensional (2D) normalized cross correlation (NCC) - based speckle tracking of the Doppler ensemble, prior to singular value decomposition (SVD) clutter filtering. Moreover, we evaluated the feasibility of using non-redundant Doppler ensembles to track small-inter frame displacements, whose quantitative estimation is quite challenging because of the poor lateral resolution of ultrasonic images. This hypothesis was corroborated by applying the motion correction technique on phantom and *in vivo* data. Correlation matrices were used throughout the analysis as performance indices. Increased values of mean correlation coefficient after motion correction in phantom instances guaranteed the efficiency of the proposed optimized technique in detecting small inter-frame displacements and encouraged its validation on the *in vivo* dataset. The results from the in vivo study proved that the motion-corrected PD images importantly improved the visualization of the small vessels. In fact, motion induced signal distortion, blurring and appearance of shadow vessel were considerably reduced upon motion correction and noise suppression, without affecting vessel morphology.

Index

Introduction

The present study was conducted in the Ultrasound Research Department at Mayo Clinic in Rochester, MN and aimed to the optimization of the motion correction procedure in contrast-free power Doppler (PD) ultrasound microvascular imaging of human thyroid.

In United States there are over 50.000 new cases of thyroid cancer every year, with a likelihood of 3:1 for females to males *(Saslow, 2007)*. Fine needle aspiration (FNA) has been accepted as a first-line screening test for patients with suspicious thyroid nodules. 60-80% of thyroid cancer diagnosis by FNA biopsies result in benign findings, which unreasonably causes significant physical and financial burden to both patients and health care system *(Frates, 2005)*.

Several studies have exploited the potential of using non-invasive PD ultrasound to detect thyroid malignancy by assessing and monitoring intranodular and peripheral vascularity *(Appetecchia, 2006; Brunese, 2008; Cerbone, 1999; Bae, 2007; Lu, 2017)*.

In PD applications clutter suppression remains a crucial and challenging step in visualizing blood flow. Clutter is usually rejected by high-pass filtering of the slow-time ensemble under the temporal assumption that tissue signal and blood flow signal have non-overlapping spectra centered on the zero frequency and the Doppler frequency, respectively. However, in presence of motion tissue frequencies could be equal or even higher than those of slow blood flow *(Nayak, 2017)*. This can limit the visualization of small vessels blood flow, which can be of low frequency (or velocity) because of small vessel diameter *(Nayak, 2017)*.

Thus, non-invasive imaging of small blood vessels in thyroid appears to be particularly challenging because of the large pulsating motion of the close carotid artery, which is associated with stresses due to blood pressure, blood flow, and tethering to the surrounding tissue. Stresses result in strains in three directions which correspond to changes in the radius and axial length of the vessel, and movement out of the B-mode section. These physiological changes combined with sonographer hand motion and

patient shifting can impact clutter suppression and coherent integration of the Doppler signal, degrading then the visualization of the underlying microvasculature. Thus, FNA is still preferred in clinical settings *(Nayak, 2017)*.

Demanè et al. demonstrated that spatio-temporal singular value decomposition clutter filtering of ultrasonic data acquired at ultrafast frame rate can significantly improve detection of slow blood flow and rejection of moving tissues *(Demanè, 2015)*. Singular value decomposition (SVD) uses both spatial and temporal information to differentiate between tissue and blood flow. Specifically, ultrafast acquisition enables tissue components to acquire low rank in the Casorati matrix because of its higher spatial and temporal coherence compared with the incoherent blood flow, and thus, a singular value (SV) rank based thresholding can be successfully used for clutter suppression.

Nayak et al. demonstrated that large physiological motion and sonographer hand motion can significantly reduce the covariance of the spatiotemporal matrix, leading to suboptimal clutter rejection *(Nayak, 2018)*. Motion increases the rank of the tissue components, and therefore, a higher SV threshold must be used to efficiently suppress tissue clutter. This can reduce the sensitivity of detecting small vessels *(Nayak, 2018)*. Furthermore, Nayak et al. showed that even if tissue clutter is completely rejected in presence of motion, estimation of the cumulated PD signal from the motion affected clutter filtered data can be demanding because of the miss-registration of the ultrasound frames in the Doppler ensemble *(Nayak, 2018)*. Specifically, PD signal is computed from coherent integration of the clutter filtered signal. In presence of motion, signal incoherency due to spatial miss-registration of the ultrasound frames can significantly reduce image quality. Moreover, imaging of blood flow in small vessels – usually characterized by low intensity back-scatter signals, can be particularly unreliable since motion can definitely corrupt its contribution because of incoherent integration *(Nayak, 2018)*. Although high frame rate imaging partially mitigate the impact of motion on small vessel, angular compounding of the ultrasound frames - required to increase the signal to noise ratio (SNR) of plane wave imaging - reduces the frame rate by up to an order of magnitude, eventually leading to increased motion between successive frames *(Nayak, 2018)*. Visualization of small vessel blood flow could be improved by injecting micro-

bubbles based contrast agents in the blood stream. However, this yields to increased complexity, cost and invasiveness.

To address these weaknesses, Nayak et al. introduced a first-order rigid body based motion correction technique. A two-dimensional (2D) normalized cross-correlation (NCC) - based speckle tracking technique was used to estimate tissue displacements, which were subsequently used for motion correction. Motion correction was performed on the clutter filtered ensemble prior to PD computation *(Nayak, 2018)*. Quantitative assessment of motion correction performance was accomplished using a correlation matrix, named *Motion Matrix* (MM) *(Nayak, 2018)*. Initial results on ten human subjects with thyroid nodules suspicious of malignancy proved the efficacy of using motion corrected PD imaging for visualization and detection of small vessel blood flow, without any use of contrast agents. Those promising and encouraging preliminary results suggested and warrant further developments and more *in vivo* validation in moving tissue and organs.

Objectives

Ultrafast Doppler, based on unfocused wave transmissions, allows the acquisition of wide 2D fields of view at a very high frame rates that, in the framework of clutter rejection filters, enables to overcome severe limitations of conventional focused transmissions. However, a large ensemble unavoidably results in small inter-frame displacements whose quantitative estimation could be challenging because of poor lateral resolution capabilities of ultrasonic images.

We hypothesized that small inter-frame displacement tracking can be enhanced by properly reducing the ultrafast Doppler ensemble and pairing Doppler frames. Specifically, in case of small amounts of motion, the displacement between two consecutive frames is insignificant, and thus, a large frame interval is needed to capture distortions and correct. Conversely, in presence of huge amounts of motion, the displacement between consecutive frames is too large to form a cohesive image, and thus, a small frame interval is preferred.

Theory

Ultrasound Imaging

1.1 Introduction

Among medical imaging modalities, such as CT and MRI, ultrasound imaging has emerged as a disruptive technology in the medical device field because of its real time capabilities, non-ionizing properties and low cost. Ultrasound has significantly impacted clinical segments within radiology, obstetrics and cardiology allowing observation of the morphology of living organs as well as functional imaging, such as blood flow imaging and evaluation of the cardiac function *(Bercoff, 2011)*.

Historically, several advances have made possible the establishment of ultrasound as a powerful clinical imaging device. The key innovation that launched the modality in the 1960s was the real time imaging capability through mechanical scanning *(Bercoff, 2011)*. Then, multichannel systems with electronic control of transducer arrays and flow analysis tools were developed in the 1970s and in the 1980s, respectively. Later, in the 1990s the introduction of real time compounding techniques and harmonic imaging has guaranteed significant improvements in image quality *(Bercoff, 2011)*. Clearly, the introduction of pioneering concepts on commercially available platforms systematically occurs in conjunction with the growth of a new technology: for example, real time imaging was prompted by microprocessors development, Doppler modes were triggered by digital signal processing chips with enough dynamics to detect, at the same time, very weak blood signal and strong tissue echoes *(Bercoff, 2011)*. Low cost Analog to Digital (A/D) converters have led to fully digital systems, increasing the quality of the information delivered. Harmonic imaging was triggered by large bandwidth transducers, allowing reception of the signal at twice the transmit frequency *(Bercoff, 2011)*. Early in 21th century, extensive miniaturization has led to the introduction of high performances portable devices, creating new promising markets for ultrasound *(Bercoff, 2011)*. Currently, a new technological improvement is ongoing with the onset of massive parallel computing capabilities. Along with multicore architecture CPU's, new graphical processing units (GPU) enable parallel processing on thousands of channels simultaneously *(Bercoff,*

2011). Basically, instead of increasing integrated hardware processing channels, all the processing is performed by the software unit (CPU and GPUs). The concept of processing channels disappears and the system is able to compute in parallel as many channels as required by the acquisition *(Bercoff, 2011)*. This architecture paves a new way to perform ultrasound imaging: ultrafast ultrasound imaging *(Bercoff, 2011)*.

1.2 Conventional Ultrasound Imaging

Ultrasound imaging is usually performed by sequential insonification of the medium using focused beams. Each beam allows the reconstruction of one image line. A 2D image is usually made of a few tens of lines (*figure 1.1*), (Bercoff, 2011).
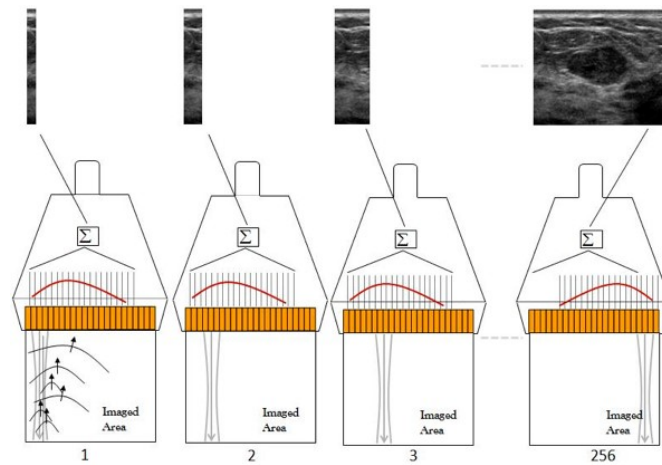
Figure 1.1 Conventional imaging acquisition process.

The frame rate of the imaging mode is set by the time required to transmit a beam, receive and process the backscattered echoes from the medium and repeat that for all the lines of the image.

For a conventional 2D image, the time to build an image is:

$$T_{image} = \frac{2 * Z * N_{lines}}{c} \tag{1.1}$$

where Z is the image depth, c the speed of ultrasound waves assumed constant (1540 m/s) and N_{lines} the number of lines in the image *(Bercoff, 2011)*. The maximum frame rate that can be reached with this technique is:

$$FR_{max} = \frac{1}{T_{image}} \tag{1.2}$$

1.3 Increasing Ultrasound Imaging Frame Rate

Limitations of the conventional approach appear as soon as higher frame rates are required. Most current systems have multiline capabilities: for each transmit beam, several lines (2 to 16) are computed. Multiline processing can be used either to increase the frame rate either to increase the number of lines computed per image *(Bercoff, 2011)*.

1.4 Ultrafast Imaging

With or without multiline capabilities, current ultrasound systems are built on serialized architecture and images are reconstructed sequentially from several equivalent transmits. Ultrafast imaging breaks this paradigm *(Bercoff, 2011)*. An ultrafast imaging system is able to compute in parallel as many lines are requested and is therefore capable of computing a full image from one single transmit whatever the size and the characteristics of the image *(Bercoff, 2011)*. In such a system the image frame rate is no longer limited by the number of lines reconstructed but by the time of flight of a single pulse to propagate in the medium and get back to the transducer *(Bercoff, 2011)*.

Table 1 shows typical frame rates for different ultrasound clinical applications using conventional and ultrafast architecture.

Table 1. Example of typical frame rates in different clinical applications for conventional and ultrafast architecture.

Application	Typical Imaging Depth	Conventional Architecture	Ultrafast Architecture
Abdominal Imaging	20 cm	20 Hz	3800 Hz
Cardiac Imaging	15 cm	150 Hz	5000 Hz
Brest Imaging	5 cm	60 Hz	15000 Hz

To achieve ultrafast imaging, the image computation must be performed on a fully parallelized platform, typically a software-based platform. There are two technologically changeling aspects to building a software-based platform *(Bercoff, 2011)*:

- As row (non beamformed) radio frequency signals (RF) are directly transferred to the PC, the data rate required to perform real time imaging is about several GigaBytes/s;

- The processing unit needs to be powerful enough to ensure real time imaging.

To speed up processing algorithms powerful GPUs are used. The ultrafast architecture leverages this processing power by combining it with fast numerical links capable of transferring huge volume of data to these units *(Bercoff, 2011)*. This combination allows the shift of the beamforming process from hardware to software, enabling full parallelization of ultrasound image computation *(Bercoff, 2011)*. *Figure 1.2* shows a comparison between the architecture of an ultrafast system and a conventional system.
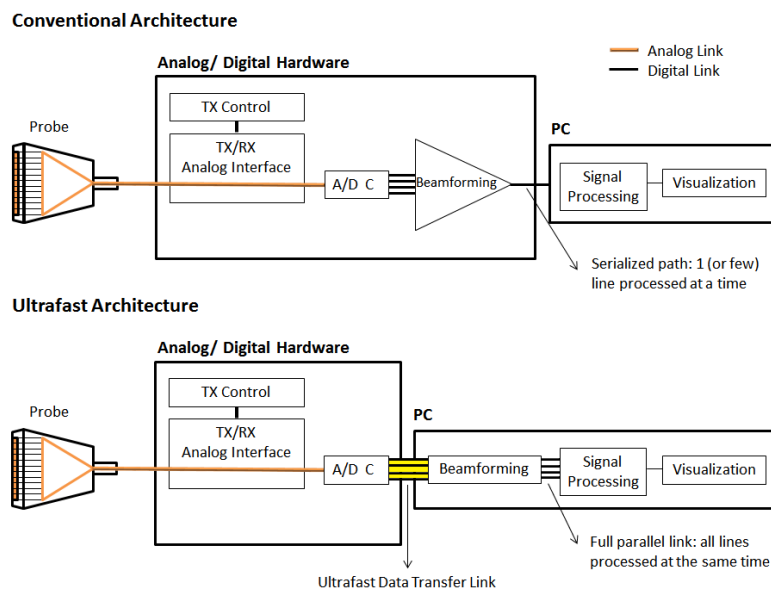
Figure 1.2 As beamforming is performed in software, full parallelization of image formation can be performed. Each insonification can therefore lead to a full image. (TX refers to 'Transmit', RX to 'Receive').

1.5 The Single Plane Wave Imaging Mode

The following section refers to *Montaldo, 2008*.

A typical configuration of ultrasonic imaging system is shown in *figure 1.3(a)*. A linear array made of n_t transducers (typically 128) is placed directly in contact with the medium of interest. The *x* direction is parallel to the array, *z* is the depth direction in the imaging medium.
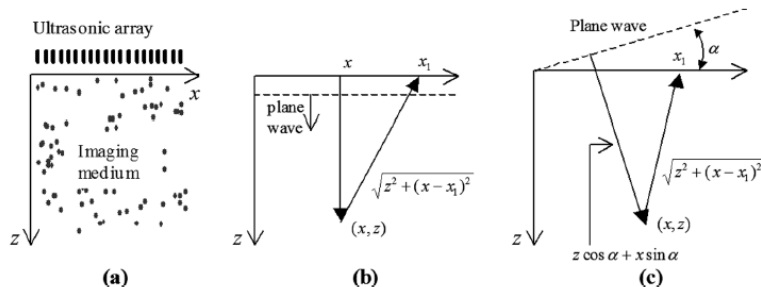
Figure 1.3 (a) Axis convention. (b) Time delays for a plane wave insonification. (c) Time delays for a plane wave of angle α. *(Montaldo, 2008).*

A plane wave is generated by applying flat delays on the transmit elements of the ultrasound probe. The general wave will insonify the whole area of interest *(figures 1.4 and 1.5(a))*. Then, this wave is backscattered by the heterogeneities of the medium and the array receives the echo signals *RF(x_1, t)*; *(figure 1.5(b))*. As the transmit focalization step is removed, the image resolution is obtained only by a parallel processing during the reception mode by adding coherently the echoes coming from the same scatter.
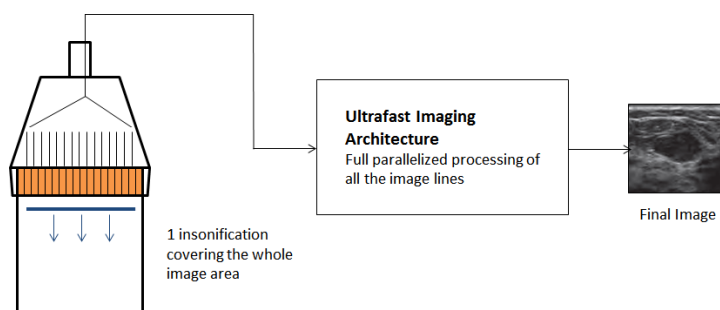
Figure 1.4 A plane wave is sent from a linear transducer and insonifies the whole region of interest. An ultrasound image is computed from this single insonification.
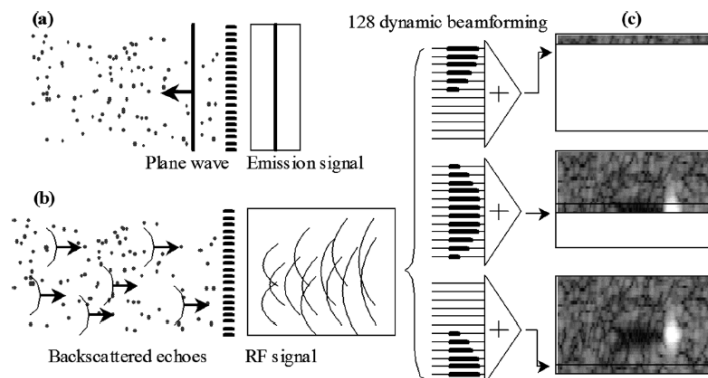
Figure 1.5 (a) The ultrasonic array insonifies the medium using a plane wave transmission. (b) The backscattered RF signals are recorded by the transducer array. (c) The beamforming procedure consists in applying time delays laws and summations to the raw RF signals to focus in the receive mode. Contrary to standard ultrasonography, each line

of the image is calculated using the same RF data set but a different set of time delays *(Montaldo, 2008)*.

For a plane-pulsed wave *(figure 1.3(b))*, the travelling time to the point *(x,z)* and back to a transducer placed in x_1 is:

$$\tau(x_1, x, z) = \frac{\left(z + \sqrt{z^2 + (x-x_1)^2}\right)}{c} \qquad (1.3)$$

where *c* is the speed of sound, assumed to be constant.

Each point *(x,z)* of the image is obtained by delaying the *RF(x_1,t)* signals by *τ(x_1,x,z)* and adding them in the array direction x_1

$$s(x, z) = \int_{x-a}^{x+a} RF(x_1, \tau(x_1, x, z)) dx_1 \qquad (1.4)$$

The aperture *2a* must take into account only the elements that contribute to the signals. It is always minor than the length of the array *L*, and it can be expressed by the *F-number* defined as:

$$F = \frac{z}{2a} \qquad (1.5)$$

The *F*-number depends on the directivity of the array and ideally must be constant in the whole image; typical values are between 1 and 2.

In dynamic beamforming, the delays *τ* are computed at each depth *z* to produce a complete line of the image. The final image is obtained by producing in parallel n_e dynamic beamformings with the same RF data, one for each line of the image *(figure 1.3(c))*.

Plane wave imaging allows the computation of one full ultrasound image per transmit, with a frame rate of nearly 10 kf/s but at the expense of image quality. As shown in *figure 1.6(a)*, the contrast is law. In order to overcome this limitation, several tilted plane waves are sent into the medium and coherently summed to compute a full image.
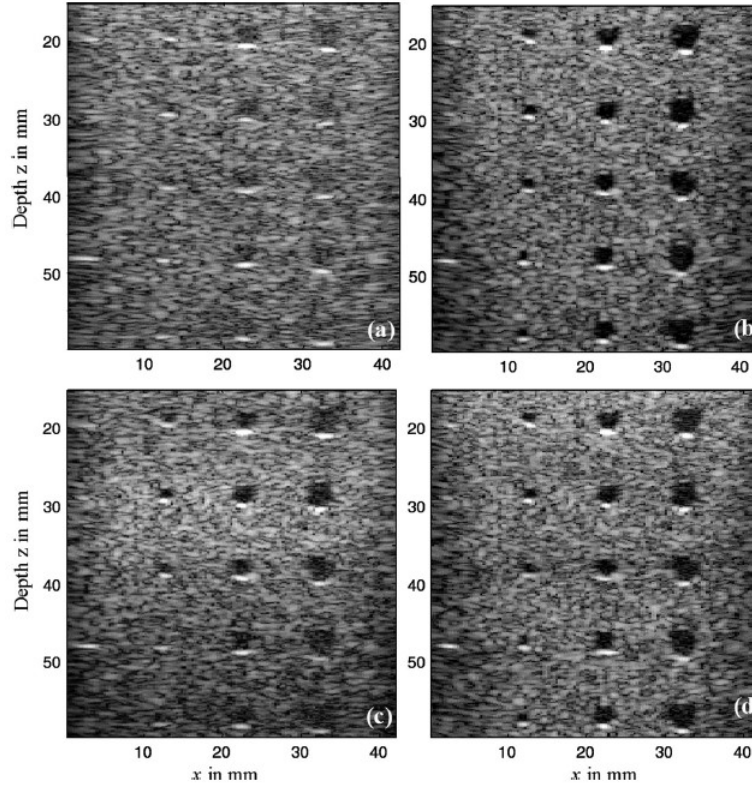
Figure 1.6 (a) B-mode image attained using a single plane wave transmission. (b) Coherent plane wave compound using 71 angles. (c) Standard monofocal image using a single focal depth at 30mm. (d) Multifocal image using 4 successive focal depth. Images produced with a 128-element array of 4.5 MHz, 60% bandwidth, pitch of 0.33 mm, F-number of 1.75 both in emission and reception, the lateral scan is done at λ/2 *(Montaldo, 2008)*.

1.6 The Coherent Plane Wave Compound

If a plane wave is sent with inclination α *(figure 1.3(c))*, the time to reach a point *(x,z)* of the medium is:

$$\tau_{ec}(\alpha, x, z) = \frac{z cos\alpha + x sin\alpha}{c} \tag{1.6}$$

and the time to come back to a transducer placed in x_1 is:

$$\tau_{rec}(\alpha, x, z) = \frac{\sqrt{z^2 + (x - x_1)^2}}{c} \tag{1.7}$$

The total 2-way travel time τ is then:

$$\tau(\alpha, x_1, x, z) = \tau_{ec} + \tau_{rec} \tag{1.8}$$

The image is obtained as described before *(equation 1.4)*, but with the delays from *(equation 1.8) (Montaldo, 2008)*. The image quality can be improved by compounding

coherently images attained with a certain number of plane waves at different angles α_i, i = 1, …, n (figure 1.7) (Montaldo, 2008). Sending n plane waves necessitates more time and reduces the frame rate by a factor n_k (Montaldo, 2008). In *figure 1.6(b)* a coherently compounded image using 71 plane waves with a separation of 0.47° between each angle is shown (Montaldo, 2008). As noticeable, the contrast is higher than that achieved using a single plane wave. *Figure 1.6(c)* shows an image attained with only one focal depth in transmit (Montaldo, 2008). As visible, the image is acceptable only near the transmit focal area. The image quality can be upgraded by using several transmit focal depths. The final image is then obtained by recombining the partial images corresponding to various depths. *Figure 1.6(d)* represents a multifocal image obtained with 4 focal depths; an improvement of the image can be clearly seen when comparing it with the single focus image *(figure 1.6(c))* (Montaldo, 2008). Moreover, the comparison between *figures 1.6(b) and 1.6(d)* shows that the coherent compound approach performs as well as the optimal multifocal image but with frame rates higher than 200 f/s (Montaldo, 2008).
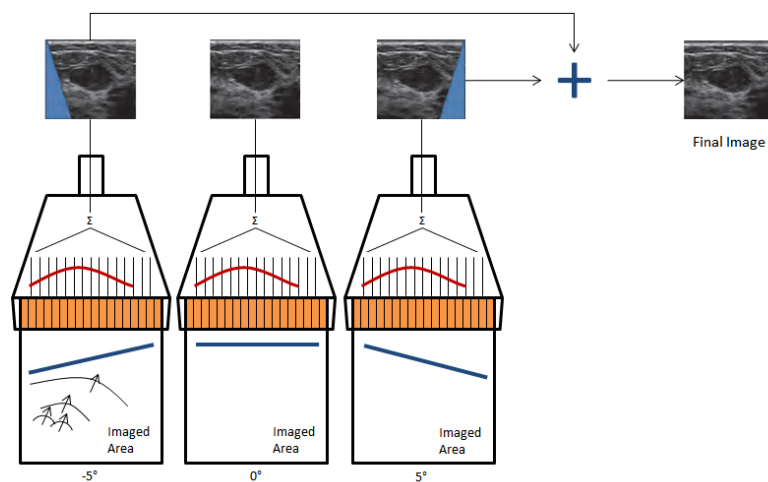
Figure 1.7 Ultrasound image obtained using ultrafast coherent plane wave compound.

As noticed before, the quality of the final ultrasound image is function of the number of angles used to reconstruct it *(figure 1.8)*. There is a tradeoff between the maximum ultrafast frame rate achievable by the mode and the image quality: the higher the number of angles, the better the image quality *(figure 1.8) (Bercoff, 2011)*.
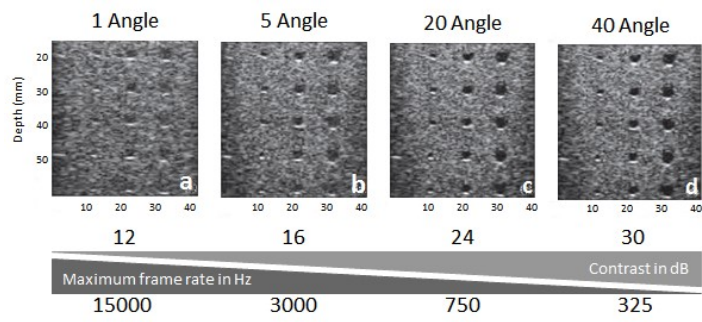
Figure 1.8 Image quality as a function of the number of angles used to compute the final ultrasound image for a 40mm depth image. *(Bercoff, 2011)*.

Doppler Ultrasound

2.1 Introduction

Doppler ultrasound is a powerful imaging modality used to detect, quantify and image blood flow. Doppler ultrasound relies on the later acknowledge "Doppler effect", first postulated in 1842 by the Austrian physicist Christian Andreas Doppler. The Doppler effect describes the change in the observed frequency of a wave when there is relative motion between a sound source and an observer. This change in the observed frequency relative to the transmitted frequency is known as Doppler shift.

The perceived frequency is either greater or less than that transmitted by the source, depending on whatever the source and the listener are moving towards or away from another one. In particular, if the source and the listener are moving towards each other, the observed frequency will be higher than the transmitted one, whereas, if they are moving apart, the perceived frequency will be lower.

In medical ultrasound Doppler shifts occur whenever echo signals are picked up from moving reflectors. In *figure 2.1*, a stationary transducer is sending sound waves to the right and receiving echoes from a reflector. The echo pattern from the reflector differs depending on whether the reflector is stationary or moving. The frequency of echoes from a stationary reflector is the same as that produced by the transducer. Slightly higher frequency echoes result if the reflector moves towards the transducer and slightly lower frequencies occur for reflectors moving away.
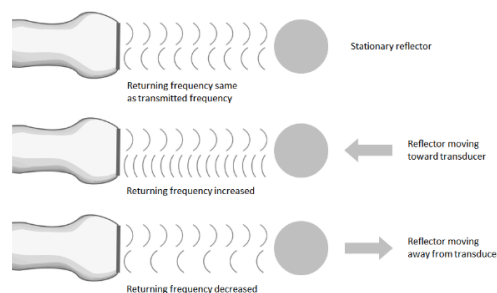

Figure 2.1 Doppler shift in medical ultrasound.

Note that the Doppler effect actually occurs twice in the production of an echo from a moving reflector. First the reflector plays the role of a moving listener as it travels

towards or away from the ultrasound. Therefore, the ultrasound waves the reflector encounters are initially Doppler shifted. Then, the reflector acts as a moving source as it sends echoes back towards the transducer. This results in an additional shift in the frequency of the waves compared to the transmitted frequency.

2.2 Doppler Equation

Doppler equipment is usually used to detect and evaluate blood flow in arteries and veins. A typical setting is shown in *figure 2.2*. The ultrasonic transducer is placed in contact with the skin surface and the ultrasound beam is directed toward the vessel. The beam is at an angle ϑ with respect to the axis of the vessel. Red blood cells flowing in the vessel scatter ultrasound waves, giving rise to echo signals. Because the scatters are moving, the frequency of the return echo signals is Doppler shifted. The Doppler frequency, f_D, and is given by:

$$f_D = f_t - f_r = \frac{2f_t v cos\theta}{c} \tag{2.1}$$

where f_t and f_r are the transmitted and received ultrasound frequencies, respectively, v the reflector velocity, c the speed of sound, and ϑ the angle between the ultrasound beam and the reflector path.

The velocity c and the transmitted frequency f_t are *a priori* known and therefore the reflector velocity can be estimated as follow:

$$v = \frac{kf_D}{cos\theta} \tag{2.2}$$

where k is a known constant given by:

$$k = \frac{c}{2f_t} \tag{2.3}$$

If the velocity is at a normal angle (90-degree) to the beam, the radial component of the velocity is zero and no Doppler shit is observed. Moreover, note that 0-degree Doppler angle corresponds to reflectors moving directly towards the transducer and, a 180-degree Doppler angle corresponds to reflectors moving directly away from the transducer.

In addition, the Doppler equation indicates that the sensitivity of velocity measurement increases with the transmitted frequency f_t. The frequency range actually used in Doppler US applications varies from 2 MHz, typical of transcranial applications where the explored region can cover a depth of 10 cm^2, up to 10-20 MHz, used for high resolution non-

invasive measurements (1-2 mm). The expected measured velocities are typically lower than 1 m/s in the peripheral circulation of a healthy subject, and they are never higher than a few m/s. Accordingly, the detected Doppler shift is generally in the range of a few kHz *(Bjorn A.J. Angelsen, 2000)*.
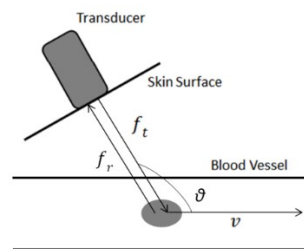
Figure 2.2 Arrangement for detecting Doppler signals from within the vessel.

2.3 Continuous Wave Doppler

An ultrasound beam is continuously transmitted into the tissue with one transducer while the back scattered signal is continuously picked up by another transducer *(figure 2.3)*. Thus, all the moving targets within the overlap of the beams - sample volume - of the dual-transducer assembly are detected. This gives practically no range resolution, but since there is the continuous recording of the return signal, there is also no sampling and frequency aliasing, and no limit on the maximum velocity that can be measured *(Bjorn A.J. Angelsen, 2000)*.
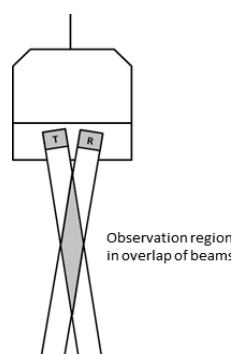
Figure 2.3 CW instrument detects Doppler shifted echoes in the region of overlap between the beams of the transmitting and receiving elements.

2.3.1 Components of a Continuous Wave Doppler System

A diagram of a Continuous Wave (CW) Doppler system is presented in *figure 2.4, A*. The oscillator produces a continuously alternating voltage with a 2 to 10 MHz frequency,

which is applied to the source transducer element *(Kremkau, 2006)*. The ultrasound frequency is determined by the oscillator. The oscillator frequency is set to be equal the operating frequency of the transducer. In the transducer assembly, a separate receiving transducer element produces voltages with frequencies equal to the frequencies of the returning echoes *(Kremkau, 2006)*. If scatter motion is present, the reflected frequency and the transmitted frequency will be different. Thus, Doppler shits are sent through a spectrum analyzer to a spectrum display for visual observation and evaluation. The detector *(figure 2.4, B)* amplifies the echo voltages it received from the receiving element, detects the Doppler shift information in the returning echoes, and determines the sign of the Doppler shift *(Kremkau, 2006)*. Doppler shifts are determined by mixing the returning voltages with the CW voltage from the oscillator. This produces the sum and difference of the oscillator and echo frequencies. The difference is the Doppler shift. The sum is a much higher frequency and is filtered out easily. The difference is equal to zero for echoes returning from stationary structures while it is equal to the Doppler shift for echoes originating from moving structure or flowing blood. Positive and negative shifts indicate motion toward and away from the transducer, respectively. The directional information is provided by the phase quadrature detector. Furthermore, the phase quadrature detector separates Doppler shift voltages into forward and reverse channels. The forward and reverse channel signals are sent to separate loudspeakers, thus, forward and reverse Doppler shifts are heard separately. The signals are also sent to a visual display to show positive and negative Doppler shifts above and below the display baseline, which represents zero Doppler shift. Simpler instruments, such as handheld, non-directional device, yield only an audible output. Analog zero-cross correlation devices provide an instantaneous-average Doppler shift that varies over cardiac cycle. This is fed to a strip-chart recorder that produces a hard copy of the average Doppler shift versus time. The zero-crossing detector counts how often the Doppler shift voltage changes from negative to positive or vice versa per second *(figure 2.5) (Kremkau, 2006)*. The higher the count, the higher the frequency. This count is presented on the vertical axis of a 2D graph where the horizontal axis represents time *(Kremkau, 2006)*.
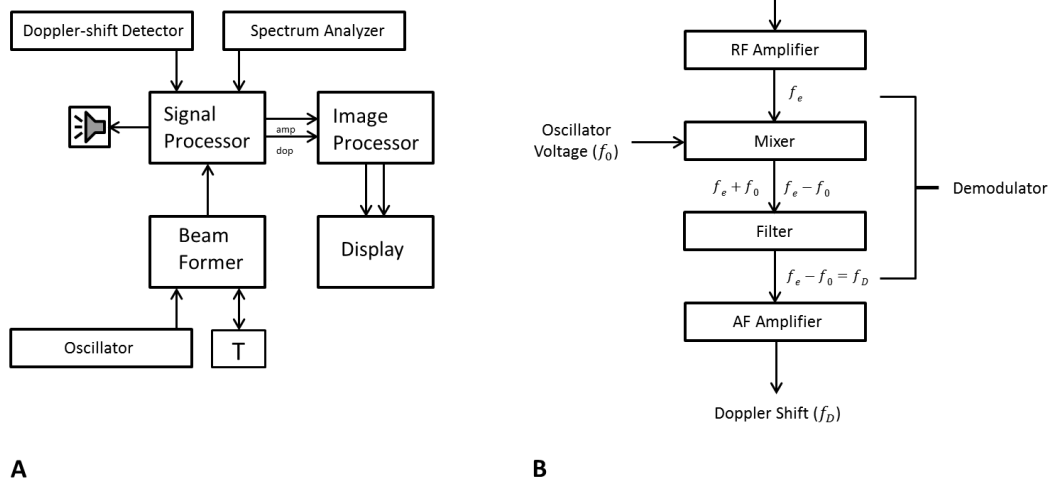
Figure 2.4 A, Block diagram of a sonographic instrument functioning as a CW Doppler instrument. The oscillator (part of the beam former) produces a continuously alternating voltage that drives the source transducer element (T). The receiving transducer element (T) produces a continuous voltage in response to echoes it constantly is receiving. The signal processor includes a Doppler shift detector that detects differences in frequency between the voltages produced by the oscillator and by the receiving element. The Doppler shifts produce voltages that drive loudspeakers and a visual display. The frequency of the audible sound is equal to the Doppler shift and is proportional to the reflector speed and to the cosine of the angle between the sound propagation direction and the boundary motion. B, Block diagram of a CW Doppler detector. The RF increases the echo voltage amplitude. The frequency of the echo voltage is f_e. In the mixer, this frequency is combined with the oscillator voltage, the frequency of which is f_0. The mixer yields the sum and difference of those two inputs. The low-pass filter removes $f_e + f_0$, leaving $f_e - f_0$ which is the Doppler frequency shift f_D. Then, this frequency is strengthened in the audio frequency (AF) amplifier. The mixer and filter together constitute the Doppler demodulator *(Kremkau, 2006)*.
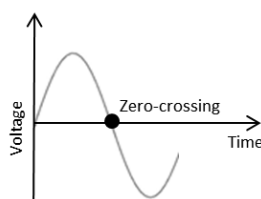

Figure 2.5 A zero-crossing detector counts the number of zero crossing per second in the positive or negative direction.

24

2.4 Pulsed Wave Doppler

A short pulse of ultrasound is transmitted into the tissue. The received signal is sampled at an adjustable delay after the pulse transmitted. By this, the signal from a localized range gate – sample volume – is retrieved, allowing the measurement of the blood velocity within a selected region. The width of the range cell is the same as the beam width, and the length is determined by the length of the transmitted pulse. The same transducer can be used both for transmission and reception *(figure 2.6) (Bjorn A.J. Angelsen, 2000)*.

T and R Crystal
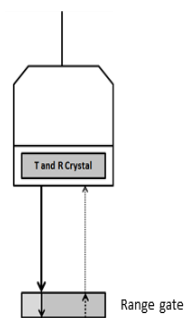
Range gate

Figure 2.6 PW Doppler with a single transducer and a defined range gate.

The pulsing of the beam also introduces a limit on the maximum velocity caused by the frequency aliasing that occurs with sampled signals. The Doppler signal is actually sampled once for every pulse transmission, and the sampling frequency is hence equal to the pulse repletion frequency (PRF) of the instrument *(Bjorn A.J. Angelsen, 2000)*. To avoid frequency aliasing with the Pulsed Wave (PW) Doppler, the Doppler shift (f_d) must therefore be less than half the sampling frequency (f_s):

$$f_d < \frac{f_s}{2} \qquad\qquad (2.4)$$

This is the requirement of the Shannon sampling theorem for error free reconstruction of a sampled signal and is often referred as the Nyquist limit on the frequency *(Bjorn A.J. Angelsen, 2000)*.

2.4.1 Components of a Pulsed Wave Doppler System

A diagram of the components of a PW Doppler instrument is presented in *figure 2.7, A (Kremkau, 2006)*. The pulser in the beam forming generates pulses of several cycles of voltage that drive the transducer where the ultrasound pulses are produced. Echo

voltages from the transducer are processed in the detector where they are amplified, their frequency is compared with the pulser frequency, and the Doppler shifts are determined. The Doppler shifts are sent to loudspeakers for audible output and to display for visual observation. Based on their arrival time, echoes coming from reflectors at a given depth may be selected by the amplifier gate. Thus, motion information may be obtained from a specific depth. This is called range gating. The operator controls the gate length and location. A PW Doppler instrument does not detect the complete Doppler shift as a CW instrument does but rather obtains samples of it. Because the PW instrument is a sampling system, each pulse yields a sample of the Doppler shifts signal. Doppler shifts are determined as previously described, except that the mixer receives a sampled input echo voltage rather than a continuous one. Echoes arrive from the sample volume depth in pulsed form at a rate equal to the PRF. Each of the returning echoes produces a sample of the Doppler shift from the Doppler detector. These samples are connected and filtered to yield the sampled waveform *(figure 2.7, B to E) (Kremkau, 2006)*.
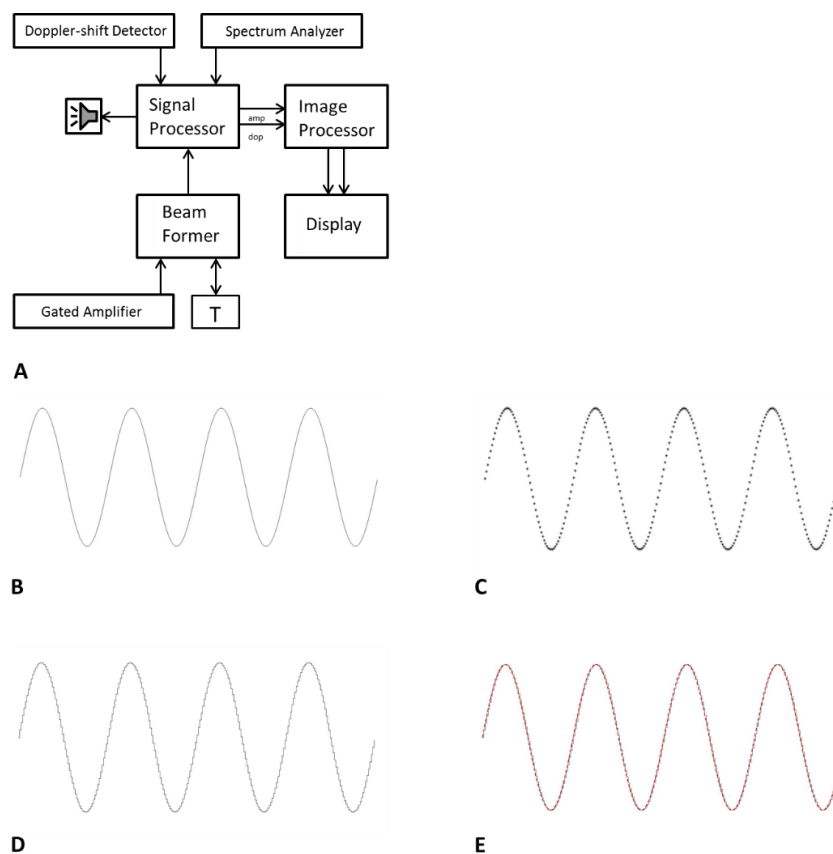

Figure 2.7 A, Block diagram of a PW Doppler instrument. The beam former produces voltage pulses of several cycles each, which drive the transducer (T). the signal processor

includes a Doppler-shift detector, where shift frequencies are compared to the frequency of the outgoing pulses. The Doppler shift is then sent to loudspeakers and, through the spectrum analyzer and image processor, to the display. The beam former also contains a gate that selects echoes from a given depth according to arrival time, and thus gives motion information from a selected depth. **B**, Cycles of a Doppler shift frequency. **C**, In a PW Doppler instrument, each pulse gives echoes from the sample volume. These echoes, after Doppler detection, yields samples (*) of the Doppler shift from the sample volume. **D**, The PW Doppler is also called sample and hold amplifier. It samples the returning stream of echoes (resulting from one emitted pulse of ultrasound) at the appropriate time for the desired depth and holds the value until the next pulse and sample are accomplished. **E**, Low-pass filtering smooths the sampled result (solid line), yielding the desired Doppler shift waveform (red dashed line) comparable to that shown in **B** *(Kremkau, 2006)*.

2.5 Spectral Analysis

Spectral analysis presents the Doppler information in the form of a Doppler frequency spectrum.

2.5.1 Frequency Spectrum

A spectrum is an array of the components of a wave, separated and arranged in order of increasing wavelength or frequency. Thus, spectral analysis presents Doppler shift frequencies in frequency order *(Kremkau, 2006)*.

Several types of flows occur in blood vessels. Changes in vessel size, turns, and abnormalities - plaques or stenosis - alter flow character. Flow can be characterized as plug, laminar, parabolic, disturbed, and turbulent. Portions of the flowing blood within a vessel are moving at different speeds and sometimes in different directions. Thus, as the ultrasound beam intersects this flow and produces echoes, the system will receive several different Doppler shifts, even from a small sample volume. This is what is called Doppler frequency spectrum *(Kremkau, 2006)*.

2.5.2 Fast Fourier Transform

The fast Fourier transform (FFT) is the mathematical tool the instrument uses to get the Doppler spectrum from the returning echoes of various frequencies *(figure 2.8) (Kremkau, 2006)*. FFT displays show spectral broadening, which is widening of the Doppler shift spectrum (*i.e.* an increase in the range of Doppler shift frequencies present) resulting from a broader range of flow speeds, and directions encounters by the sound beam with disturbed or turbulent flow *(Kremkau, 2006)*.
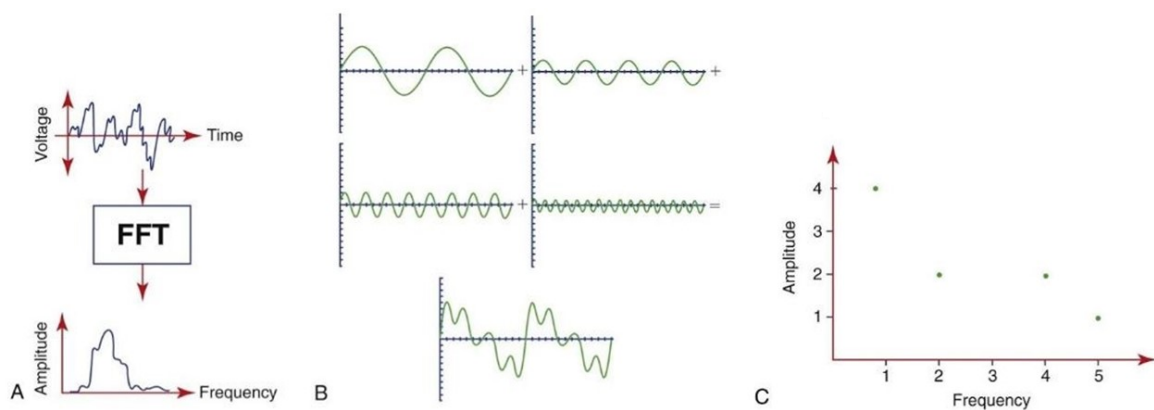
Figure 2.8 A, The Doppler shift signal is transformed using FFT into a spectrum. **B**, Four voltages of different frequencies are combined to yield the final result. **C**, FFT analysis of the combined voltage produces a spectrum of four components *(Kremkau, 2006)*.

2.6 Color Flow Imaging

Color flow imaging (CFI) is an ultrasound imaging technique whereby color-coded maps of tissue velocity are superimposed on grey-scale pulse-echo images of tissue anatomy. The most widespread use of the method is to image the movement of blood through arteries and veins, but it may also be used to image the motion of solid tissue. The production of velocity information is technically more demanding than the production of the anatomical information, partly because the target of interest is often blood, which backscatters significantly less power than solid tissues, and partly because several transmit–receive cycles are necessary for each velocity estimate *(Bercoff, 2011)*.

In CFI, flow velocity estimation relies on the use of N narrowband pulses transmitted at a constant PRF to estimate the Doppler frequency and/or power. N is commonly referred to as the color ensemble length and usually varies between 6 and 16 pulses. In a typical case, each ultrasound line is insonified N times. Acquisition and processing are done sequentially line by line as shown in *figure 2.9*. The main processing steps are clutter filtering to extract Doppler blood flow signals from tissue echoes, and estimation of the mean flow velocity, mostly using correlation-based methods *(Bercoff, 2011)*.
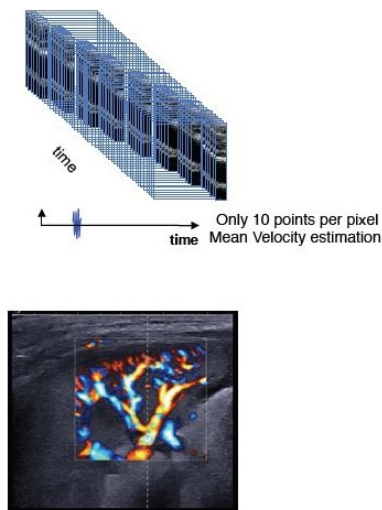
Figure 2.9 Data acquisition and processing in CFI *(Bercoff, 2011)*.

2.6.1 General Layout

A standard layout for a CFI system is given in *figure 2.10 (Evans, 2009)*. The beam former is the circuit that combines the signals from appropriate array elements with appropriate phasing to synthesize an optimal, dynamically focused beam in the required direction. Time gain compensation (TGC) is applied to the signal in order to compensate for the additional attenuation that signals from deep regions within the body will have suffered compared to those from more superficial regions. Then, the signal is quadrature demodulated, to preserve directional information, by mixing it with quadrature signals derived from the system master oscillator, and stored in the color vector memory. All the required samples from a single spatial vector can be acquired before moving on to another vector. Alternatively, particularly when the velocities are low, it is possible to build up the information from a number of vectors in a sequential manner to improve velocity resolution without sacrificing the frame rate. Once the required data for

estimating velocities along a given beam direction have been acquired, the data are further processed to filter out the clutter components, and to estimate the power, mean frequency, and bandwidth of the signal from each required sample volume along the beam. These estimates are then stored in the color frame memory, which allows both spatial and temporal averaging of these data before they are combined with the grey-scale pulse-echo information from the corresponding sample volume. The priority encoder determines the probability that there is flow (or required tissue motion) present in the sample volume and writes either color velocity information or, in the absence of valid velocity information, greyscale anatomical information to the display memory *(Evans, 2009)*.
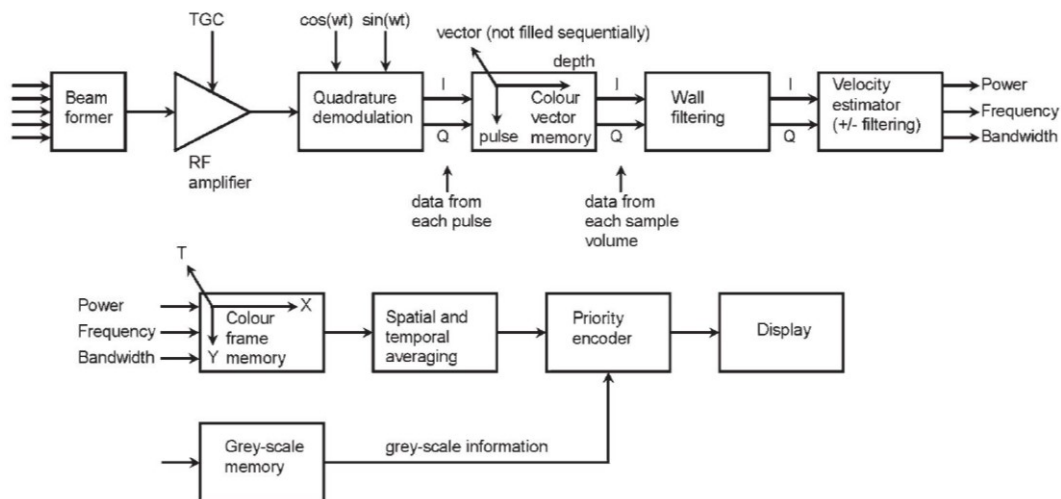
Figure 2.10 General layout of the Doppler path for a color-coded imaging system (RF, radio frequency; I, in-phase component of each signal; Q, quadrature component of each signal) *(Evans, 2009)*.

2.6.2 Filter and Clutter Rejection

High quality ultrasound color flow images require suppression of clutter signals originating from stationary and slowly moving tissue. With no sufficient clutter rejection, low velocity blood flow cannot be measured, and estimates of higher velocity will have a large bias *(Bjærum, 2002)*. In CFI systems, frame rate requirements limit the number of available samples to between about 4 and 16 making clutter filtering technically challenging. Various approaches to the problem have been suggested in the literature, and three of these are briefly discussed below *(Bjærum, 2002)*.

2.6.2.1 Finite Impulse Response Filters

The simplest type of clutter rejection filter is the single-echo canceller where, the output is derived by subtracting each successive echo from its predecessor. Signals from targets that are stationary should be unchanged and therefore will be cancelled, whereas those from targets that have moved will change and therefore not be subject to the same degree of cancellation *(Bjærum, 2002)*. In practice, the single-echo canceller is inadequate for most CFI applications because of its poor roll-off (6 dB/octave) and wide transition band. The roll-off of the simple echo canceller could be increased by cascading two such filters, but this only impairs the transition band problem *(Bjærum, 2002)*. More complex finite impulse response (FIR) filters could be designed with much narrower transition bands, but unfortunately this requires the use of much higher-order filters involving large numbers of data samples, which are not available in CFI applications *(Bjærum, 2002)*.

2.6.2.2 Infinite Impulse Response Filters

The frequency characteristics of output values must be discarded before the data becomes valid. As known, that is not possible in CFI applications of digital filters can be dramatically improved using infinite impulse (IIR) filters *(Bjærum, 2002)*. Unfortunately, IIR filters tend to have long transient responses, meaning that, unless appropriate steps are taken to initialize them, when a new signal is applied to the filter, a large number *(Bjærum, 2002)*.

2.6.2.3 Other Approaches

Hoeks et al. introduced regression filters based on the assumption that the slowly varying clutter components of the Doppler signal can be approximated by a low-order polynomial, which can be found using least-squares regression analysis *(Hoeks, 1991)*. Later, Bjærum and Torp *(Bjaerum, 1997)* described an adaptive regression filter performing significantly better than a standard regression filter under some circumstances *(Bjaerum, 1997)*. Then, Ledoux et al. suggested the singular-value decomposition method, which exploits both temporal and spatial information (Ledoux, 1997). In addition, a number of methods based on eigen-decomposition have been proposed too *(Bjærum, 2002; Kruse, 2002; Lovstakken, 2006; Yu, 2006; Yu, 2007)*.

2.6.3 Velocity Estimation

After clutter rejection, the resultant quadrature range-phase signals are passed to the velocity estimator where parameters such as total power, mean frequency, and bandwidth are estimated. Because of the small number of samples available for analysis, standard spectral analysis techniques appear to be not feasible *(Evans, 2009)*. In 1982, Namekawa et al. proposed the autocorrelation technique to estimate frequency in CFI systems *(Namekawa, 1982)*. The basis of the autocorrelation technique is described in *figure 2.11,* which shows the phase, relative to a master clock, of a signal vector during two successive samples, *i-1* and *i*. The angular frequency ω of the vector is defined as its rate of change in phase, or:

$$\omega = \frac{d\phi}{dt} = \frac{\phi_i - \phi_{i-1}}{T} \tag{2.5}$$

where T is the pulse repetition interval.

The tangent of the required phase difference $\phi_i - \phi_{i-1}$ can be written as:

$$\tan(\phi_i - \phi_{i-1}) = \frac{\sin \phi_i - \phi_{i-1}}{\cos \phi_i - \phi_{i-1}} = \frac{\sin \phi_i \cos \phi_{i-1} - \cos \phi_i \sin \phi_{i-1}}{\cos \phi_i \cos \phi_{i-1} - \sin \phi_i \sin \phi_{i-1}} \tag{2.6}$$

If the sine and cosine terms are written as the in-phase magnitude *I* and quadrature magnitude *Q* of the vectors, and an average frequency calculated by summing over a number of pulse pairs, then the mean angular frequency is:

$$\bar{\omega} = \frac{1}{T} \tan^{-1} \left[\frac{\sum_{i=1}^{n} Q(i)I(i-1) - I(i)Q(i-1)}{\sum_{i=1}^{n} Q(i)I(i-1) + I(i)Q(i-1)} \right] \tag{2.7}$$

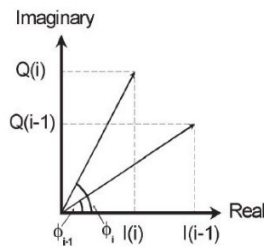

Figure 2.11 Position of a rotating signal vector during two successive samples *i-1* and *I,* showing the in-phase components *I(i-1)* and *I(i)*, and the quadrature components *Q(i-1)* and *Q(i) (Evans, 2009).*

The output of the autocorrelation estimator is ideally unbiased because adding white noise to the signal does not affect the autocorrelation at finite lags, although a decreasing

signal-to-noise ratio leads to an increase in the variance of the estimate. However, because of the inevitable use of clutter rejection filters, the system noise is inevitably colored, the autocorrelation function is not zero at lag one, and the estimated mean frequency is biased. These effects can be reduced using clutter filters with good roll-off characteristics, such as IIR filters *(Evans, 2009)*.

The autocorrelator provides an unambiguous output for narrowband signals over the range $\pm\pi$ rad. Moreover, the autocorrelator properly works with wideband signals with mean frequencies of up to close to $\pm\pi$ rad because it correctly accounts for partial aliasing in a continuous spectrum *(Evans, 2009)*.

Currently, modern scanners use the 2D autocorrelation estimator, which calculates axial velocity from the Doppler equation using explicit estimates of both the mean Doppler frequency and the mean radio frequency at each range gate location. This has considerable advantages over the conventional 1D method, which implicitly assumes that the mean RF is constant and equal to the center frequency of the transmitted pulse, since, actually, the local RF varies considerably because of both the stochastic nature of the backscattered signal and the frequency-dependent effects of attenuation and scattering *(Evans, 2009)*.

A further benefit of the 2D autocorrelator is that, in its standard implementation, estimates of the Doppler frequency are derived by processing subsamples from a number of axial depths, which leads to a reduction in the variance of the Doppler frequency estimate *(Evans, 2009)*.

2.6.4 Post-Processing

The estimated mean frequency, power, and variance are stored in a color frame memory, and then subjected to further processing. Because of the stochastic nature of Doppler signals are stochastic in nature - estimates of the Doppler parameter data vary in a random manner -, regions of color drop-out in flow-containing areas and flashes of color in flow-free areas could be present. To address these issues, several post-processing techniques, such as linear and/or non-linear spatial and temporal filtering of the Doppler

parameter data, are used to improve the consistency and acceptability of the color images *(Evans, 2009)*.

2.6.5 Priority Encoding

Since the frequency estimator provides nonzero values for Doppler signal power, mean frequency, and bandwidth in each sample volume irrespective of whether there is any real flow or movement present, it is crucial to determine whether the estimator output is a result of real flow or purely artefactual in nature. In the first case, the Doppler information is color coded and written to the appropriate part of the screen while in the other case, only the grey-scale pulse-echo information is presented. To address this crucial decision the priority encoder is used *(Evans, 2009)*.

2.7 Power Doppler

If standard CFI techniques produce a 2D map of flow velocities towards or away from the ultrasound transducer, PD measures and displays the intensity or the power of the signal as it changes in time at each region within the interrogated area *(Evans, 2009)*.

The information on the intensity of the Doppler signal is obtained from the same autocorrelation process used in CFI and is also displayed in real-time *(Martinoli, 1998)*. However, both the velocity and the direction of flow are missing and the color flow is monochromatic: the higher the intensity of the Doppler signal, the lighter the hue of the color displayed within the vessels. Actually, some machines are now able to overwrite the directional information on PD images. This is obtained by the interpolation of CFI readout phases into a conventional PD acquisition *(Martinoli, 1998)*.

The intensity or power of the signal depends on the number of scatters within the Doppler sensitive region, and it is determined by complex interactions between several factors such as hematocrit level, blood flow velocity, and shear rates *(Bude, 1996)*. An additional factor is the depth of the vessel from the transducer: the greater the attenuation from the overlying tissues, the weaker the returning signal becomes *(Rubin, 1993; Rubin, 1994)*.

Advantages of PD over CFI account its extended dynamic range which results in an increase in sensitivity to flow, and its relative independence of beam to vessel angle which produces a better delineation of tortuous vessels.

An increase in CFI gain results in an increase of both weaker echoes and noise. Since noise contains a wide frequency spread, it is displayed in the CFI image as random velocities in random directions. This results in a 'mosaic of colors' that could mask real vascular signals. Consequently, the color gain is commonly raised until noise begins to appear in the image as a colored 'snow storm', and then it is slightly lowered. In PD images, because of its low power, noise is coded as a single background color throughout the image. Additionally, a dark hue, which may be blended with the B-mode of the ultrasound image, is commonly assigned. Signals from moving blood are encoded with different hues and, thus, can be easily discriminated from noise *(Martinoli, 1998)*. The uniform background display of noise in PD images often allows the gain to be increased by 10±15 dB over CFI; therefore, previously undetected vessels can be identified *(Rubin, 1993)*. For optimum sensitivity, the PD gain should be set using an opaque background, as advised by Rubin and Adler *(Rubin, 1993)* and Rubin et al. *(Rubin, 1994)*. Gain optimization would have the advantage of maximum sensitivity and of an objective, standardized method of scanning.

PD is almost independent from the beam to vessel angle because it is based on the number of scatters moving within the vessel, rather than on the frequency shift they generate *(Martinoli, 1998)*. Thus, use of a PD display helps to improve the appearance of tortuous and irregular vessels by coding them with a slightly constant color, irrespective of insonification angle. Moreover, because of the effects of intrinsic spectral broadening *(Evans, 2000)*, it is possible to detect Doppler power even when the ultrasound beam is at right angles to the directions of flow, although clutter filters inevitably reduce the total Doppler power returning from a vessel in such an orientation *(Evans, 2009)*.

Furthermore, aliasing has no effects on the PD display because it does not provide any information on the frequency of the Doppler signals *(Martinoli, 1998)*.

PD is more sensitive to tissue motion artifacts than CFI. Movements of soft tissues cause signals of high intensity and low frequency that create flash artifacts. Improved clutter rejection can be obtained by using weighted temporal averaging techniques which,

however, may reduce the frame rate of the PD to an unacceptable level. Presently, the method only works properly on relatively slow-moving structures *(Martinoli, 1998)*. An additional motion artifact can be observed from highly echogenic stationary interfaces. When they move even slightly, they may produce such strong signals that completely overwhelm the clutter canceller. This artifact mainly occurs at sufficiently characteristic positions, such as the surface of organs or structures, to avoid misinterpretations. If it is not possible to discriminate between real flow and PD based artifacts, spectral Doppler can be used to establish whether the displayed images are vascular or not *(Martinoli, 1998)*. Additionally, note that Doppler signals originating from tissue movements can be encoded and used in clinical applications to evaluate moving structures *(Martinoli, 1998)*. To note that, albeit PD has significant advantages over standard CFI, these are only gained at the expense of suppressing all information on velocity *(Evans, 2009)*.

A comparison between CFI and PD images is provided in *figure 2.12.*

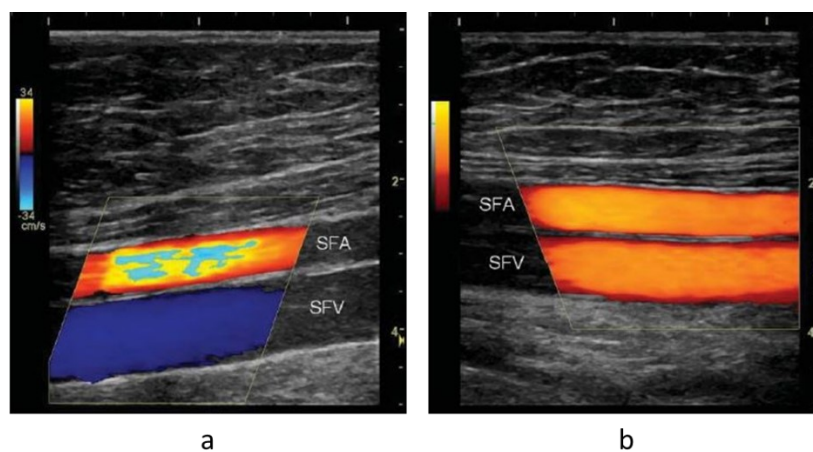a   b

Figure 2.12 (a) Color flow image of the superficial femoral artery (SFA) and the superficial femoral vein (SFV) in the thigh of a healthy subject. The subject's head is to the left of the scan, and so the arterial flow is from left to right and the venous flow from right to left. The color scale on the left of the image is calibrated in centimeters per second and shows that flow towards the probe is colored as red-orange-yellow, while the flow away from the probe is colored as blue. The blue color appearing in the middle of the SFA is a result of aliasing and not reverse flow. The scale to the right and top of the image is calibrated in centimeters. Note that the color box, from which the velocity image is extracted, occupies only part of the image. **(b)** Power Doppler image of the SFA and SFV. The color scale on the left is purely qualitative showing that greater Doppler power is represented by a

brighter shade of brown-orange-yellow. Because it is power rather than velocity that is mapped there is no information about the direction of flow, but aliasing does not lead to a potentially confusing change in color in the center of the SFA *(Evans, 2009)*.

2.8 Ultrafast Doppler

Conventional Doppler analysis is performed using:

- CFI to spatially locate a flow region
- PW spectral Doppler to perform quantitative measurement in the flow region of interest depicted by CFI

In a typical Doppler exam, the user constantly goes back and forth between those two modes and successively analyzes with PW spectral Doppler the locations pointed out by the CFI mode. Triple mode (simultaneous color and PW) has been introduced to improve the user workflow. Despite some compromises on the PW spectrum quality, it facilitates the acquisition of information in many cases *(Bercoff, 2011).*

Using an ultrafast architecture, Doppler can be envisioned in a completely different manner: quantitative information is acquired at the same time in all pixels of the color box breaking the incompatibility between imaging and quantitative measurements *(Bercoff, 2011).*

2.8.1 Ultrafast Sequence for Doppler Imaging

Ultrafast imaging relies on the coherent compounding of backscattered echoes resulting from successive tilted plane waves emissions *(figure 2.13).* The maximum number of angles that can be used to compute an image is limited by the acquisition $PRF_{Doppler}$ necessary to measure the desired Doppler velocity scale *(Bercoff, 2011).*

$$N_{angles} = \frac{PRF_{max}}{PRF_{doppler}} \tag{2.8}$$

where PRF_{max} is the maximum PRF reachable for a given imaging depth.

Using ultrafast imaging, Doppler information is continuously and simultaneously acquired across the full image. Therefore, unlike conventional CFI acquisitions, all pixels are sampled at a high Doppler PRF in an uninterrupted and concurrent manner, allowing performing full flow quantification at every pixel within the ultrafast color box *(Bercoff, 2011)*. In a typical implementation of Ultrafast Doppler, a single-shot acquisition can be launched from the conventional CFI mode. A full clip of Ultrafast Doppler data is acquired (typically 2 to 4 s) and the system is frozen. The user can then review the Ultrafast color flow imaging clip, select the frame(s) offering best visualization of the flow properties of interest, and perform full spectral analysis at every pixel of the color box in a retrospective manner. Retrospective Ultrafast spectral analysis allows comparing flow spectra and measurements from multiple locations, which have been acquired simultaneously *(Bercoff, 2011)*.
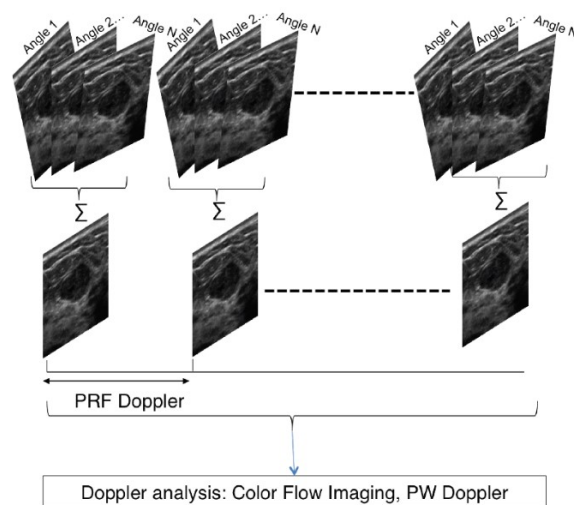

Figure 2.13 Ultrafast compound imaging for Doppler analysis of flow *(Bercoff, 2011)*.

Ultrafast Doppler offers *(Bercoff, 2011)*:

- A significant improvement of CFI performance in terms of temporal resolution and sensitivity;
- A new Doppler paradigm by merging CFI and PW Doppler modes in a single fully-quantifiable acquisition, which can simplify workflow, reduce exam time, and can enable advanced measurement and visualization capabilities.

2.8.2 Improving Color Flow Imaging

Conventional CFI offers limited frame rates (typically 20 Hz) and suffers from severe trade-offs between image size and frame rate. Ultrafast compound based Doppler imaging provides flow images with a very high temporal resolution whatever the box size *(Bercoff, 2011). Figure 2.14* shows two conventional color Doppler frames from a femoral artery, plus the corresponding frames obtained by means of Ultrafast Doppler. Ultrafast Doppler exhibits high flow sensitivity, and provides frame rates higher than 80 Hz. Conversely, conventional color Doppler is limited to a frame rate of 19 Hz which results in insufficient sampling of the underlying flow dynamics. In fact, as shown by the bottom frames of *figure 2.14* the reverse flow is perfectly documented in the Ultrafast Doppler frame, but completely missed by the conventional color Doppler acquisition. Ultrafast Doppler enables frame rate increases by a factor of 5 to 10 compared to conventional color Doppler, typically from 60 up to 200Hz, without sacrificing field of view or spatial resolution. These improvements allow the visualization of complex flow dynamics and transient flow events *(Bercoff, 2011).*
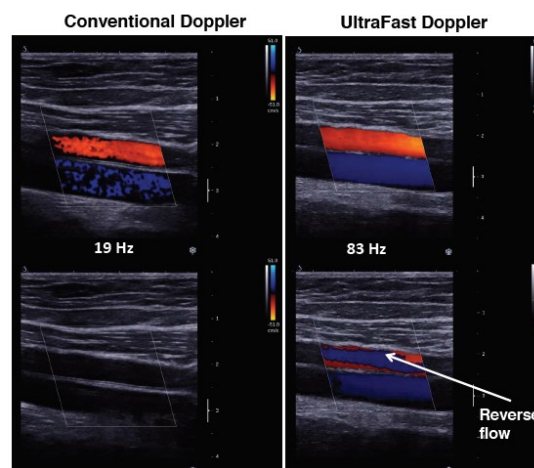

Figure 2.14 Ultrafast color flow imaging provides increased temporal resolution and sensitivity *(Bercoff, 2011).*

Compared to conventional color Doppler imaging, Ultrafast Doppler acquisitions guarantee several advantages *(Bercoff, 2011)*:

- Clips of color data can be generated with higher sensitivity and frame rates than on conventional systems.

- The increased quality is maintained whatever the box size. Conventional color Doppler suffers from trade-offs between frame rate and color box size. Using plane waves, the whole area of interest can be filled with color Doppler information without any drop-in frame rate.

- The flow information is consistent and synchronous throughout the imaged area, since the Doppler signals corresponding to all pixels are acquired at the same time. In contrast, conventional color Doppler lines are sequentially acquired, so that the Doppler signals on the sides of the color box exhibit time lags that can reach several hundreds of milliseconds.

2.8.3 Full Flow Quantification

Ultrafast Doppler enables full quantification of flow data everywhere in the image. The user can position a sample volume anywhere within the region of interest and the system responds by instantaneously computing and displaying the PW spectrogram from the selected location. Up to three spectrograms can be calculated and displayed simultaneously on the image, as shown in *figure 2.15*. Measurements can be performed independently on all spectrograms and compared to each other with a high degree of reliability, since all spectra are computed from data acquired at the same time, on the same cardiac cycles. Note that the results of Ultrafast spectral analysis are numerically equivalent to those obtained by conventional PW Doppler exam performed under the same conditions *(Bercoff, 2011)*.
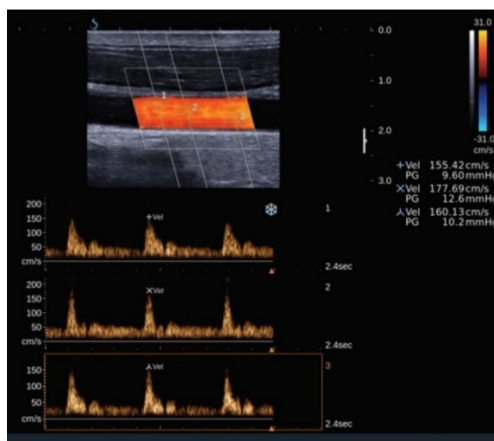

Figure 2.15 Simultaneous Ultrafast Doppler spectral analysis from three sample volumes *(Bercoff, 2011)*.

Time-Domain Methods for Assessing Tissue Motion by Analysis from Reflected Ultrasound Echoes

3.1 Introduction

Motion estimation is performed in several ultrasound-based techniques such as blood flow imaging, elastography or elasticity imaging, phase-aberration correction, and strain compounding. Several methods have been suggested for motion estimation, including phase-domain methods, time-domain or space-domain methods, and spline-based methods *(Luo, 2010)*.

In the following sections, an overview of some of the most effective time-domain based tissue-motion techniques is proposed. The techniques are grouped into two general categories: 1D and 2D measurement configuration.

3.2 One-Dimension Measurement Configurations

A 1-D measurement configuration consists of analyses executed upon ultrasound data acquired along a single A-line. The ultrasound data may be in the form of the RF signal, the envelope-detected signal, or on pixels in an M-mode ultrasound image. Typically, a number of echoes along an A-line are acquired and stored, and motion information is extracted by comparison of echoes acquired at different times *(Hein, 1993)*.

3.2.1 Digital Wall Tracking

The simplest method of measuring tissue motion with ultrasound echoes is to track the rising edge of an echo reflected from a tissue interface, such as a vessel wall *(Hein, 1993)*. Powalowski et al. have used this technique to measure the motion of blood vessels and to assess the hemodynamic properties of the blood vessel *(Powalawski, 1988)*. If a pulsed ultrasound beam is directed at a vessel, then echoes will be reflected from the interior and exterior surfaces of the vessel walls. The analog echoes are fed into a comparator circuit that produces a digital output pulse whenever the analog waveform exceeds a predetermined trigger level. The digital pulses from the comparator will move back and forth in time along with the motion of the vessel wall. The motion is digitally tracked using a tracing gate and a clock. To identify a desired echo slope, the tracing gate is

generated at a desired range. Clock pulses are counted from the transmission of the pulse until the first rising echo edge after the tracing gate *(Powalawski, 1988)*. Powalowski's system consists of two ultrasound transducers used simultaneously: a 6.75 MHz pulsed and a 4.5 MHz continuous wave Doppler *(Powalawski, 1988)*. The pulsed transducer is used to digitally track and estimate the vessel wall diameter and the continuous wave to measure the blood flow velocity *(Powalawski, 1988)*. If the instantaneous vessel wall diameter and blood flow velocities are known, various hemodynamic parameters such as the volumetric blood flow rate, blood pressure, input vessel impedance, vessel diameter change over work cycle of the heart, pulse wave velocity, and coefficient of rigidity of the blood vessel walls can be estimated *(Powalawski, 1988)*. The digital wall tracking technique presents significant limitations since it only observes rising edges of ultrasound echoes *(Powalawski, 1988)*. Moreover, the tracing gate must be set precisely, and if the walls move out of the range of the tracing gate, there will be ambiguities as to what tissues are under observation *(Hein, 1993)*.

3.2.2 Correlation Techniques

Correlation techniques estimate tissue motion by tracking a segment of echo reflected from a group of scatters rather than just the rising edge.

3.2.2.1 Normalized Correlation Coefficient

The standard correlation coefficient used to express the linear association between two random variables X and Y is given as:

$$R = \frac{\sigma_{xy}}{\sigma_x \sigma_y} \tag{3.1}$$

where σ_x is the standard deviation of *X*, σ_y is the standard deviation of *Y*, and σ_{xy} is the covariance of *X* and *Y*. *R* is a normalized correlation coefficient such that *-1 ≤ R ≤ 1*, where *R = -1* indicates a perfect negative linear association, *R = +1* represents a perfect positive linear association, and *R = 0* indicates that no linear association exists between X and *Y (Hein, 1993)*.

If *X* and *Y* consist of *N* discrete values such that *X = {y(0), y(1), …, y(N-1)}*, the correlation coefficient is defined as:

$$R = \frac{\sum_{i=0}^{N-1}[x(i) - \overline{X}][y(i) - \overline{Y}]}{\sqrt{\sum_{uj=0}^{N-1}[x(i) - \overline{X}]^2 \sum_{k=0}^{N-1}[y(i) - \overline{Y}]^2}} \tag{3.2}$$

Where $\overline{X}$ and $\overline{Y}$ are the mean of X and Y, respectively. If X and Y are two ultrasound echoes that have been digitized and stored, *equation 3.2* can be used to determine the similarity between the two ultrasound echoes, which can in turn be related to tissue motion by various algorithms *(Hein, 1993)*.

3.2.2.2 Tissue Motion Assessment by Normalized Correlation of Echoes

A typical pulse-echo ultrasound measurement arrangement for motion estimation is shown in *figure 3.1 (Hein, 1993)*. Suppose that it is desired to collect information starting from the face of the transducer to a depth of *z* cm. The ultrasound echo reflected from the tissue covering this distance will be of duration *a* ms, where *a* is related to *z* by the speed of sound in the tissue. If the A/D is digitizing at a rate of *F* points/s, then the digitized echo will consist of *M* discrete points where *M = Fa.* Any resolution volume *V* within the ultrasound beam will be defined by the width of the beam, the distance *d* from the transducer, and an axial length *l.* The ultrasonic signal reflected from this particular resolution volume occurs at *r* points within the echo for *a* duration of *N* points. Echo segments of width *N* points can then be windowed out for processing, where *N* represents the spatial axial resolution of the measurements and is typically determined by resolution versus accuracy tradeoffs. If more than one echo is digitized and stored, the normalized correlation coefficient *R* can be calculated for window length *N* and distance d from the transducer *(Hein, 1993)*. From *(equation 3.2)* and the assumption that the mean value of *RF* echoes is zero, *(equation 3.2)* is:

$$R = \frac{\sum_{i=0}^{N-1} E_1(r+i)E_2(r+i)}{\sqrt{\sum_{uj=0}^{N-1}[E_1(r+j)]^2 \sum_{k=0}^{N-1}[E_2(r+k)]^2}} \tag{3.3}$$

Where E_1 and E_2 are echoes acquired at two different points in time. In this case, the normalized correlation coefficient *R* indicates the similarity of the two windowed echoes. If they are exactly the same, then *R = 1*, and if they have no similarity, then *R = 0*. If *R = -1* the two echoes are exactly inverted about the amplitude axis *(Hein, 1993)*.
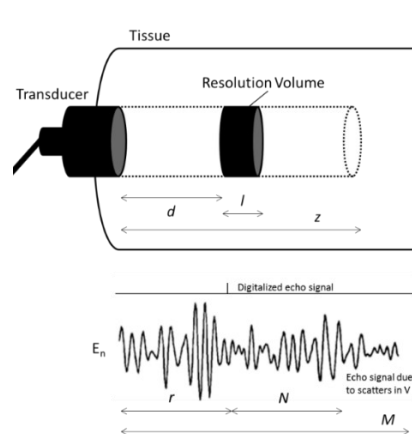
Figure 3.1 Digitalized RF echo E_n reflected from scatters within the ultrasound beam. If the digitalized echo is M points long, the footprint corresponding to a resolution volume at a distance d from the transducer will be located at a position r within the echo.

The amount of tissue motion between transmissions of ultrasonic pulses can be estimated from the value of the normalized correlation coefficient, computed between different echoes. The more the tissue has moved, the smaller the value of R *(Hein, 1993)*. Ideally, this is shown in *figure 3.2* for tissue moving axially away from the transducer. In this case three pulses are transmitted and three echoes received. If the tissue is moving with a velocity v, then the tissue will move a distance d_1 between the first and second echo and d_2 between the first and third echo. In this instance the correlation coefficient R_{12} between the first and second echo is 0.6. Since the tissue has moved farther between the first and third than the first and second echoes, R_{13} = 0.1. If all of the original tissue moves out of the window between the first and nth echo, then $R_{1n,}$ = 0. Thus, the change in R between echoes is proportional to the distance the tissue has moved. Note that the value of the normalized correlation coefficient will change not only for axial motion but also for lateral and transverse motions, which will move the original scatter volume out of the beam *(Hein, 1993)*.
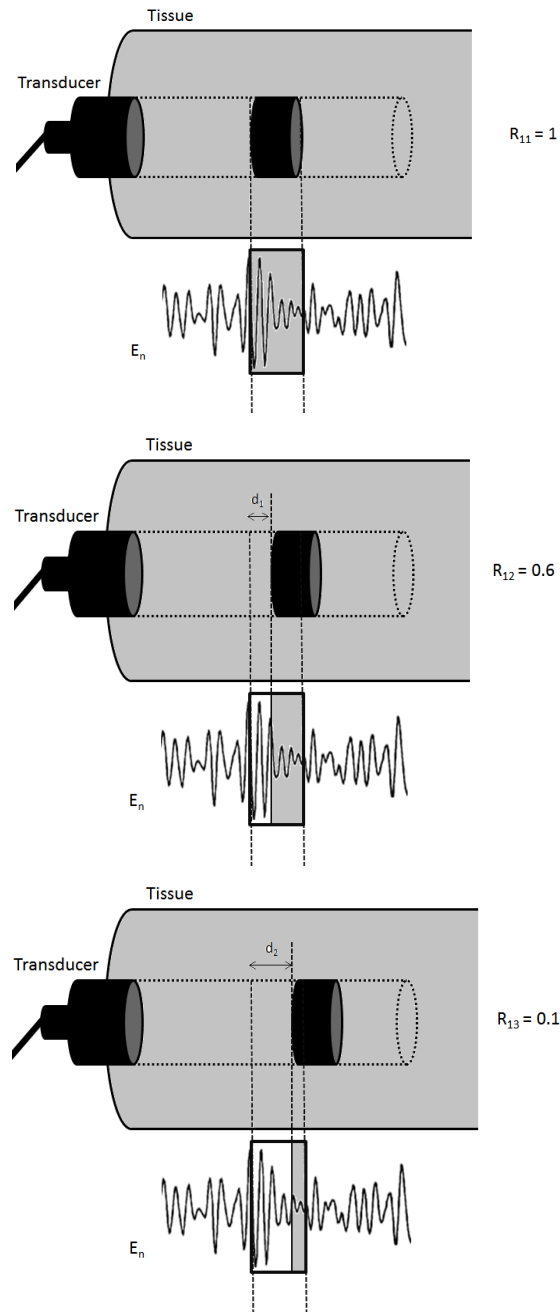
Figure 3.2 Variation of the normalized correlation coefficient with tissue motion within the correlation window. The greater the amount of tissue motion between echoes, the smaller the value of the normalized correlation coefficient.

3.2.2.3 Velocity Estimation by Correlation Search Algorithm

Tissue motion can be measured using the correlation coefficient to track the same group of scatters. Assuming that a given group of scatters leaves a unique footprint in ultrasonic echoes, the motion of those scatters can then be tracked by tracing the footprint from different ultrasonic echoes. The process can be thought of as shifting one echo with

respect to another until the echoes overlap. This corresponds to searching for the maximum in the normalized correlation coefficient, and effectively measuring the difference in arrival times of the ultrasound footprint signal reflected from a given group of scatters *(Hein, 1993)*.

The basic ultrasound time-domain cross-correlation velocity measurement concept is shown in *figure 3.3* for RF data *(Hein, 1993)*. Suppose that an ultrasonic pulse is transmitted at time $t = t_1$ and an RF echo E_1 is recorded. If a tissue scatter group is located at d_1, then it will produce an ultrasonic footprint located at a distance r points and length N points within E_1. If another pulse is transmitted at $t = t_2$, then the scatters will have moved some unknown distance Δd (shown moved toward the transducer in *figure 3.3*) *(Hein, 1993)*. The ultrasonic footprint will also have moved accordingly to a new spot in E_2. The distance (in time) the scatters have moved can be determined by correlating the original footprint in E_1, with different equivalent length sections of E_2 *(Hein, 1993)*. Mathematically, the process consists of shifting the windowed footprint from E_1 by s and varying s until the same footprint is found in E_2. The correlation coefficient $R(s)$ is calculated for each value of s, and the value of s producing the maximum in $R(s)$ corresponds to $s = \tau$, the new location of the tissue scatters. Basically, the search for the maximum correlation coefficient is performed in discrete increments of the digitizing period *(Hein, 1993)*. Actually, the true location of the maximum is not constrained to these increments, and will generally lie somewhere between the discrete maximum and one of the two neighboring points *(Hein, 1993)*. The true location of the maximum can be estimated by fitting a curve, such as a parabola or cosine, and using the location of the top of the curve as the fractional part (in terms of discrete shift increments) of the shift *(Hein, 1993)*. Once the shift τ has been estimated, the distance the tissue scatters have moved axially is given by:

$$d_a = \frac{c\tau}{2}$$ (3.4)

where c is the speed of sound. Since velocity is distance/time, the axial velocity of the scatters is given by:

$$V_a = \frac{c\tau}{2T}$$ (3.5)

where T is the pulse repetition period.

Note that only the axial component of velocity is measured; in order to estimate the lateral movement some a priori information, such as the measurement angle, must be known *(Hein, 1993)*.
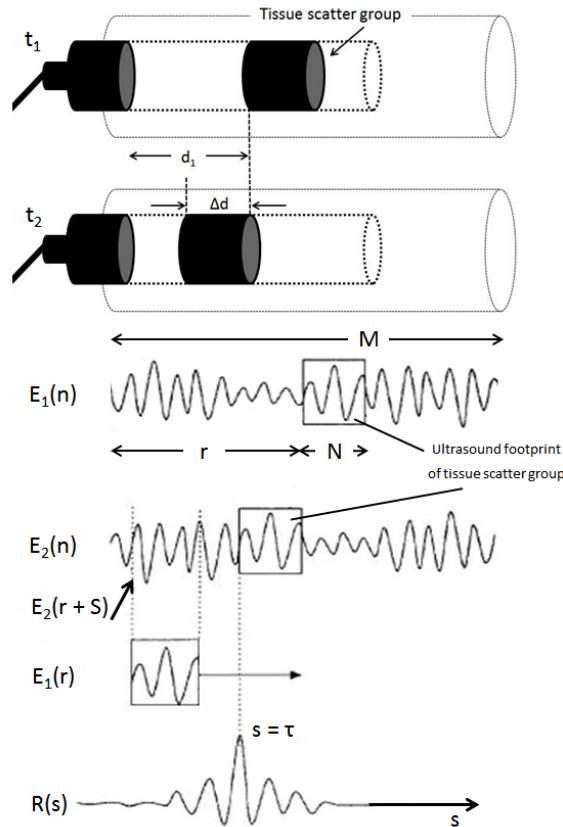

Figure 3.3 Digital tracking of a tissue volume by locating the maximum in the normalized correlation function. A window of width *N* at a desired range r is removed from one echo E_1 and is correlated at different locations s along another echo E_2. The value of s producing the maximum correlation coefficient *R(s)* corresponds to *s = τ*.

3.2.2.4 Correlation Interpolation

De Jong, *et al.* have developed a correlation interpolation algorithm that computes the correlation coefficient at only five points in the neighborhood of the maximum, and use an interpolation algorithm to estimate the location of the maximum from these points *(De Jong, 1990)*. In that study, the received echo signal *y* from moving tissue has been defined as:

$$y(x,t) = s(x - vt) + n(x,t) \tag{3.6}$$

Where *s* is the signal reflected by the tissue, *x* is the depth, *t* is time, *v* is the tissue velocity and *n* is the noise uncorrelated with signal. If *y(x,t)* is sampled at spacings of *Δx* in

depth and Δt in time, the discrete 2D autocorrelation R_{yy} (X,T) can be estimated numerically by:

$$R_{yy}(X,T) = \frac{1}{i_{max}j_{max}} \sum_{j=1}^{j_{max}} \sum_{i=1}^{i_{max}} y(x,t)y(x+X,t+T) \tag{3.7}$$

Where $x + i\Delta x$, $t = j\Delta t$, $x = I\Delta x$, $T = J\Delta t$, I, j, I, J are integers. X and T represent shifts in depth and time, i_{max} is the number of samples in depth and j_{max} is the number of samples in time where $i_{max} * j_{max}$ equals the total number of sampled used. The autocorrelation function is evaluated at $R_{yy}(0,0)$, $R_{yy}(\Delta x, 0)$, $R_{yy}(0, \Delta t)$, $R_{yy}(+\Delta x, \Delta t)$ and $R_{yy}(-x, \Delta t)$. These five values are fit to a cosine function to estimate the location of the maximum correlation; the final axial velocity estimate is:

$$V_a = \frac{\Delta x}{\Delta t} \frac{\beta}{\alpha} \tag{3.8}$$

Where

$$\alpha = \cos^{-1} \frac{R_{yy}(\Delta x, 0)}{R_{yy}(0,0)} \tag{3.9}$$

$$\beta = \tan^{-1} \frac{R_{yy}(\Delta x, \Delta t) - R_{yy}(-\Delta x, \Delta t)}{2 \sin \alpha R_{yy}(0, \Delta t)} \tag{3.10}$$

This velocity estimation is valid as long as the shift between echoes is within ± 0.5 of a signal period. The main advantage of the correlation interpolation is that several echoes can be analyzed in a single calculation and only five correlations are required to estimate velocity. Drawbacks include low performances with larger bandwidth signals and aliasing *(De Jong, 1990)*.

3.3 Two-Dimension Measurement Configurations

2D motion estimation algorithms can be also used to assess different physical components of motion. A change in tissue shape (deformation) or a change in tissue density (compression or expansion) results in a corresponding change in the speckle pattern observed in the ultrasound image *(Hein, 1993)*.

Below some of the most used and effective 2D motion estimation techniques are described.

3.3.1 Subtraction Algorithms

The simplest mean to detect motion between two video frames is to subtract one image from another. Pixel locations with no change in brightness will show up with zero brightness in the subtracted image, and those with changes in brightness will show up with the difference in brightness. Thus, the subtraction of two consecutive ultrasound B-mode images will indicate where in the image there has been tissue motion. In the case of blood flow, this method is effective for showing large differences between frames but maps small differences from blood flow into a few gray levels near zero with very little contrast *(Gardiner, 1989)*. Alternatively, bit-by-bit Boolean operations in identically positioned pixels between frame buffers can be performed. Gardiner and Fox have used this method with the Boolean operations AND, OR, and XOR to produce in vivo color flow images for flow measured in the abdominal aorta of a human *(Gardiner, 1989)*. The main advantages of this account the real time performance, and the angle independence of Doppler measurements. However, it is just qualitative; in fact, it gives an indication that there is motion, but provides no information about the direction of motion (*Gardiner, 1989*).

3.3.2 2D Block Matching Algorithms

To obtain the direction of motion of blood cell scatters, the scatters must be tracked as they move from frame to frame. This can be accomplished with block-matching search algorithms performed on different digitized video frames *(Hein, 1993)*. A block-matching system is provided in *figure 3.4 (Hein, 1993)*. A group of blood cell scatters is in location 1 in the first image frame and has moved to location 2 in the second image frame. The scatters can be tracked by removing a target region block from the first frame and sweeping it over a search region from the second frame to find out where in the search region the original target region block has moved to *(Hein, 1993)*. Mathematically, there are several methods to determine the similarity between the target region block and the current search region block, for example, by computing the 2D correlation coefficient. The 2D correlation coefficient is just an extension of the 1D case: a normalized correlation coefficient is calculated at each search position, and the position where the correlation coefficient is maximum corresponds to the new scatter position *(Hein, 1993).* If two

images *X* and *Y* have been acquired, the correlation coefficient can be written for the 2D *k* x *l* window as:

$$R = \frac{\sum_{i=1}^{l}\sum_{j=1}^{k}(X_{i,j}-\bar{X})(Y_{i+m,j+n}-\bar{Y})}{\sqrt{\sum_{i=1}^{l}\sum_{j=1}^{k}(X_{i,j}-\bar{X})^2 \sum_{i=1}^{l}\sum_{j=1}^{k}(Y_{i+m,j+n}-\bar{Y})^2}}$$

(3.11)

Where $X_{i,j}$ are pixels in the target region windowed from frame X, $Y_{i+m,j+n}$ are pixels at location *m, n* windowed from the search region in frame Y, and $\bar{X}$ and $\bar{Y}$ are the mean pixel values of the corresponding windows. The location *m, n* which produced the maximum in $\rho_{m,n}$ is considered to be the new location of the scatters *(Hein, 1993)*.
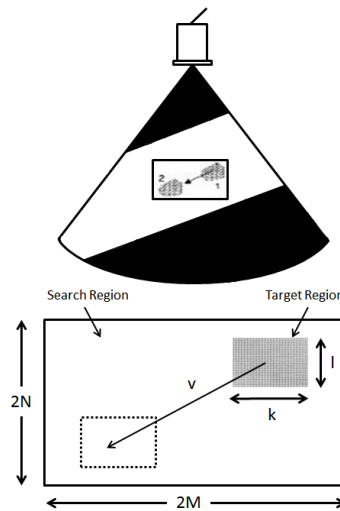
Figure 3.4 2D correlation search algorithm geometry. The target region from one image is swept across the search region from a different image and the 2D correlation coefficient is computed at each position in the search region *(Hein, 1993)*.

Robinson et al. first performed a 2D correlation search on ultrasound images to estimate the ultrasound velocity in tissue *(Robinson, 1983)*. In this study, two ultrasound images from different positions of a region of interest were acquired and the shift of the region of interest in the two images by 2D cross-correlation was measured *(Robinson, 1983)*.

The use of 2-D correlation to estimate motion from ultrasound B-mode images was first introduced by Akiyama et al. in 1986 for soft tissue motion and by Trahey et al. in 1987 for angle-independent blood flow detection *(Akiyama, 1986; Trahey, 1987)*. In 1988, both Akiyama et al. and Trahey et al. presented early experimental results examining the effects of lateral, axial, and out-of-plane motion on the correlation peak. Later, Bohs and Trahey *(Bohs, 1991)* and Ramamurthy and Trahey *(Ramamurthy, 1991)* presented more

detailed results examining the effects of various parameters on the accuracy of 2D correlation tracking.

One of the most important parameters is the size of the windowed target region block. In general, a larger size window produces better results since it has a more unique speckle pattern than a smaller window. The weakness of large windows is that it will result in a decreased spatial resolution and increased computation time *(Hein, 1993)*.

Another important parameter affecting the performance of correlation search algorithms is whether RF data or envelope-detected data is used. RF data is cyclic in nature and thus contains phase information, which disappears in the envelope detection process. This phase information contributes to the uniqueness of speckle patterns that increases the probability of finding a correct match *(Hein, 1993)*. Ramamurthy and Trahey and Bohs and Trahey have shown that RF processing has better performance than envelope-detected processing, particularly for motion in the axial direction *(Bohs, 1991; Ramamurthy, 1991)*. This is so because of the autocorrelation length of speckle in the axial direction which is typically much smaller for RF than envelope-detected data *(Bohs, 1991; Ramamurthy, 1991)*.

3.3.3 Searching algorithms

Searching trials reduce the number of shifts required in order to find the best match and are based on the assumption that the matching function decreases as the search moves away from the direction of movement *(Hein, 1993)*.

In 2006, Zahiri-Azar and Salcudean introduced an innovative method, based on the standard time domain cross correlation strain estimation (TDE), for real time motion tracking in ultrasound imaging *(Zahiri-Azar, 2006)*. The proposed technique, named time-domain cross-correlation with prior estimates (TPDE), uses prior displacement estimates of neighboring windows to guide the search in a very small area and, consequently, speed up the computation *(Zahiri-Azar, 2006)*.

3.3.3.1 Standard Time Domain Cross Correlation Estimator (TDE)

Using the Standard Time Domain Cross Correlation Estimator (TDE) technique small displacements are obtained from the position of the maximum peak of the cross-correlation function calculated over a predefined search region between pairs of windowed ultrasonic images that are acquired under different axial deformations *(figure 3.5) (Zahiri-Azar, 2006)*. The exact position of the peak is usually calculated by interpolation. The corresponding value of the normalized correlation at the peak position is an indicator of the accuracy of the displacement estimate *(Zahiri-Azar, 2006)*.
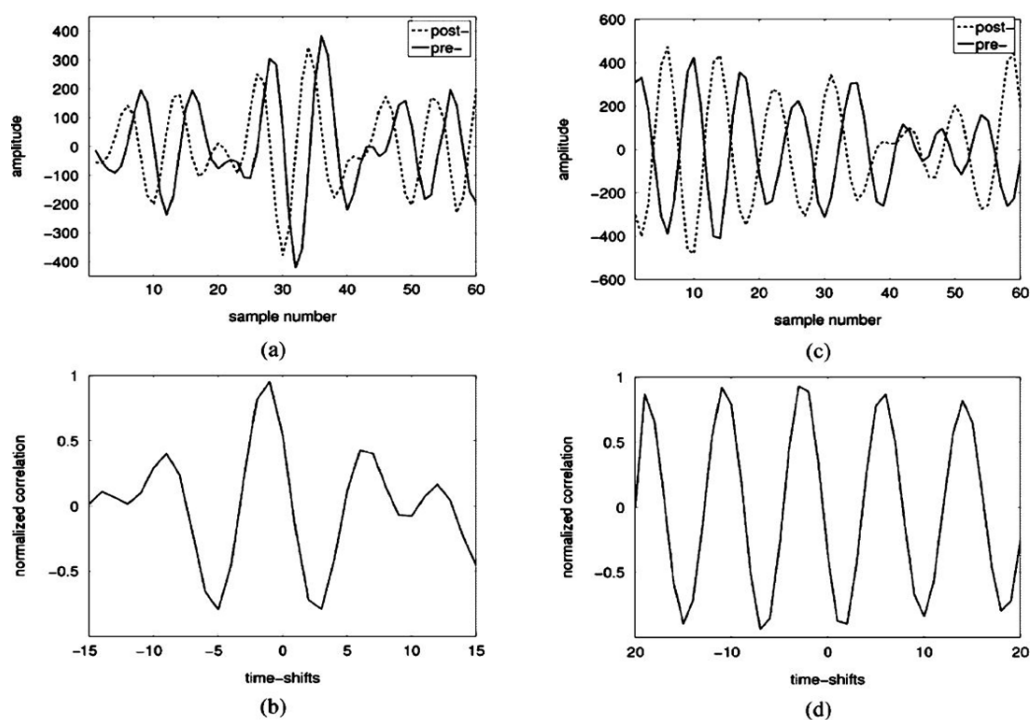
Figure 3.5 Pre-compressed and post-compressed RF data (a), (c) and corresponding normalized cross-correlations (b), (d) *(Zahiri-Azar, 2006)*.

3.3.3.2 Time Domain Cross Correlation with Prior Estimates (TDPE)

TDE is not used in real time applications because of its computational inefficiency *(Zahiri-Azar, 2006)*. Searching over a large area makes the algorithm slow. In addition, TDE can give a "false peak" when a secondary correlation peak exceeds the true peak *(Zahiri-Azar, 2006)*. TDPE algorithm exploits the fact that neighboring windows in an RF frame correspond to tissue regions that are close to each other *(figure 3.6)* and that have similar displacements because of their physical proximity *(Zahiri-Azar, 2006)*. TDPE is similar to

TDE, but it gathers information about the displacements of neighboring blocks and uses them to predict and reduce correlation peak search areas to small regions *(Zahiri-Azar, 2006)*. Typically, only 3 lags inside the predicted brackets need to be checked to detect the displacement quickly and with high accuracy *(Zahiri-Azar, 2006)*. Thus, TDPE becomes much faster than TDE. It also becomes more accurate and without false peaks because, in the small region employed, the correlation coefficient has a single peak, which is easy to detect *(figure 3.7) (Zahiri-Azar, 2006)*.

In the plane of an ultrasound image, except for boundary windows, each window has four main adjacent neighbors - a leading window to the left and a lagging window to the right on the same RF line, and windows at the same position on the upper and lower RF lines *(figure 3.6) (Zahiri-Azar, 2006)*. The displacement estimates of the leading window (previous window) and of the window at the same position on the upper RF line (upper window) have already been calculated and can be used to bracket the displacement of the current window *(Zahiri-Azar, 2006)*. Moreover, since the motion tracking is done with respect to the probe, the displacements gradually increases from the first window of each RF A-line as one moves away from the transducer *(Zahiri-Azar, 2006)*. This fact can be used as an initial guess to bracket the search area for each A-line. The prediction of the search bracket from one window to the next may generate occasional errors. These are due to: (i) the complex deformation of tissue being imaged that does not always follow the compression direction; (ii) existence of internal motion due to heart beat or breathing that makes the motion unpredictable; (iii) the way the compression is applied to the tissue; (iv) poor ultrasound SNR *(Zahiri-Azar, 2006)*.

Therefore, to validate the estimated displacement the correlation coefficient is checked. If the prediction leads to poor correlation (e.g., <0.9) the algorithm ignores the prediction and runs a full search over a predefined search region to find the displacement of the current window *(Zahiri-Azar, 2006)*. This "recovery search" in the TDPE is only triggered if the prediction fails. Using recovery search makes it possible to run the algorithm on an arbitrary region of interest rather than on a full image, if needed *(Zahiri-Azar, 2006)*.

Similar to the TDE method, TDPE splits each RF line into a number of windows. Finding the displacement is done in a raster scan starting from the window closest to the probe in the first RF line (top) and moving away from the probe (right), then continuing the process along each RF line *(Zahiri-Azar, 2006)*. At the first window of each RF line the correlations for lag values of -1, 0 and lag +1 are calculated and saved (3 lags). A three-point parabolic interpolation is then applied to find the exact position of the correlation peak. Then, the corresponding correlation coefficient at the peak position is computed. If the result exceeds the correlation accuracy threshold, the displacement estimate is recorded. For all other windows, the search area will be from Round(previousWinDisplacement) -1 to Round(previousWinDisplacement) +1 *(Zahiri-Azar, 2006)*.

If the prediction results in a poor correlation, the recovery search will be triggered and the algorithm will run a full search to find the displacement of the current window *(Zahiri-Azar, 2006)*.
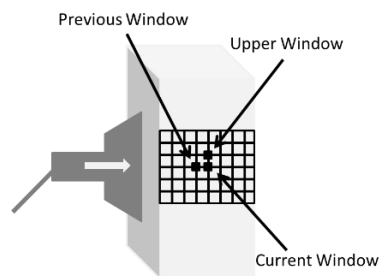
Figure 3.6 TDPE exploits the fact that displacements of previous neighbors have already been calculated. Previous and upper windows are shown.
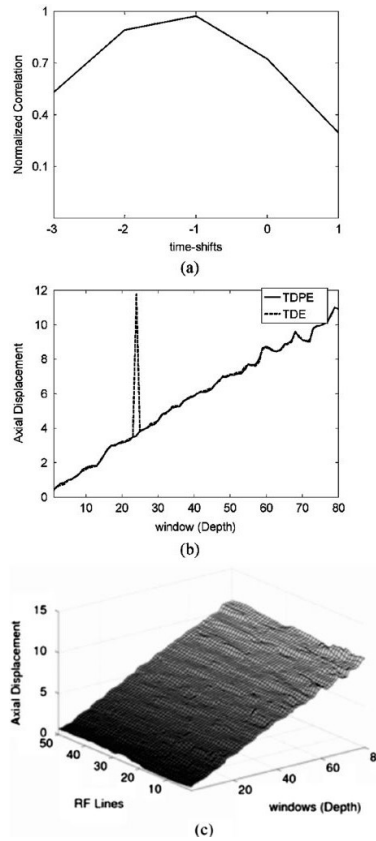
Figure 3.7 TDPE uses the information from neighboring windows to reduce the search area to a very small region. (a) The correlation peak is easy to find and false peaks do not occur. The displacement vector for a single RF line (b) and the displacement image for the complete RF frame (c) show how search bracketing lessens the change of finding false peaks *(Zahiri-Azar, 2006)*.

Spatiotemporal Clutter Filtering of Ultrafast Ultrasound Data

4.1 Introduction

Over the last decades, extensive work has been conducted in order to reject clutter signals originating from stationary and slowly moving tissue as they are the main source of artifacts in ultrasonic blood flow imaging *(Bjaerum, 2002).* Clutter suppression remains a crucial and challenging step in visualizing blood flow because tissue echoes and blood scatters echoes tend to share common characteristics, in particular when blood flow velocities become low or when tissue motion is too large. In these specific configurations conventional clutter filters fail because of the underlying assumption on which they are built. In fact, in conventional PD studies, clutter filtering has always been performed under the hypothesis that tissue motion is primarily of low velocity and thus corresponds to low frequency whereas red blood cells are fast moving scatters, meaning that demodulated tissue and blood signals have non-overlapping spectra centered on the zero frequency and the Doppler frequency respectively *(Demanè, 2015)*. Because of this temporal dynamic assumption, the raw ultrasonic signal is filtered along the temporal dimension using finite impulse response (FIR) or infinite impulse response (IIR) filters *(Willemetz, 1989; Tysoe, 1995).* IIR filters present the advantage of having steeper roll-off than FIR for a given order, but they exhibit a long settling time because of the lack of correct outputs for the first temporal points. FIR filters present a short settling time but require a higher order to efficiently discriminate clutter from blood signal. In both situations a limitation arises: due to the real time requirement and the use of focused ultrasonic beams to compute the image, the number of temporal samples in each spatial location is low (typically 8 to 16) and those filters are extremely difficult to optimize for a general Doppler imaging application ranging from cardiac imaging to microcirculation imaging.

Ultrafast ultrasound imaging enables to acquire a wild field of view at frame rates of several kHz. Mace et al. demonstrated that Ultrafast Doppler imaging improved Doppler sensitivity by a factor up to 30 compared to conventional Doppler imaging *(Mace, 2013).* This is in large extent due to the temporal ensemble length of an Ultrafast Doppler

dataset compared to a conventional Doppler dataset. Since Ultrafast Doppler does not need electronic sweeping of the focused beam along the transducer array, temporal samples are acquired simultaneously in every pixel of the image, meaning that for 1 second acquisition at 1 kHz of frame rate, each pixel exhibits 1000 temporal points. The settling time of temporal filter is no longer an issue and high order IIR with step roll-off can be used as long as the first tens of temporal points are removed from the signal. However, spectral filters continue to fail in discriminating between tissue and blood flow in case of slow blood flows or fast-moving tissue where both spectra overlap. Demanè et al. proposed a new way of rejecting clutter signals from Ultrafast Doppler datasets using Singular Value Decomposition (SVD) *(Demanè, 2015)*.

4.2 The Specificity of Ultrasound Signal

The following sections refer to Demanè et al., 2015.

4.2.1 The Different Component of Ultrasound Signal

An ultrafast Doppler acquisition consists in a stack of beamformed ultrasound images and can be represented under the variable *s(x,z,t)*, where *x* stands for the lateral dimension (along the transducer array), *z* stands for depth in the medium in front of the ultrasonic probe, and *t* stands for time. The signal can be described as the summation of three contributions - c the clutter signal, *b* the blood signal, and *n* the electronical/thermal noise:

$$s(x, z, t) = c(x, z, t) + b(x, z, t) + n(x, z, t) \qquad (4.1)$$

n can be considered as a zero-mean Gaussian white noise. Although these three contributions have both spatial and temporal different characteristics, in most applications only the temporal information has been exploited because the hypothesis discriminating between tissue signal and blood scatters signal focused on their different spectral content. However, the spatial characteristics of these signals also convey different information. In fact, tissue is far deformable than a red blood cell arrangement in plasma, and a small movement of tissue can be seen as a spatial shift of a speckle pattern whereas a movement of red blood cells implies a reorganization of the scatters generating a different speckle pattern. This means that tissue signal has a higher spatial coherence than blood signal in ultrasound imaging. Moreover, depending upon the

ultrasound frequency used for the acquisition, the backscattered energy of the blood signal can be 10 to 60 dB lower than energy of the tissue signal *(Demanè, 2015)*.

4.2.2 Covariance Matrix of Neighboring Pixels

To compare spatially close temporal signals, a simplified signal is considered:

$$\tilde{S}(x, z, t) = s(x, z, t) \cdot \overline{s(x, z, t)}^* / \left| \overline{s(x, z, t)} \right|^2 \tag{4.2}$$

where $\tilde{s}$ is the time average value of s and * stands for complex conjugate *(Demanè, 2015)*. This simplification allows to get rid of any phase shift (via the product with the complex conjugate of the time averaged signal) and of amplitude difference (via the division with the squared modulus) between two pixel signals and thus to compare signals only according to their shape *(Demanè, 2015)*. *Figure 4.1* shows that in neighboring pixels, simplified signals present very similar low frequency variations (tissue motion), whereas the rapid fluctuations (blood motion) do not present the same pattern from one pixel to another *(Demanè, 2015)*. This aspect is further investigated in *figure 4.2*, where the nine pixel signals of the second neighborhood of *figure 4.1* are divided in blood (HF – high frequency) and tissue (LF – low frequency) signals with a temporal filter *(Demanè, 2015)*. As noticeable, tissue signal is highly correlated and the covariance matrix of those nine signals shows a high degree of correlation, whereas the blood signal covariance matrix is almost diagonal, meaning that blood signal is poorly spatially coherent, even at a very local scale *(Demanè, 2015)*. *Figure 4.1* even shows that at large spatial scales, tissue signal is still quite coherent as the simplified signals are quite similar in shape between the two neighborhoods *(Demanè, 2015)*. Therefore, tissue signal could be condensed in a few temporal signals accompanied by a set of spatially arranged complex coefficients required to recover the amplitude and phase shift proper to each pixel *(Demanè, 2015)*. Hence, tissue signal realization in all pixels forms a family of vectors whose cardinality is much higher than the dimension of the tissue vector subspace. Contrary to tissue signal, blood signal is not assumed to have high spatial coherence *(Demanè, 2015)*.
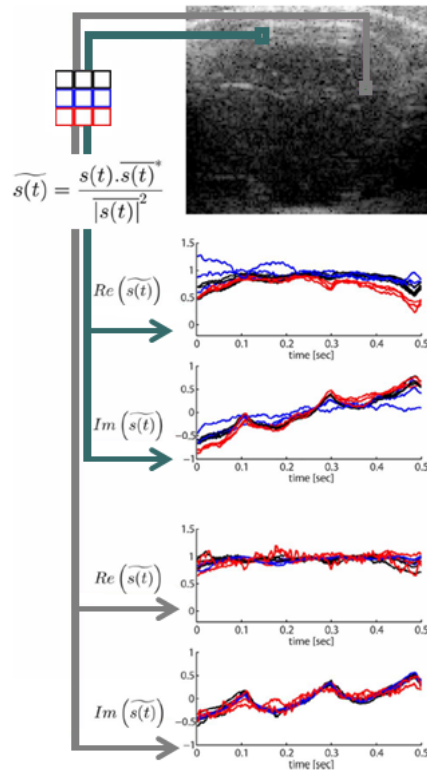
Figure 4.1 The top image depicts *s(x,z,t = 0)* of an Ultrafast acquisition acquired during 0.5 s at a frame rate of 500Hz, on the brain of a thinned skull rat (*scale bar = 1mm*). To have an insight into the temporal dimension of this Ultrafast acquisition, two neighborhoods of nine pixels have been chosen in the image (grey and green squares). Inside each pixel, the simplified signal is calculated. $\bar{s}$ is then plotted with color respective to the position in the nine pixel neighborhood (black, blue or red). This illustrates that signal in close pixels is very similar in shape *(Demanè, 2015)*.
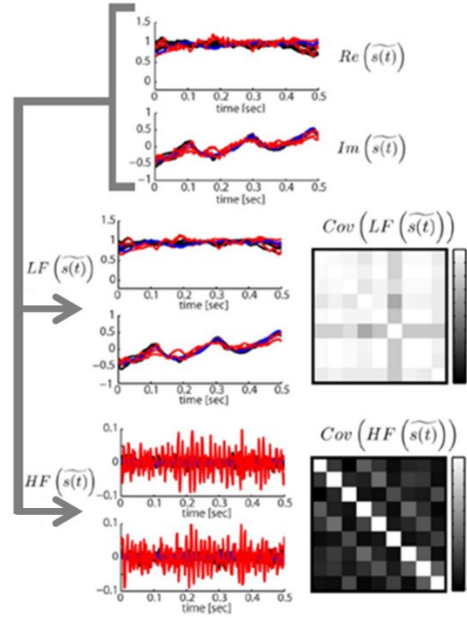
Figure 4.2 The same data in the grey nine pixel neighborhood of *figure 4.1* are filtered using a 50Hz cut off 4th order Butterworth filter typically used to discriminate between tissue and blood flow signals. The low frequency (LF) part of the nine pixel temporal signal are really similar in shape and seem highly correlated, whereas the blood signal (HF) seem highly decorrelated. On the right are displayed the *9 x 9* covariance matrix (magnitude) of the normalized zero-mean complex signals, for the low frequency and high frequency part respectively. HF blood signal is indeed highly decorrelated compared to LF tissue signal *(Demanè, 2015)*.

4.3 Singular Value Decomposition of Ultrafast Ultrasonic Data

Let consider the spatiotemporal matrix form of *s(x,z,t)* corresponding to the raw data cineloop acquired during an ultrafast acquisition. *s(x,z,t)* corresponds to set of n_x x n_z x n_t samples where n_x, n_z and n_t are respectively the number of spatial samples along the *x* direction, the number of spatial samples along the *z* direction and the number of time samples *(Demanè, 2015)*. The raw data matrix is reshaped under a Casorati matrix form by transforming time series data into a 2D space-time matrix form *S* of dimension (n_x x n_z, n_t) *(Demanè, 2015)*. The singular value decomposition (SVD) of this Casorati matrix *S* is written as

$$S = U\Delta V^*$$ (4.3)

where *Δ* is a non-square *(n_x x n_z, n_t)* diagonal matrix with diagonal coefficient λ_k; *U* and *V* are orthonormal matrices of rank n_t with respective dimension *(n_x x n_z, n_x x n_z)* and *(n_t, n_t)*,

and * stands for the conjugate transpose *(Demanè, 2015)*. Columns of *U* and *V* correspond respectively to the spatial and temporal singular values of *S*. This decomposition can be made so that the coefficients in the diagonal matrix *Δ* are sorted in a descending order *(Demanè, 2015)*. In that case tissue signal with higher energy and higher spatiotemporal coherence will be concentrated on the first singular vectors. Thus, a suppression of the tissue signal can be achieved by using a "brick-wall" filtering matrix I^f that removes the contribution of the first singular values from the original signal *(Demanè, 2015)*. This gives the filtered signal S^f:

$$S^* = U\Delta I^f V^*$$ (4.4)

This matrix I^f is diagonal and the first *N* diagonal coefficients are zeros whereas the remaining diagonal coefficients are ones *(Demanè, 2015)*.

4.4 Implementation of the SVD Filter

The first step is presented in *figure 4.3(a)* and consists in rearranging the Ultrafast Doppler acquisition into a 2D Casorati matrix where one dimension is space and the other dimension is time *(Demanè, 2015)*. SVD could be performed on this matrix and directly give the new temporal singular vector basis and the new spatial singular vector basis *(Demanè, 2015)*. However, in most cases the Ultrafast Doppler acquisition presents many more spatial points (typically several 10 000) than temporal points (several hundreds or thousands), and it can be less demanding from a computing point of view to first form the n_t x n_t covariance matrix *(figure 4.3(b))* and diagonalize it. This gives n_t temporal eigenvectors that are the right singular vector V_i of *S (Demanè, 2015)*. *Figure 4.4(a)* shows the spectral content of those eigenvectors sorted by decreasing eigenvalue. The largest eigenvalues are associated with the temporal singular vectors presenting the slowest variation *(Demanè, 2015)*. This is consistent with spatially coherent tissue signal supposed to be quite similar in neighboring pixels in a way that enables to reduce the realizations of tissue temporal signal on a much smaller subspace *(Demanè, 2015)*. As a consequence, tissue signal is supposed to be condensed in the first singular vectors whereas blood and noise signals are described by the singular vectors associated with lower singular values *(Demanè, 2015)*. The eigenvalue itself is closely related to the energy associated the corresponding singular vector and *figure 4.4(b)* shows the relative variation of those singular values: the dashed red line shows that with a threshold of 50 rejected singular

values *(see figure 4.5)* the SVD clutter rejection will discriminate the supposedly tissue from a signal 30 dB below, which is really consistent with the expected relative difference between tissue energy and blood energy at that range of US frequencies (15 MHz) *(Demanè, 2015)*. The weighted spatial vector $\lambda_i U_i$ are then computed by the projection as described in *equation 4.4*. Finally, using this decomposition, *s(x,z,t)* can be decomposed on both a temporal basis and a spatial basis of singular vectors *(figure 4.5)*. Based on the assumption that tissue signal is gathered in the first singular vectors, clutter rejection is performed using a threshold *n* on the number of singular vectors removed from the raw signal *(Demanè, 2015)*:

$$S_{blood}(x, z, t) = s(x, z, t) - \sum_{i=1}^{n} \lambda_i I_i(x, z) V_i(t) \tag{4.5}$$

Then, the energy per pixel can be computed to produce the so-called Power Doppler image:

$$PW(x, z) = \int |S_{blood}(x, z, t)|^2 dt \tag{4.6}$$
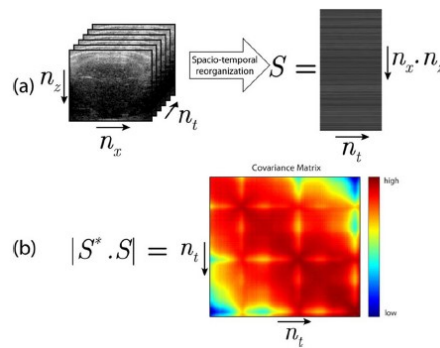
Figure 4.3 (a) The ultrafast Doppler acquisition forms a 3D stack of images with two spatial dimensions and one temporal dimension. It is reshaped in one spatiotemporal representation (Casorati matrix) where all pixels at one time point are arranged in one column. Thus, all time points for one pixel are arranged in one row. **(b)** The covariance matrix is presented here in magnitude and is of dimension n_t x n_t *(Demanè, 2015)*.
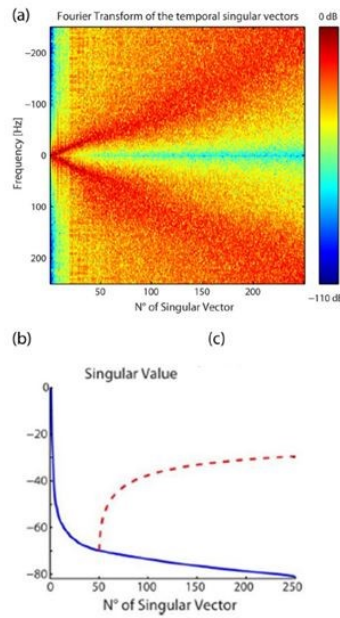
Figure 4.4 (a) Spectral content estimation of all the right singular vectors, sorted with decreasing singular value. Low frequency temporal signals are associated with the highest singular values. As all singular vectors are normalized, energy in all spectra (all columns) is equal to one. **(b)** Singular values of the matrix Δ (solid blue) expressed in dB and cumulative sum of those singular values from n° 50 (dashed red) *(Demanè, 2015).*
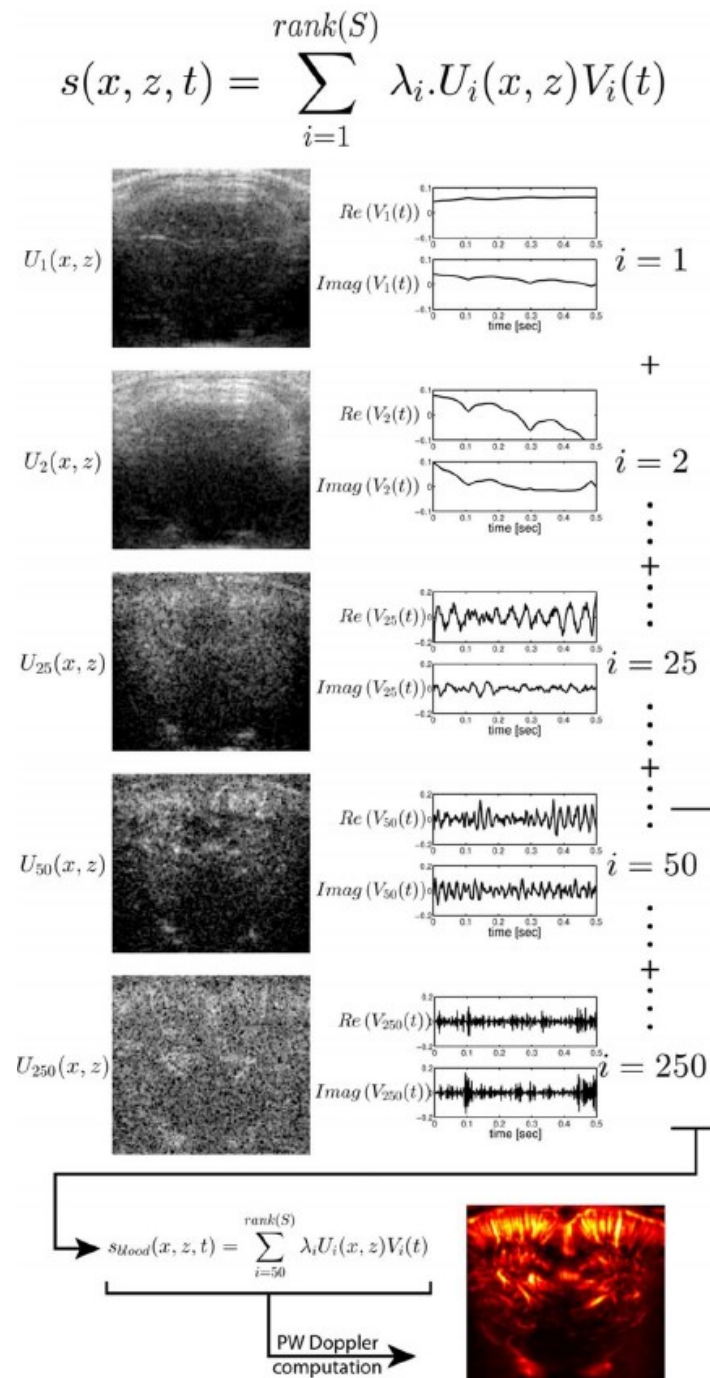
Figure 4.5 The Ultrafast acquisition is decomposed by the singular value decomposition into a set of spatiotemporal couples of vectors. The crucial point is that tissue signal is coherent enough to be quite similar over the entire image, and that it can be described by a set of vectors constituting a subspace of the temporal space, but much smaller. Indeed, by rejecting the first 49 couples of singular vectors, tissue signal is rejected and a very good PW Doppler image of the vascularization in the rat brain is obtained *(Demanè, 2015).*

4.4.1 SVD Thresholding

SVD thresholding can be performed using four different types of methods *(Baranger, 2018)*.

Arbitrary Thresholding

The basic intuitive approach is to manually tune the threshold *N* for a given acquisition, until the resulting PD image is acceptable. For several examples in a certain clinical setup a manual estimation can be performed, giving rise to a lookup table with present thresholds for a range of particular experimental conditions. This arbitrary thresholding relies on qualitative criteria and assume that the clutter is comparable from one acquisition to another as long as imaging conditions are similar. Being parametric and independent of the real ultrasonic signal characteristics, the arbitrary threshold may exhibit a lack of robustness *(Baranger, 2018)*.

Estimators based on the Singular Values

As the singular vectors are normalized *($\forall i\ U_i^* \cdot U_i = 1$ and $\forall i\ V_i \cdot V_i^* = 1$)*, the amount of energy in a particular couple of singular vectors is entirely contained in the singular value λ_i. A first idea is to reject singular values above a certain threshold in dB, *(figure 4.6, blue dashed line) (Baranger, 2018)*. In certain conditions of tissue motion and blood flow speed, the best threshold is found and the corresponding dB level is computed. This dB level is then used to estimate the threshold in another set of tissue motion and blood flow speed. However, this approach does not take into account that tissue and blood flow are decomposed on two multidimensional subspaces, and that it is more relevant to consider the energy associated with a space spanning over a subspace of singular vector, i.e. the sum of the associated singular values *(Baranger, 2018)*. Therefore, a second idea is to consider the overall signal as an additive combination of a tissue signal and a blood signal *(Baranger, 2018)*. Therefore, given an ultrasound emission frequency, a characterized transducer and standard echogenicity conditions in a certain organ, the tissue signal and blood signal have a given backscattered energy *(Baranger, 2018)*. It can then be decided to choose the threshold when the ratio between the cumulative sum of the blood singular values and the overall signal energy, defined as the sum of all singular

values *(equation 4.7)*, reaches a certain (negative) dB level *(figure 4.6, orange dashed line)* *(Baranger, 2018)*.

$$\frac{\text{Blood energy}}{\text{Blood energy}} = \frac{\sum_{k=N}^{\text{Rank}(S)} \lambda_k}{\sum_{k=1}^{\text{Rank}(S)} \lambda_k} \qquad (4.7)$$

The last idea is a non-parametric one. The blood flow signal can be thought as an intermediate between the highly coherent tissue signal and the Gaussian image noise *(Baranger, 2018)*. In fact, SVD of in vivo ultrafast imaging data usually exhibits 3 different regimes of singular value decrease *(figure 4.6, blue curve) (Baranger, 2018)*. The first regime is supposed to be related to tissue components and the clutter rejecting threshold is chosen as the first turning point of the singular value curve *(blue dotted line)*, given by the first local minimum of the curvature radius *(Baranger, 2018)*.
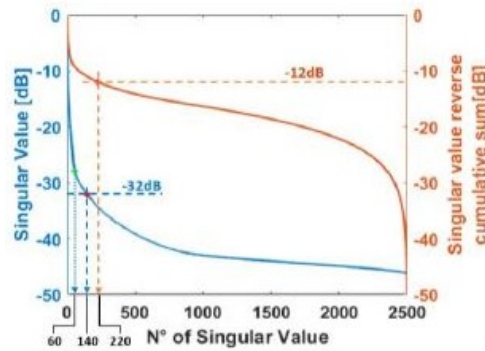
Figure 4.6 Energetic criteria for thresholding selection. Singular values of the matrix *Δ* (solid blue) and blood subspace energy (solid orange) computed as the reverse cumulative sum of singular values. Acquisition on the brain of a neonate. A first natural threshold can be obtained by arbitrarily defining a magnitude above which the singular values are considered to represent tissue signal (dashed blue). Here, a magnitude chosen at −32dB would result in a threshold at 140. Same approach can be done for the blood energy curve: a cutoff chosen at −12dB (dashed orange) gives a threshold of 220. Another threshold is the turning point of the singular value curve (dotted blue), which here gives a threshold of 60 *(Baranger, 2018)*.

Estimators based on the Singular Vectors V

Tissue and blood flow are generally assumed to exhibit distinct frequency content. Therefore, it can be assumed that the temporal vectors follow the same trend *(Baranger, 2018). Figure 4.7 (a)* shows the power spectral density (PSD) of all temporal vectors for an

acquisition on a neonate's brain *(Baranger, 2018)*. As noticeable, the spectra are almost equally spread between positive and negative frequencies, implying that most spectral statistics, such as the central frequency, have to be computed side-by-side of the band *(Baranger, 2018)*. For each temporal singular vector, the PSD-weighted central frequency (f_c, first statistical moment) and standard deviation (STD, second statistical moment) of the considered half band were computed *(Baranger, 2018)*. The central frequency and the STD increase with the singular vector index. Tissue signal generally has a narrower bandwidth than blood flow signal. This behavior is shown by the evolution of the bandwidth containing 99% of the energy *(figure 4.7, a)*, which is computed over the whole frequency band (two-sided) *(Baranger, 2018)*. For each of these 3 spectral statistics, two SVD threshold estimators can be defined. Firstly, singular vectors can be assumed to be in the tissue subspace while their central frequency, frequency STD or 99% bandwidth lies below a given cutoff *(Baranger, 2018)*. For instance *(figure 4.7, b)*, singular vectors whose central frequency are below 100Hz are thought to be tissue representatives, which boils down to a tissue/blood threshold of *N = 75*. Secondly, non-parametric estimators can be defined by the first inflexion point of these curves *(figure 4.7, b, green arrows)*, following the idea that these spectral statistics experience a change of regime around the transition between tissue and blood subspaces *(Baranger, 2018)*.
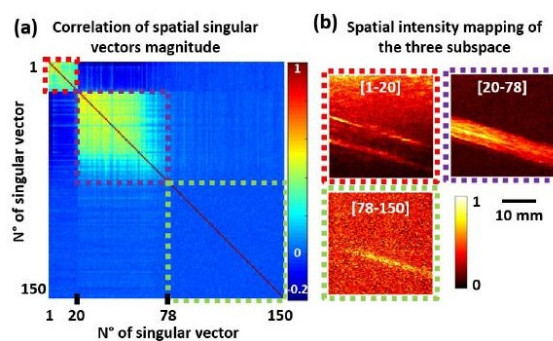
Figure 4.7 Spatial criteria for threshold selection. **(a)** Incoherent correlation matrix of spatial singular vectors, for a plane wave ultrafast Doppler acquisition on a flux phantom. Three highly correlated areas appear. **(b)** Spatial vectors are incoherently averaged in the 3 areas, giving intensity maps. From 1 to 20 (red dotted squares), vectors describe the tissue and the canal walls. From 20 to 78 (purple dotted squares), spatial vectors represent the blood flow. From 78 to 150, spatial vectors account for mostly noise, yet with remaining blood signal *(Baranger, 2018)*.

Estimators based on the Singular Vectors U

From $S = U\Delta V^*$, it is possible to write S as the sum of multiple separable matrices $u_k v_k^*$, of size ($n_x \times n_z$, n_t), weighted by the singular value λ_k where u_k and v_k are respectively the *k-th* column vector of *U* and *V (Baranger, 2018)*:

$$S = \sum_{k=1}^{n_t} \lambda_k \cdot u_k v_k^* \qquad (4.8)$$

Each vector u_k has a size *($n_x \times n_z$, 1)* and then could be rearranged in the shape of a 2D image of size *(n_z, n_x) (Baranger, 2018)*. Therefore, each matrix $u_k v_k^*$ can be thought as an image of intensity *|u_k|*, with a pixel-specific phase shift *arg(u_k)*, and modulated along time by a complex signal *v_k* (the symbols modulus *| |* and argument *arg ()* being applied to each components of *u_k*) *(Baranger, 2018)*. If it is assumed that the tissue signal and the blood signal have different spatial distributions, then the *|u_k|* vectors should be correlated within the tissue subspace and within the blood subspace, but not between them *(Baranger, 2018)*. This assumption on the spatial distribution is widely observed experimentally, with the tissue being spread in the whole field of view, with high spatial and temporal coherence, and the blood being restricted to the vascular network, with lower spatial and temporal coherence *(Baranger, 2018)*. Consequently, *C*, the correlation matrix of *|u_k|* $k \in$ *[1, n_t]* of size *(n_t, n_t)* should reveal the different subspaces. The calculation of *C* is given in the *equation 4.*9, where $\overline{u_n}$ and σ_n respectively stand for the mean and the standard deviation of *u_n* indexes *(Baranger, 2018)*.

$$C(n, m) = \frac{1}{n_x \cdot n_z} \cdot \sum_p^{n_x \cdot n_z} \frac{(|u_n(p)| - |\overline{u_n}|) \cdot (|u_m(p)| - |\overline{u_m}|)}{\sigma_n \cdot \sigma_m} \qquad (m, n) \in [1, n_t]^2 \qquad (4.9)$$

4.5 Motion-Corrected Spatio-Temporal Clutter Filtering

Nayak et al. demonstrated that large and periodic physiological motion and sonographer hand motion can significantly reduce the covariance of the spatiotemporal matrix, leading to suboptimal clutter rejection *(Nayak, 2018)*. Motion increases the rank of the tissue components, and therefore, a higher SV threshold should be used to efficiently suppress tissue clutter. This can reduce the sensitivity of detecting small vessels *(figure 4.8) (Nayak, 2018)*.
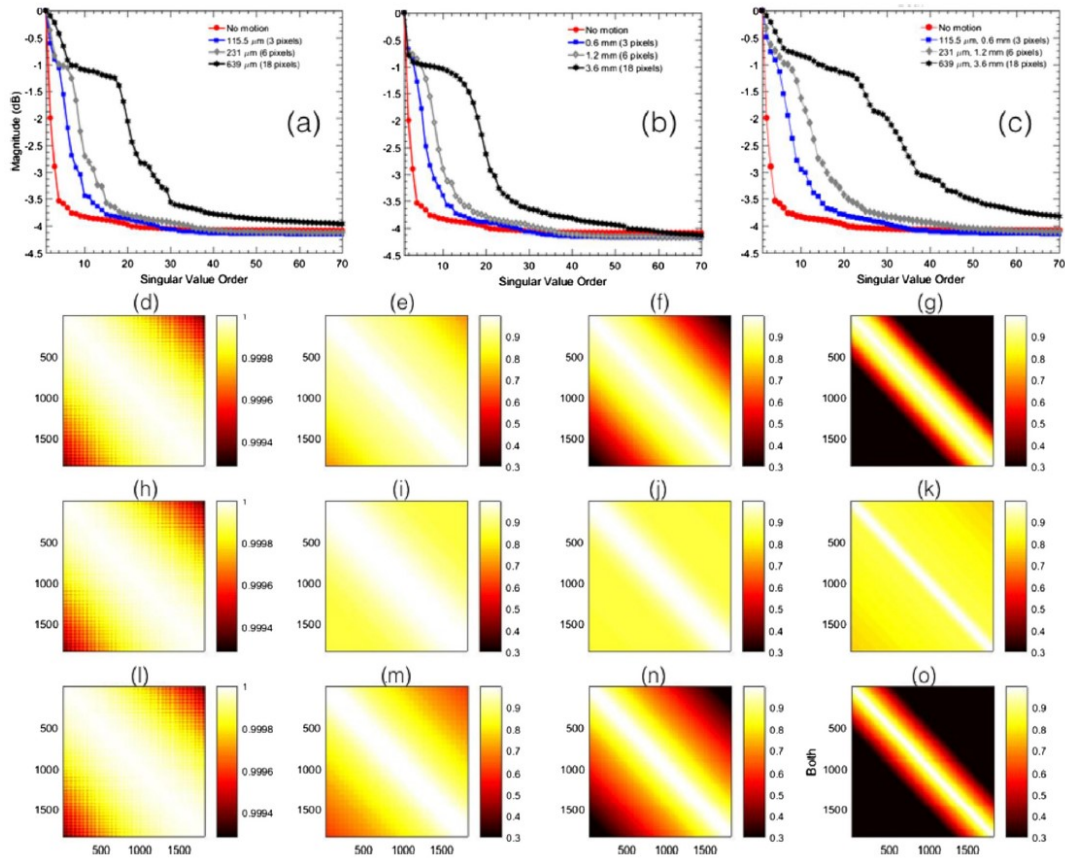
Figure 4.8 Singular value order and covariance of the spatiotemporal Casorati matrix obtained from the homogeneous phantom data with no blood activity. (a-c) Variation in the decay of the singular value order of the phantom data, with respect to increasing extent of motion in the uniaxial, unilateral and diagonal directions, respectively. (d-o) Corresponding covariance of the spatiotemporal Casorati matrix obtained in the absence of motion (d, h, l), and in the presence of motion of 3 (e, i, m), 6 (f, j, n) and 18 (g, k, o) pixels. Rows e-g, i-k and m-o represent uniaxial, unilateral and diagonal motion, respectively. *(Nayak, 2018).*

Moreover, Nayak et al. showed that even if tissue clutter is completely rejected in presence of motion, estimation of the cumulated PD signal from the motion affected clutter filtered data can be demanding because of the miss-registration of the ultrasound frames in the Doppler ensemble *(Nayak, 2018)*. Specifically, PD signal is computed from coherent integration of the clutter filtered signal. However, in presence of motion, which is considerable and unavoidable in thyroid imaging, signal incoherency due to spatial miss-registration of the ultrasound frames can significantly reduce image quality *(Nayak,*

2018). Additionally, imaging of blood flow in small vessels – usually characterized by low intensity back-scatter signals, can be particularly unreliable since motion can definitely corrupt its contribution because of incoherent integration *(Nayak, 2018)*. High frame rate imaging could possibly mitigate the impact of motion on small vessel. However, angular compounding of the ultrasound frames - required to increase the signal to noise ratio (SNR) of plane wave imaging, reduces the frame rate by up to an order of magnitude, eventually leading to increased motion between successive frames *(Nayak, 2018)*. Additionally, imaging frame rate is further reduced when imaging large or deep thyroid nodules because of the increased scan depth *(Nayak, 2018)*. Visualization of small vessel blood flow may be improved by injecting micro-bubbles-based contrast agents in the blood stream. However, this yields to increased complexity, cost and invasiveness *(Nayak, 2018)*.

To address this weakness, Nayak et al. introduced a first-order rigid body - based motion correction technique *(Nayak, 2018)*. Specifically, 2D normalized cross-correlation (NCC) - based speckle tracking technique was used to estimate tissue displacements, which were subsequently used for motion correction *(Nayak, 2018)*. Motion correction was performed on the clutter filtered ensemble prior to PD computation. The efficacy of the proposed technique was demonstrated on thyroid nodules *(Nayak, 2018)*. Results on 10 female patients with at least one thyroid nodule suspicious of malignancy showed that PD images of thyroid nodules were significantly degraded because of the large physiological motion due to thyroid proximity to the pulsating carotid artery *(Nayak, 2018)*. The resultant PD images were corrupted with signal distortion, motion blurring and occurrence of artificial shadow vessels and displayed visibly low signal-to-background contrast *(Nayak, 2018)*. Conversely, PD images obtained from the motion corrected ultrasound data addressed the issue and significantly improved detection and visualization of blood flow in small vessels *(figures 4.9, 4.10, 4.11 and 4.12) (Nayak, 2018)*. The SNR and the contrast-to-noise ratio (CNR) increased by up to 15.2 dB and 12.1 dB, respectively *(Nayak, 2018)*.
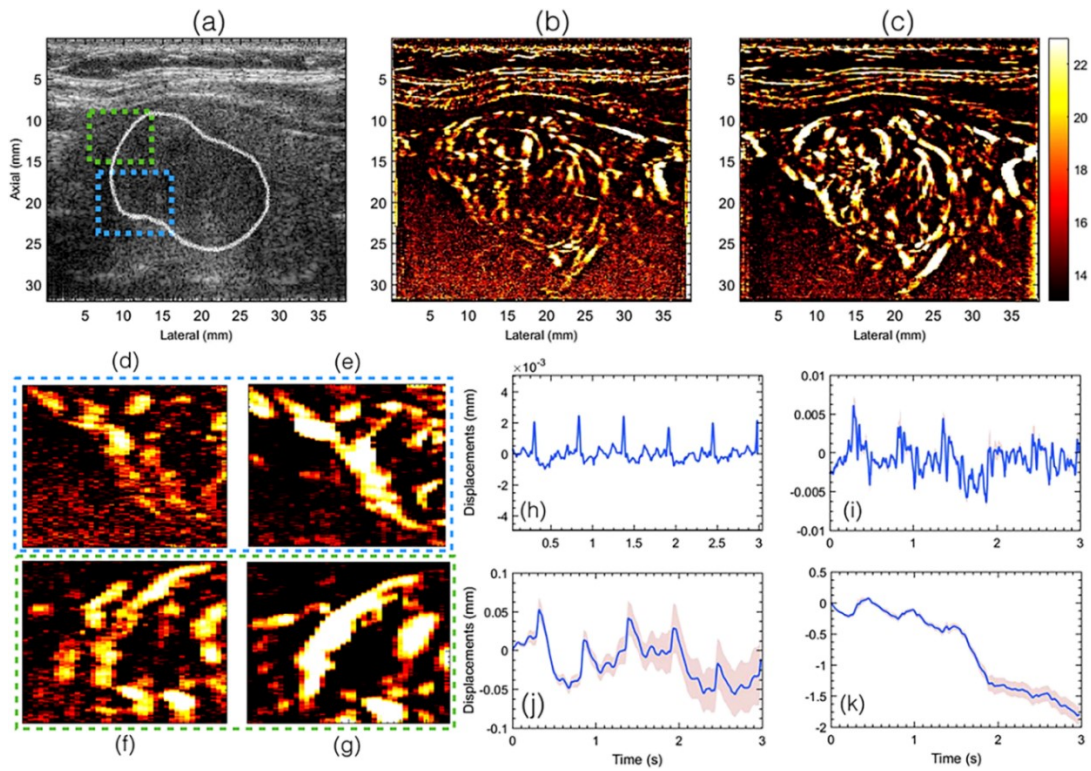
Figure 4.9 Plane wave B-mode sonogram, with ROIs in blue and green (a), and its corresponding PD images without (b) and with (c) motion correction. The outlines of the thyroid nodules are indicated in white in the B-mode sonogram. (d, f) show zoomed insets obtained from (b). (e, g) show zoomed insets obtained from (c). (h, i) and (j, k) display the axial and lateral displacements, respectively. (h, i) display the displacement associated with every consecutive frame, and (j, k) display the total accumulated displacements, with reference to the first frame in the ensemble. The continuous error band (red) displays ± 1 STD from the mean. *(Nayak, 2018).*
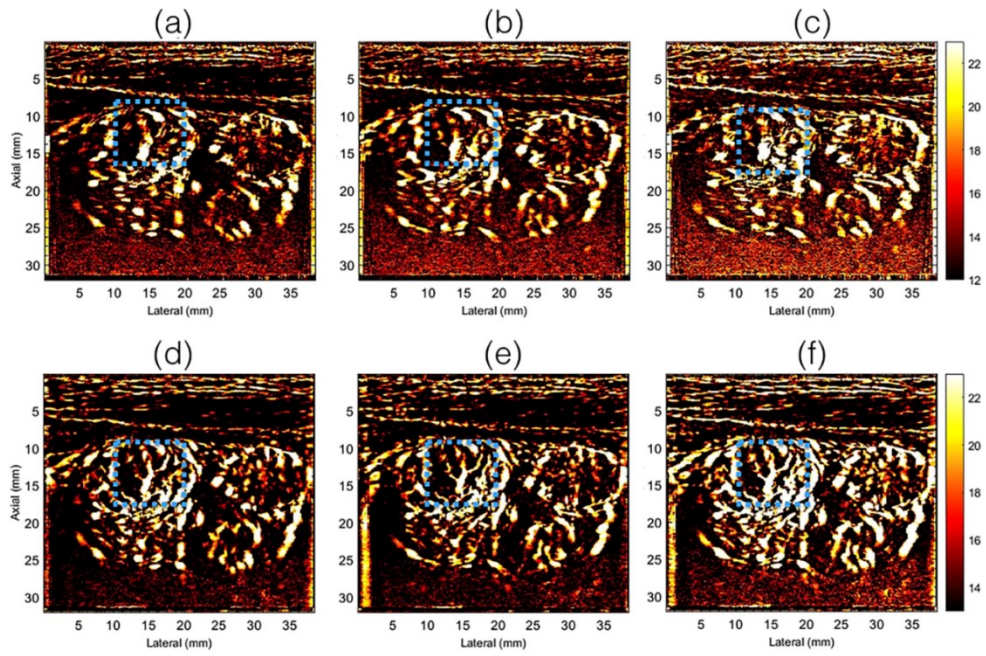
Figure 4.10 Half- and full- ensemble PD images obtained using clutter filtered Doppler ensemble, without (a-c) and with (d-f) motion correction. The half-ensemble PD images are displayed in (a, b, d, e) and the corresponding full-ensemble are displayed in (c, f). The blue ROI indicates a region for closer observation and comparison. *(Nayak, 2018).*
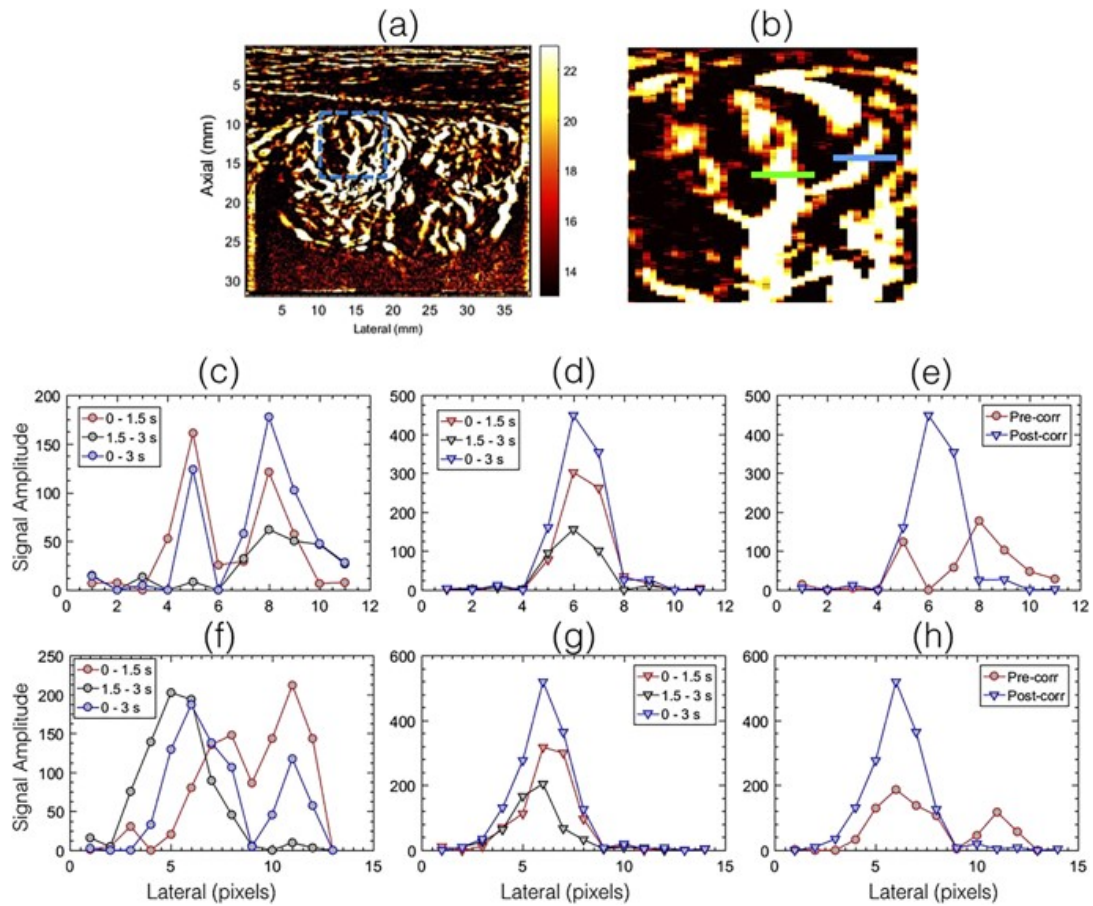
Figure 4.11 Spatial amplitude profile from the half- and full- ensemble PD images displayed in *figure 4.10* Signal amplitude profile (c-e) and (f-h) corresponds to the blue and green line segments in the zoomed inset (b) of the PD image in (a), respectively. In the absence of motion correction (c, f), coherent integration of the Doppler data was not feasible, which led to poor signal reconstruction. In the motion corrected data, the half-ensemble PD intensity profiles (d, g) were spatially registered, which produce a stronger peak (e, h). *(Nayak, 2018).*
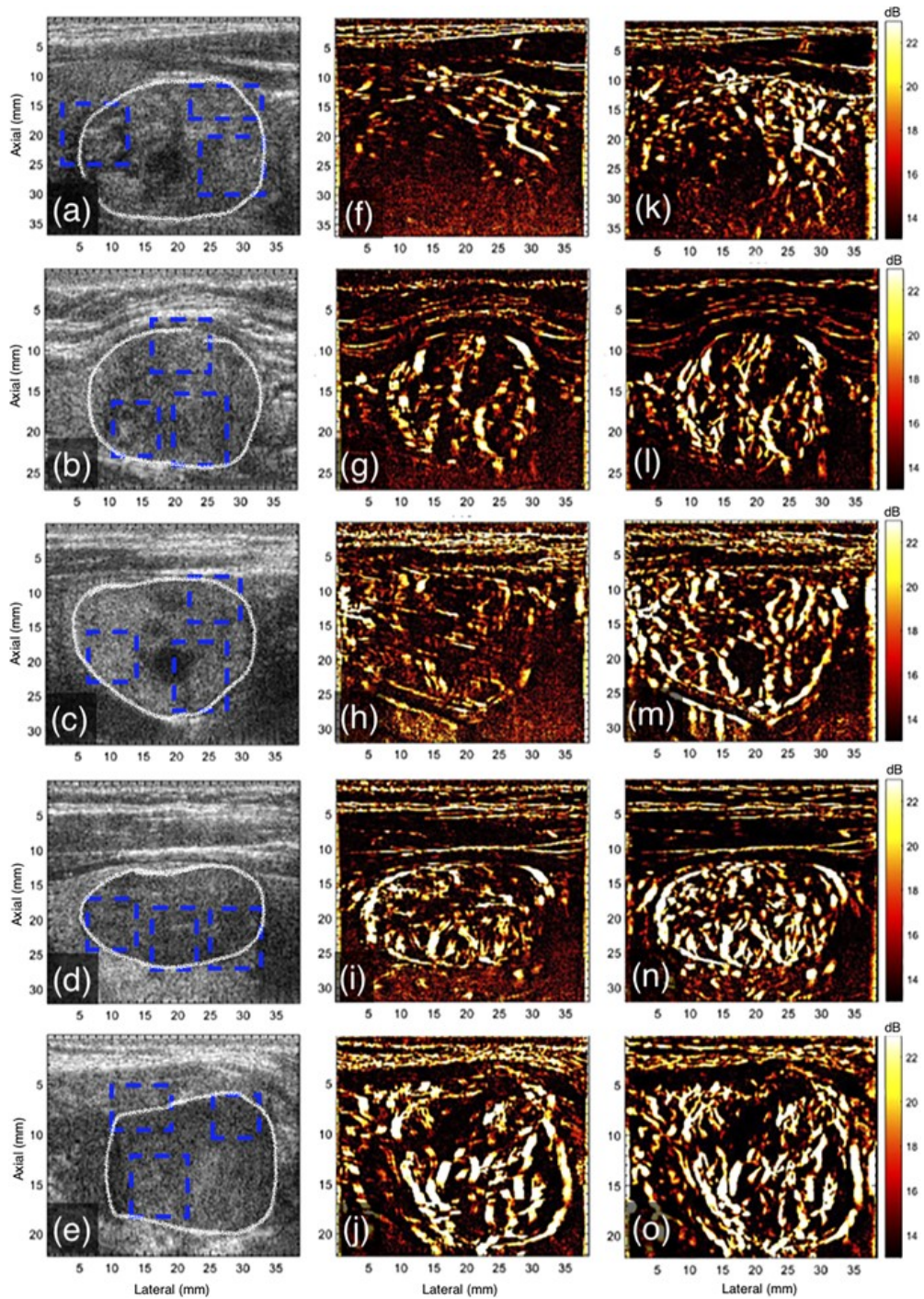
Figure 4.12 Plane wave B-mode sonograms (a-e) and the corresponding PD images without (f-j) and with (k-o) motion correction for patients 3-7, respectively. The outline of the thyroid nodules is indicated in white in the B-mode sonogram (a-e). *(Nayak, 2018).*

4.5.1 Motion Correction Performance Descriptor

Nayak et al. introduced a performance descriptor, named *Motion Matrix,* useful to quantitative assess motion correction performances *(Nayak, 2018)*. The motion matrix is

a visual representation of the correlation between any two given frames within an ensemble. An example of Motion Matrix is provided in *figure 4.13.* Both *x* and *y* axes show image frames plotted in a sequential order. The correlation coefficient (CC) between any two frames is computed using a 2D NCC – based speckle tracking technique. CC values are comprised in the range *(0, 1)*, where *CC = 1 (yellow)* indicates a perfect linear association and *CC = 0 (blue)* indicates that no linear association exists between two given frames. The diagonal of the matrix gives the CC of a frame against itself, and therefore, it shows the highest level of similarity, i.e. *CC = 1*. The mean correlation coefficient provides a quantitative descriptor of displacement tracking accuracy and consequently of motion correction efficacy. Furthermore, MM provides a quick visual aid to present motion. Translational and periodic motions as well as sharp and sudden changes in motion can be easily identified *(figure 4.14).*
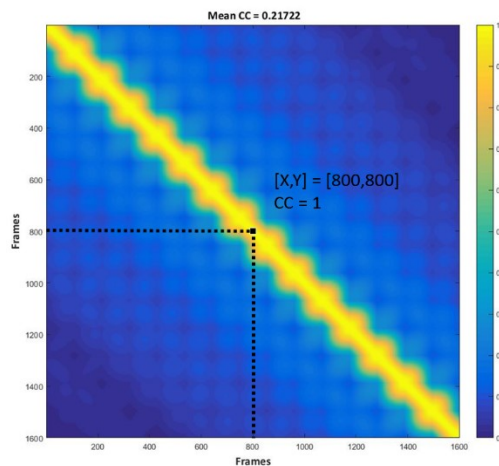
Figure 4.13 The motion matrix plots frames in sequential order and computes the correlation coefficient (CC) between any two frames within an ensemble. The diagonal of the matrix shows the correlation coefficient of a frame against itself, i.e. *CC = 1*. The mean CC provides a feedback on motion correction effectiveness.
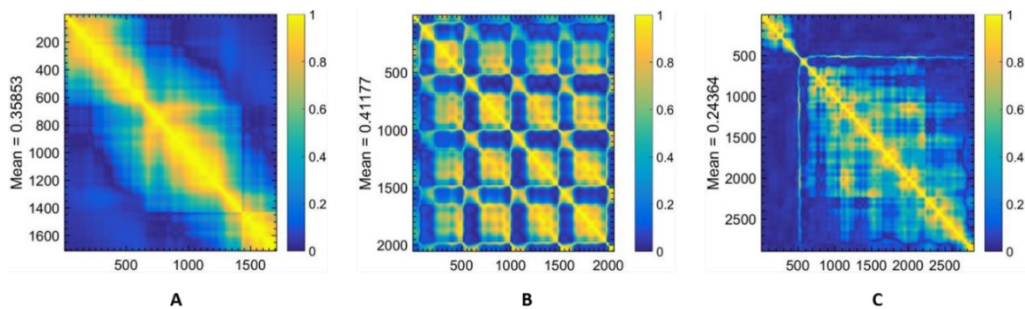
Figure 4.14 A. Linear motion, correlations move in diagonal. **B**. Periodic motion, correlations move alongside axes and motion is repeated every 300 frames. **C**. Out of

plane motion, regions where frames have almost no correlation with the rest of image ensemble can be identified.

4.5.2 Noise Bias Suppression

The background noise field used for the suppression of the PD image is estimated from the clutter-filtered Doppler ensemble (CFDE) *(Nayak, 2019)*. This is achieved in two steps:

1. Estimation of the synthetic noise image from the CFDE
2. Estimation of the background noise field from the synthetic image from the synthetic noise image based on low-rank approximation.

4.5.2.1 Estimation of the Synthetic Noise Image

A spatio-temporal filter (STC) is used to identify the flow pixels in the CFDE, which are replaced by randomly selected noise pixels from the local neighborhood, to generate the synthetic noise image *(Nayak, 2019)*. In particular, STC based filtering of the CFDE is performed locally overlapping kernels of dimension m x n x t pixels in axial, lateral and temporal direction, respectively *(Nayak, 2019)*. The pixels within the 3D kernel are arranged in the space-time Casorati form of dimension s x t, where s = m x n, and its normalized correction matrices M of dimension t x t are computed:

$$M_{i,j} = \frac{\sum_{n=1}^{N} C_i(n) \times C_j(n)}{\sqrt{\sum_{n=1}^{N} C_i(n)^2 \times \sum_{n=1}^{N} C_j(n)^2}} \tag{4.10}$$

where (i, j) corresponds to each entry in M. Further, C_i and C_j are the (i, j) columns of the Casorati matrix, respectively and N denotes the number of rows in the Casorati matrix *(Nayak, 2019)*. The correlation matrix quantifies the similarity of the pixels in the 3D kernel. Highly dissimilar pixels corresponding to noise yielded a low correlation value *(~ 0)*, while those associated with flow pixels yielded relatively higher values *(~ 0.4)* *(Nayak, 2019)*. This information is used in synthesizing a purely noise image from which inherent noise bias can be deduced *(Nayak, 2019)*. The mean of the estimated local correlation matrices M, which inherently ranged between *0-1*, constituted the noise and flow *(Nayak, 2019)*. Specifically, the pixel intensity at location *{x, z}* in the STC image is estimated by computing the values associated with the flow pixels were relatively higher

compared to noise. Accordingly, they could be separated based on grey-scale thresholding of the STC image *(figure 4.15) (Nayak, 2019)*.

Since noise is expected to be statistically uniform across the columns and frames of the Doppler ensemble, the identified blood flow pixels are replaced by noise pixels randomly selected from the lateral neighborhood, across multiple frames of the CFDE *(Nayak, 2019)*. Moreover, since the amplification due to TGC varies gradually across depth, the replacement noise pixels could be selected from over a range of depth (rows), without affecting the performance of the technique *(Nayak, 2019)*.

4.5.2.2 Estimation of the Low-Rank Noise Field

The background noise field is characterized by a smooth depth-increasing signal that is replaced across all columns of the image, consistent with the notion that TGC is applied uniformly across all receive channels *(Nayak, 2019)*. Accordingly, to derive the noise field that is repetitive across all columns of the synthetic noise image, a SVD based low-rank matrix approximation is performed *(Nayak, 2019)*. Specifically, the noise field is reconstructed using the lowest singular order component that also corresponded to the highest SV. Since the low-rank noise field is estimated from a single synthetic noise field, it is then smoothed using a 2D least square method that fitted a 2D plane in locally overlapping kernels across the depth of the image *(Nayak, 2019)*.

The background-suppressed PD image is computed by normalizing the original PD image with the estimated noise field *(Nayak, 2019)*. This corresponds to subtraction of the estimated noise field from the original PD image in the log scale that is used for image display. Accordingly, total suppression of noise should theoretically lead to a 0 dB background signal *(Nayak, 2019)*.

An example is provided in *figure 4.15* to outline different steps involved in estimation of the synthetic noise image from the Doppler ensemble.
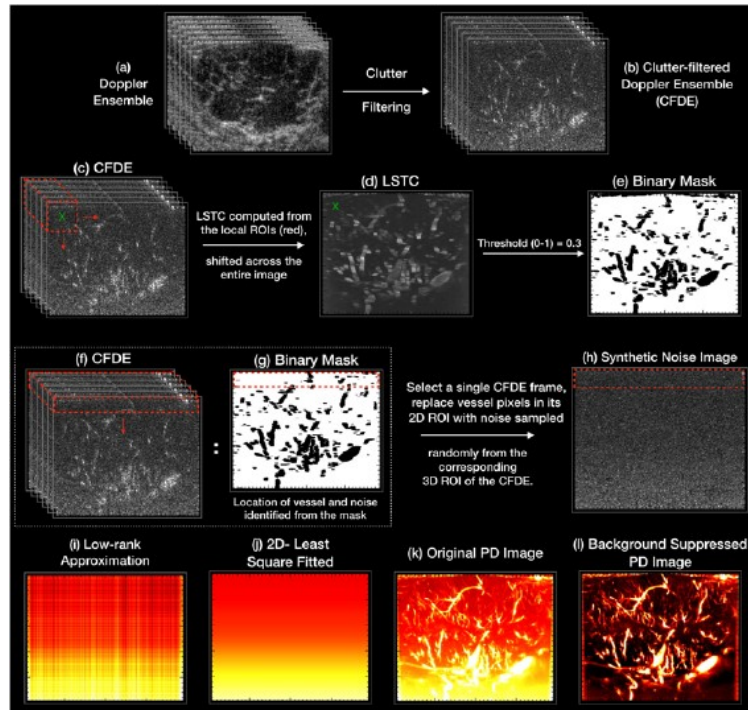
Figure 4.15 (a) and (b) display the acquired Doppler ensemble, and the corresponding clutter-filtered Doppler ensemble (CFDE), respectively. The corresponding LSTC image (d) is computed from the CFDE (c) by estimating spatiotemporal correlation in local 3D kernels (red) as defined in equation (3). (e) and (g) displays the binary mask computed by greyscale thresholding of the LSTC image, which is inherently normalized between 0–1. The black and white regions correspond to the location of the flow and noise pixels, respectively. The synthetic noise image (h) is generated from a single clutter filtered image, by replacing its vessel pixels by randomly selected noise from its local 3D neighborhood in the corresponding CFDE (f). (i) displays the low-rank approximation of the synthetic noise image (h), which is subsequently smoothened using a 2D least-square based plane-fit algorithm to generate the final noise field (j). The final PD image (l) is obtained by suppressing the estimated noise field (j) in the original PD image (k). *(Nayak, 2019).*

Materials and Methods

5.1 Data Acquisition

The ultrasound in-phase and quadrature (IQ) data for the phantom and *in vivo* experiments were acquired using an Alpinion E-Cube 12R ultrasound scanner (Alpinion Medical System Co., Seoul, South Korea), equipped with a L12-3H linear probe. The scanner transmitted and received using 128 and 64 elements, respectively. The plane wave IQ data were acquired using 7 compounding angles, with a maximum angle of 3° and an incremental step size of 1° *(Montaldo, 2009; Denarie, 2013; Nayak, 2017)* at a transmit frequency of 11.5 MHz. Specifically, each B-mode image was computed by transmitting 7 angular plane waves (-3°, -2°, -1°, 0°, 1°, 2°, 3°), and the corresponding received signals were computed to form a single image. This process was repeated sequentially to acquire 1848 compounded images in 3 seconds, for an image depth of 35 mm. The imaging pulse repetition frequency was 9624 Hz. However, the final imaging frame rate decreased to 616 Hz because of (i) seven-angle plane wave compounding, and (ii) the scanner's requirement for two receive events (with 64 elements in each) to create a single image. Accordingly, the frame rate was 8624 Hz/7/2 = 616 Hz. The received radiofrequency signal was sampled at 40 MHz. The beamformed images obtained from the E-Cube 12R has dimensions of 960×192 pixels (depth × width). The axial and lateral lengths of each pixel were 38.5 and 200 μm, respectively. The speed of sound was assumed to be 1540 m/s for the calculation of beamforming delays.

5.2 Phantom Study

The goal of the phantom study was to evaluate the feasibility of using non-redundant ensembles and customized frame intervals to improve the tracking of small-inter frame displacements, and to compare the performance of the optimized algorithm *(figure 5.1(e))* to that of the previous one *(figure 5.1(d)),* in a controlled environment. The experiments were conducted using a homogeneous tissue-mimicking custom LE series phantom from Gammex (Middleton, WI, USA) that had an attenuation coefficient of 0.5 dB/cm/MHz *(McFarlin, 2015)*. The phantom data were acquired using the data acquisition described in the previous section. To acquire data without any motion, the linear array

probe was clamped to a rigid stand. With these data, instances of rigid body translational motion were realized in MATLAB (The MathWorks, Natick, MA, USA) by shifting the rows (axially) of Doppler frames by a total of 5 and 10 pixels or the columns (laterally) of Doppler frames by a total of 5, 15 and 30 pixels for ensembles of different size (50, 100, 200, 400, 800 and 1600 frames). Moreover, instances of periodic motion were realized as a combination of lateral displacements of 5 or 10 pixels for ensembles of 1800 frames. In particular, the first instance of periodic motion was realized by laterally shifting 9 groups of 200 Doppler frames by 0, 5, 0, -5, 0, 5, 0, -5, 0 pixels, respectively; while the other one by laterally shifting 9 groups of 200 Doppler frames by 0, 10, 0, -10, 0, 10, 0, -10, 0 pixels, respectively. The subpixel displacements between consecutive frames were achieved by using a spline-based subpixel interpolation *(Huntzicker, 2014; Konofagou, 1998; Parker, 1983).* Motion was introduced in post-processing specifically to prevent any potential out-of-plane motion or speckle decorrelation. Therefore, in the absence of blood activity, out-of-plane motion and speckle decorrelation, any loss in covariance of the spatiotemporal data could be addressed to in-plane translational motion.
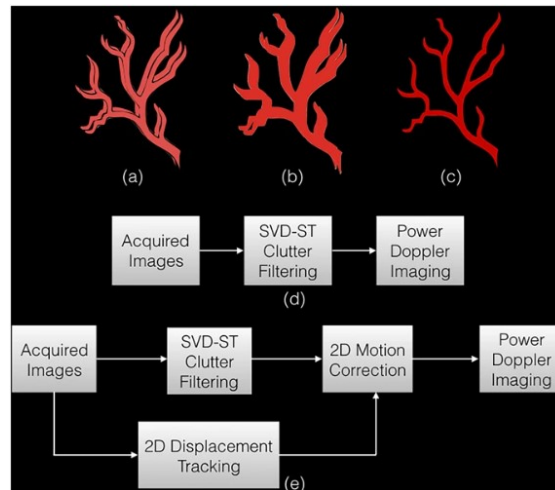
Figure 5.1 (**a**) displays the clutter filtered blood flow signal in two example Doppler frames, spatially mis-registered due to motion. On estimating the power Doppler image, the final image is blurred with appearance of shadow vessels. (**c**) displays the final image expected upon motion correction, where the Doppler signals coherently integrate to produce a stronger signal with reduced motion artifacts. Specifically, (**b**) and (**c**) are obtained using the approach outlined in (**d**) and (**e**), respectively. *(Nayak, 2018)*

5.3 In vivo study

The in vivo study was conducted to evaluate the feasibility of using corrected ultrasound data to improve the visualization of small vessel flow in thyroid, using a clinical ultrasound scanner. The ultrasound data was obtained from two patients with suspicious thyroid nodule, recommended for ultrasound-guided FNA biopsy. The study was performed in accordance with the relevant guidelines and regulations approved by the Mayo Clinic institutional review board and a written approved, informed consent was obtained from the patient prior to their participation. The ultrasound data was acquired by an experienced sonographer, across the longitudinal cross-section of the right thyroid gland, prior to the scheduled biopsy of the nodule. Further, the patient was asked to hold the breath for the 3 seconds duration of the scan to minimize any motion due to breathing.

5.4 Image Processing and Analysis

The proceeding subsections describe the method used for phantom and in vivo processing and analysis. The previous approach follows exactly the same steps but the generation of the non-redundant ensemble and the computation of customized frame intervals.

Computation of the Correlation Matrix before Motion Correction

Once the ultrasound Doppler ensemble was generated, a ROI of dimensions $m \times n \times t$ pixels in axial, lateral and temporal direction respectively, was selected. The pixels within the 3D ROI were arranged in the in the space-time Casorati form of dimension $s \times t$, where $s = m \times n$. The normalized correlation matrix, labelled MM Pre, of dimension $t \times t$ was computed. The correlation matrix quantifies the similarity of frames within the 3D ROI.

Generation of the Non-redundant Ensemble

The information content of MM Pre was used to generate a non-redundant ensemble; specifically, couples of frames displaying a CC above a certain threshold (th) (lateral motion simulations, *th=0.9*; axial motion simulations, *th=0.7*; periodic motion simulations, *th=0.95*), were rejected. The new non-redundant ensemble was then rearranged in the

Casorati form and a new normalized correlation matrix, labelled MM No Red, was computed.

Computation of the Optimal Skip Size

An optimal skip size was computed by searching for dissimilarities among frames. Specifically, for each frame of the non-redundant ensemble, a plot of the correlation values associated to all the other frames was obtained. The first point of zero-line crossing was found and acknowledged as the optimal skip size. The vector containing the optimal index for each frame in the non-redundant ensemble was fed to the tracking algorithm.

Displacement tracking

The axial and lateral displacements were estimated using a 2D-NCC based echo tracking algorithm. The displacements estimates associated to the in vivo ultrasound data were estimated prior to clutter filtering, although motion correction was applied on clutter-filtered data. The ultrasound images were interpolated in the axial and lateral directions by factors of 3 and 10, respectively *(Huntzicker, 2014; Konofagou, 1998; Parker, 1983)*. The images were interpolated to increase the spatial density of the correlation functions. This is particular important for estimating lateral motion, because ultrasound provides no phase information in the direction perpendicular to beam propagation *(Konofagou, 1998)*. Subsequently, the ultrasound images were tracked using a 2D kernel (0.2×0.8 mm), which overlapped by 90% in both coordinates. The Cartesian displacement estimates between each consecutive pair of images were calculate as described in *(Zahiri-Azar, 2006)*, using peak of cross-correlation. Specifically, the 2D kernel based sliding reference window obtained from the first ultrasound image was cross-correlated with the corresponding displaced location of the reference window in the subsequent image. In addition, a 2D spline interpolation was used to determine the location of the peak cross-correlation coefficient to subpixel accuracy.

SVD based Spatio-temporal Clutter Filtering

The original ultrasound data was clutter filtering using the SVD of the spatiotemporal Casorati matrix.

$$S_{blood} = S(x, z, t) - \sum_{r=1}^{r=th} U_r \lambda_r V_r^* \tag{5.1}$$

where the matrices S and S_{blood} represent pre- and post- clutter filtered Doppler ensemble. The matrices U, V consist of left and right singular orthonormal vectors, respectively. The corresponding singular values and their order are denoted by λ_r and r, respectively, and * represents conjugate transpose. A global SV threshold was chosen to separate tissue clutter from blood signal, based on the decay of the double derivative of the SV orders (i.e. when the double derivative approached zero).

Motion Correction of the Non-redundant Ensemble

The estimated axial and lateral displacement maps were transformed from Eulerian to Lagrangian coordinates to correspond with the first frame of the Doppler ensemble. Motion correction of the non-redundant Doppler ensemble was performed to re-register each ultrasound frame with that of the first frame, by globally shifting the rows and columns by the estimated displacements. The correlation matrix, labelled MM No Red Moco, was computed and the associated mean correlation coefficient was used as a performance index to asses for motion correction on the non-redundant ensemble.

Motion Correction of the Full Ensemble

The original full Doppler ensemble was then corrected by clustering twin frames together.

Computation of MM post

The correlation matrix, labelled MM post, was compute to assess the efficacy of the motion correction performance.

Power Doppler Imaging

The final power Doppler signal was computed from the motion corrected data:

$$PD(x, z) = \sum_{t=1}^{N_t} |S_{blood}(x, z, t)|^2 \tag{5.2}$$

where N_t indicates the ensemble length.

Noise Bias Suppression

The dimension of the local 3D kernel *(m, n, t)* were assigned as (3,3,30), respectively. The grey scale threshold was empirically chosen as 0.30; pixels with higher or lower STC were

identified as blood vessels or noise, respectively. The local noise neighborhood was limited to (30, 192, 30) pixels, across rows, columns and frames, respectively.

The axial and lateral widths of the kernels were 100 and 192 pixels, respectively. The kernels overlapped by one pixel, and they were constrained to have zero-slope in the lateral direction.

Results

6.1 Phantom Results

6.1.1 Instance of Axial Motion

The proceeding subsection includes results obtained for a simulated motion of 5.1948 pixels or 0.2 mm in the axial direction.

Figure 6.1 (a-f) illustrates the motion matrices before motion correction, MM Pre, for ensembles of 50, 100, 200, 400, 800 and 1600 Doppler frames. The value of the mean correlation coefficient increased along with the size of the Doppler ensemble. Larger ensembles resulted in smaller inter-frame displacements, which, in turn, guaranteed slightly higher level of similarity between each couple of frames, leading thus to a slightly higher mean correlation coefficient.
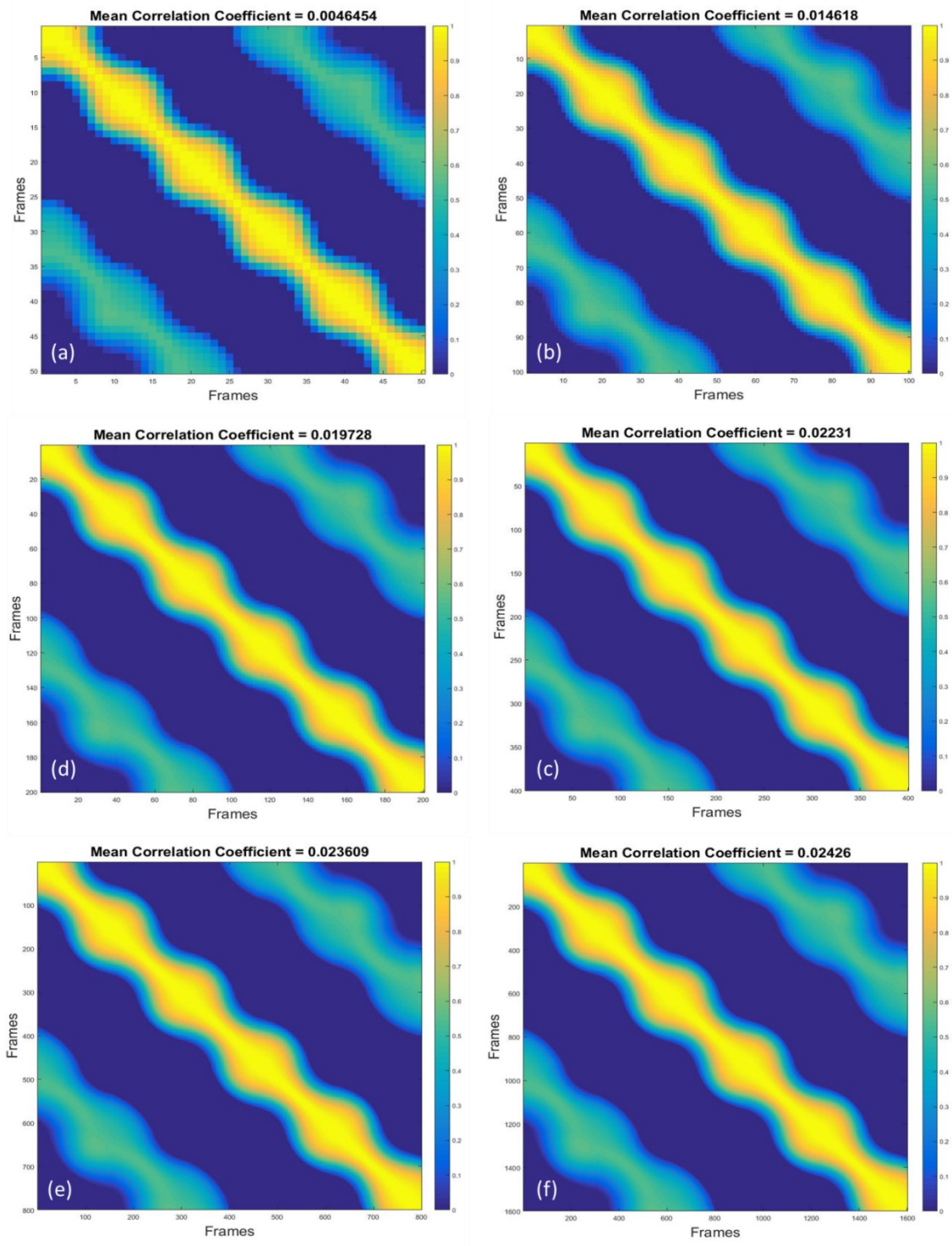
Figure 6.1 MM Pre and associated mean correlation coefficients for Doppler ensembles of: (a) 50 frames, (b) 100 frames, (c) 200 frames, (d) 400 frames, (e) 800 frames and (f) 1600 frames.

In *figure 6.2 (a-f)* are the Motion matrices, MM No Red, and relative mean correlation coefficients computed on the new non-redundant ensembles of 11, 12, 13, 13, 13 and 13 frames, respectively.
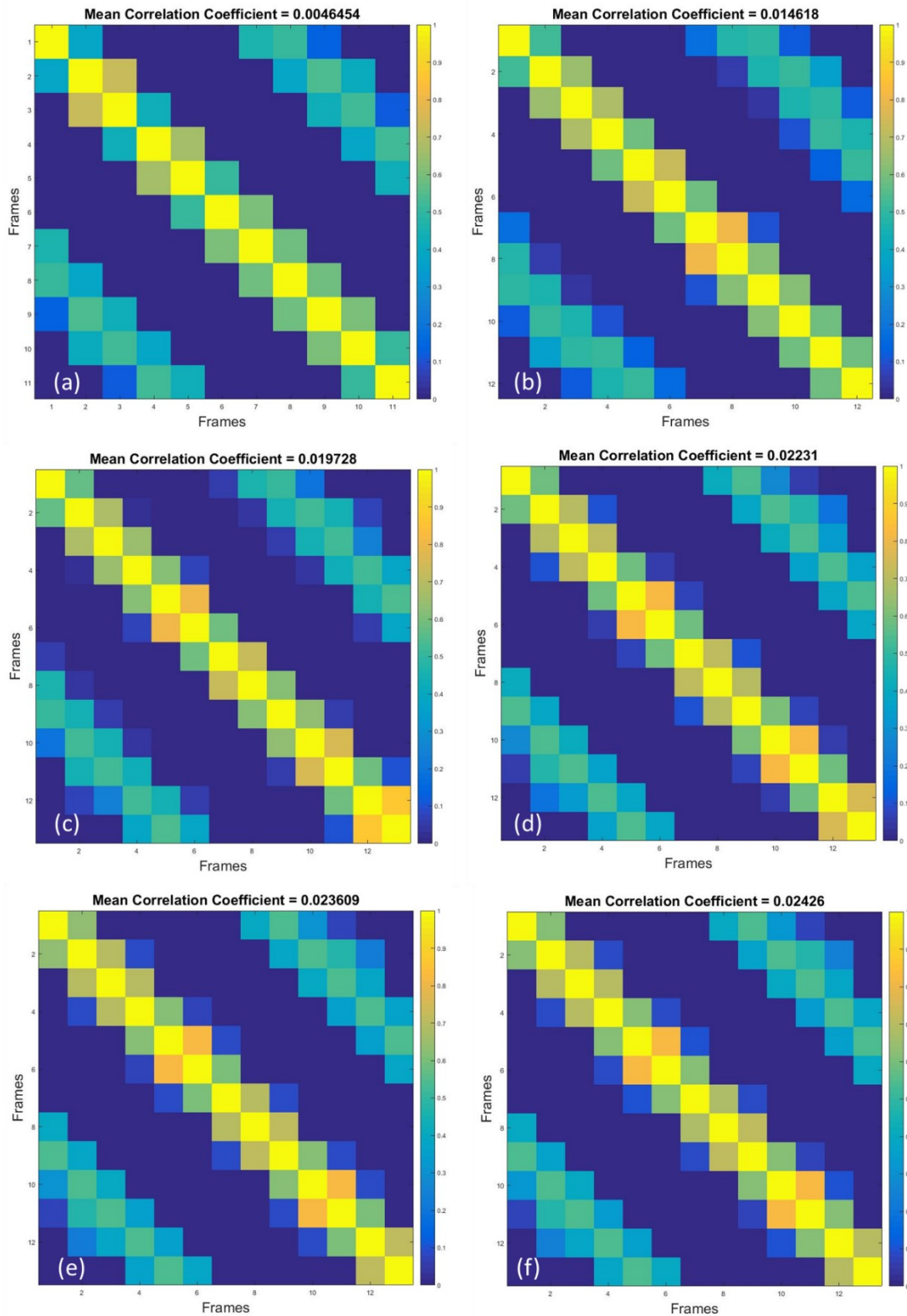
Figure 6.2 MM No Red and relative mean correlation coefficients for the new non-redundant ensembles of: (a) 11 frames, (b) 12 frames, (c) 13 frames, (d) 13 frames, (e) 13 frames and (f) 13 frames.

In *figure 6.3* are the values of the optimal skip size for each frame of the non-redundant ensembles of: *(a)* 11 frames, *(b)* 12 frames, *(c)* 13 frames, *(d)* 13 frames, *(e)* 13 frames and *(f)* 13 frames. As noticeable, the optimal index was almost always equal to 1. This indicated that the frames of the Doppler ensembles were strongly dissimilar. Remind that, in simulations of axial displacement, while generating the non-redundant ensembles, the threshold was set to 0.7, meaning that also frames medium level of similarity were rejected.
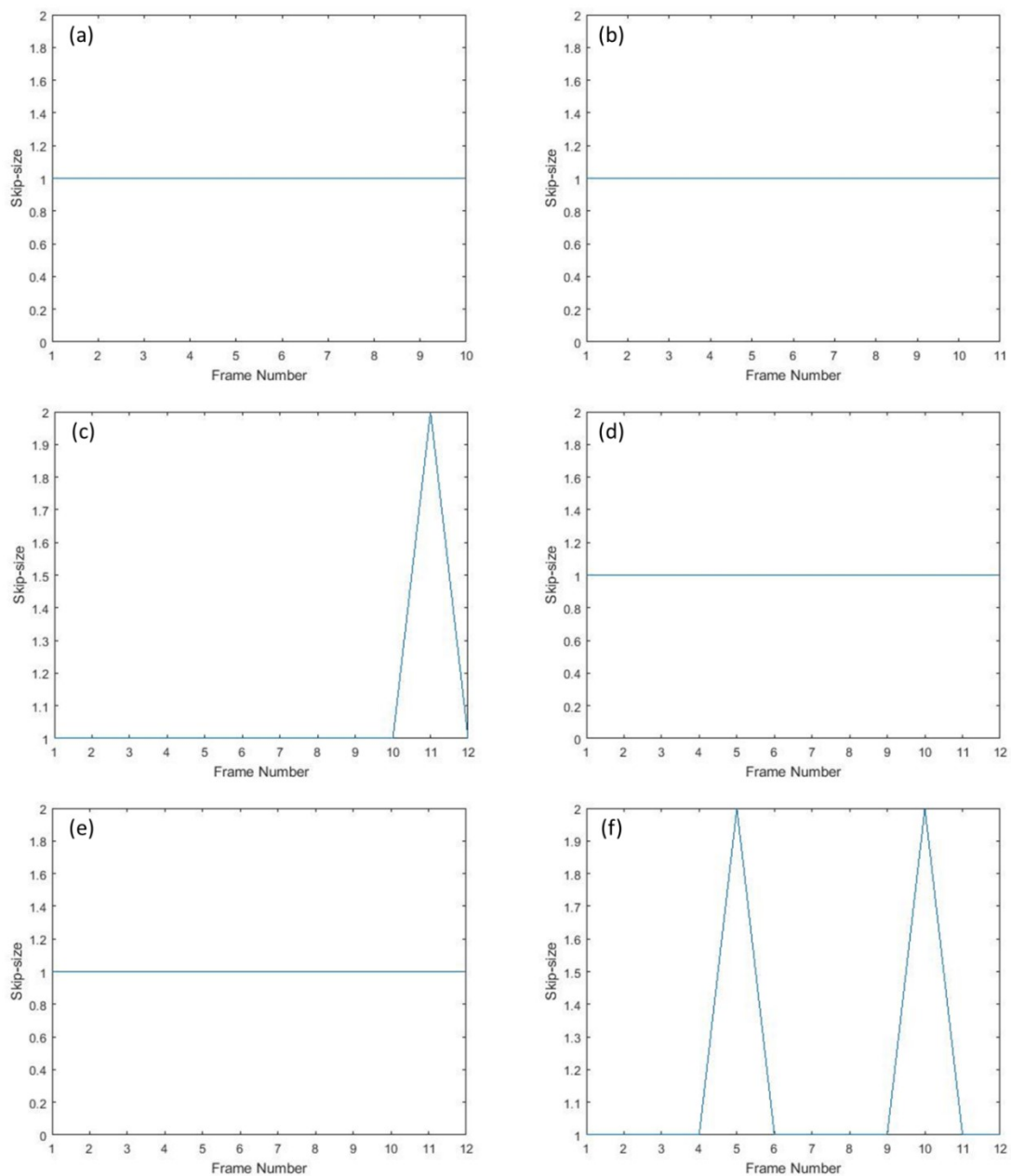
Figure 6.3 Customized frame intervals for Doppler ensembles of: (a) 11 frames, (b) 12 frames, (c) 13 frames, (d) 13 frames, (e) 13 frames and (f) 13 frames.

Figure 6.4 shows the displacement estimates in mm for a Doppler ensemble of 50 frames. The upper plots (a, c) display the frame-to-frame displacements whereas the lower plots (b, d) show the cumulative displacements. (a, b) were obtained applying the previous approach whereas (c, d) were obtained applying the new approach. Using the former algorithm, the final estimate was 0.1078 mm. Conversely, the non-redundant Doppler ensemble and the optimal skip size provided a final estimate of 0.1786 mm.
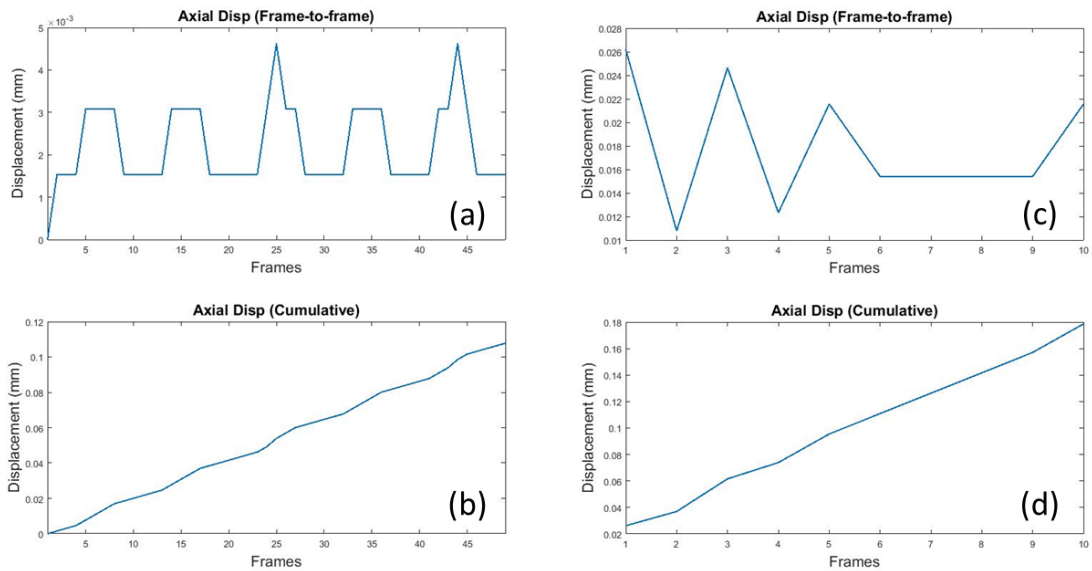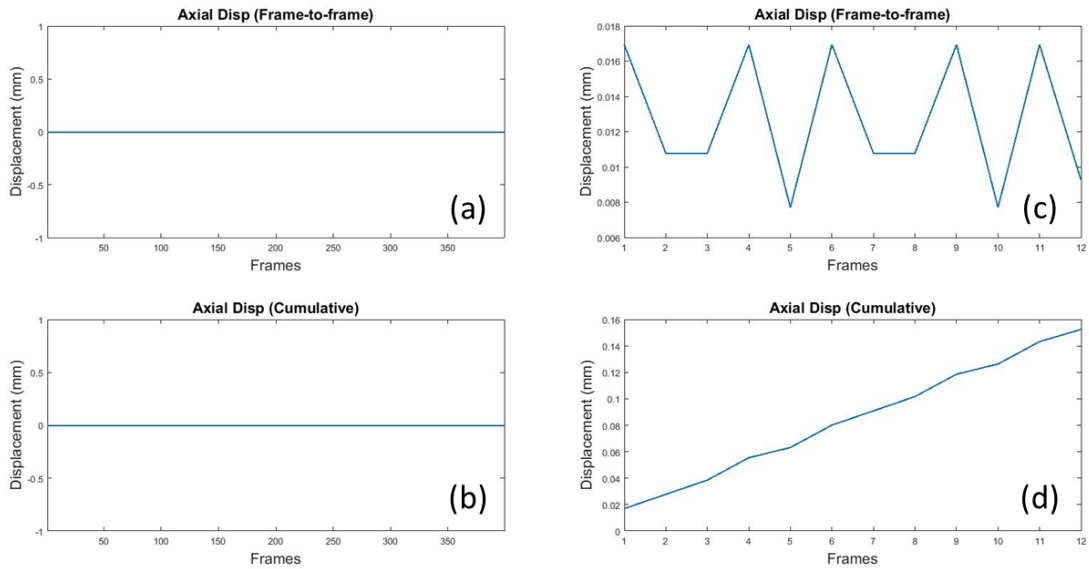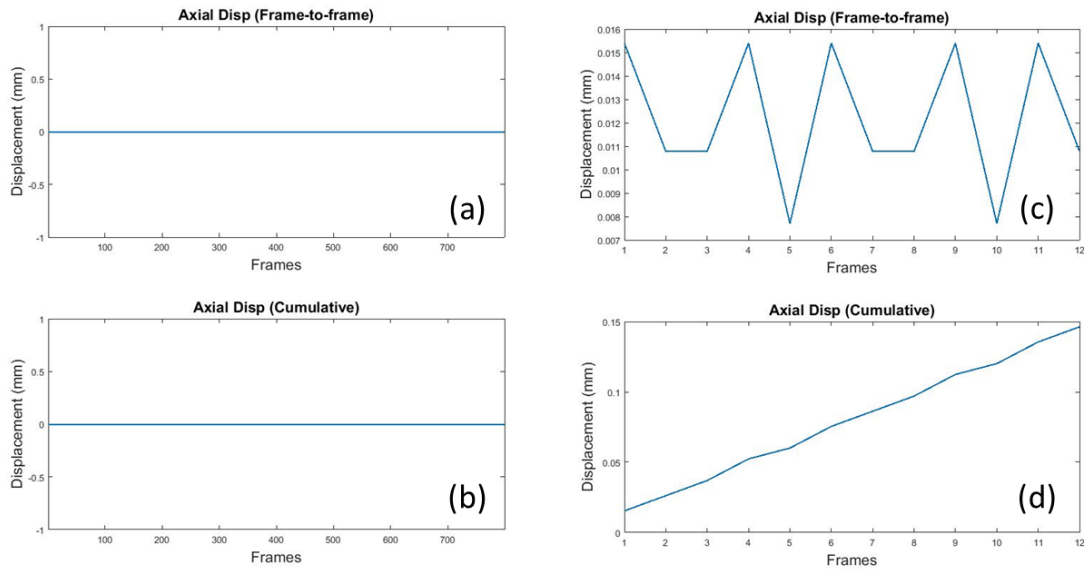

Figure 6.4 Displacement estimates. (a, c) frame-to-frame displacement; (b, d) cumulative displacement; (a, b) full ensemble, skip size equal to 1; (c, d) non-redundant ensemble, customized frame intervals.

Figure 6.5 shows the displacement estimates in mm for a Doppler ensemble of 100 frames. The upper plots (a, c) display the frame-to-frame displacements whereas the lower plots (b, d) the cumulative displacements. (a, b) were obtained applying the previous approach whereas (c, d) were obtained applying the new approach. The former algorithm gave a final estimate of 0.08932 mm. Conversely, the non-redundant ensemble and the optimal skip size provided a final estimate of 0.1571 mm.
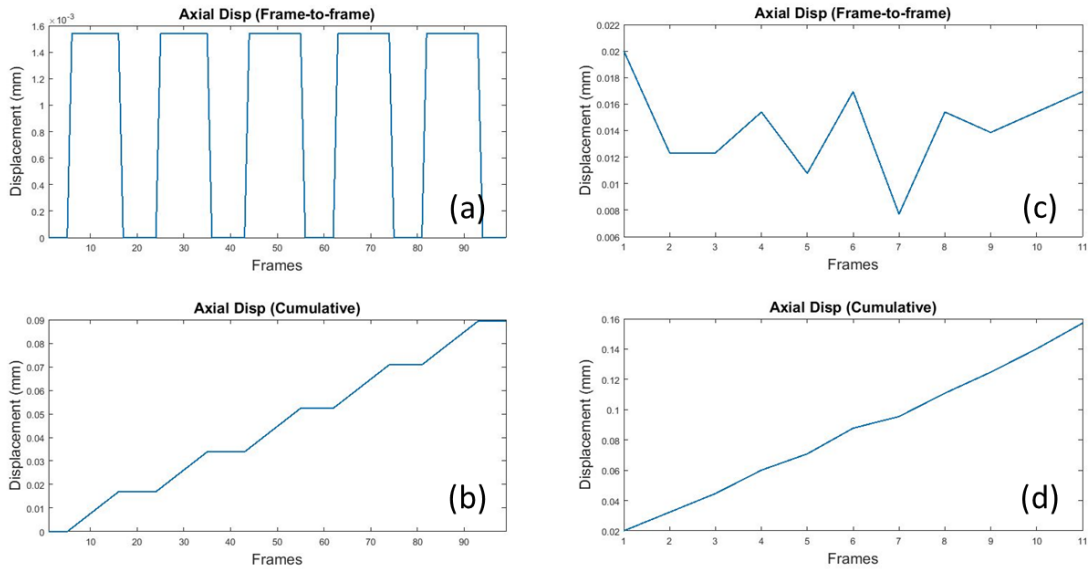
Figure 6.5 Displacement estimates. (a, c) frame-to-frame displacement; (b, d) cumulative displacement; (a, b) full ensemble, skip size equal to 1; (c, d) non-redundant ensemble, customized frame intervals.

Figure 6.6 shows the displacement estimates in mm for a Doppler ensemble of 200 frames. The upper plots *(a, c)* display the frame-to-frame displacements whereas the lower plots (b, d) the cumulative displacements. *(a, b)* were obtained applying the previous approach whereas *(c, d)* were obtained applying the new approach. Using the former algorithm, the final estimate was 0.06006 mm. Conversely, the non-redundant ensemble and the optimal skip size provided a final estimate of 0.1502 mm.
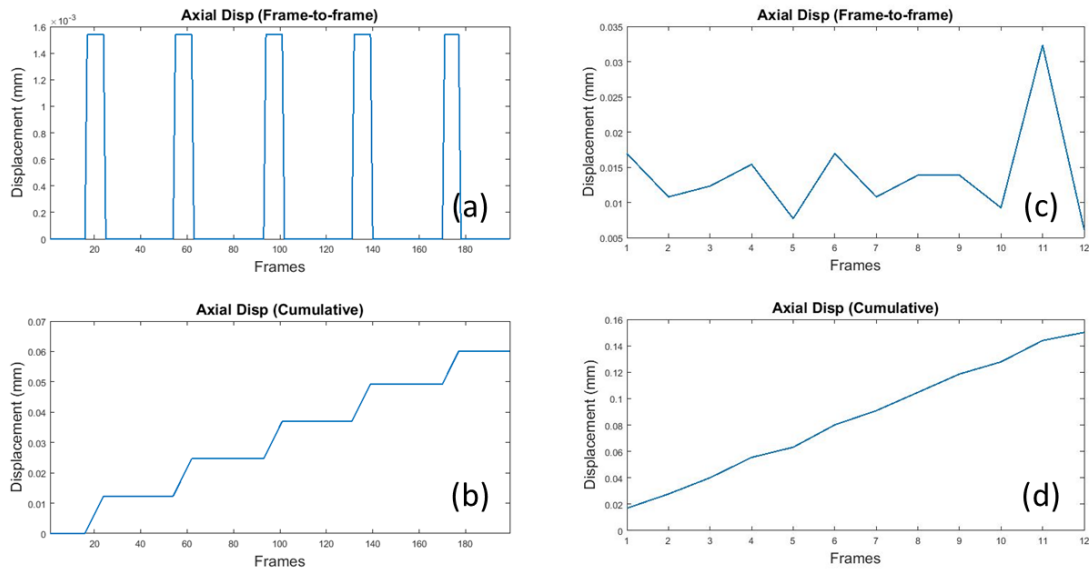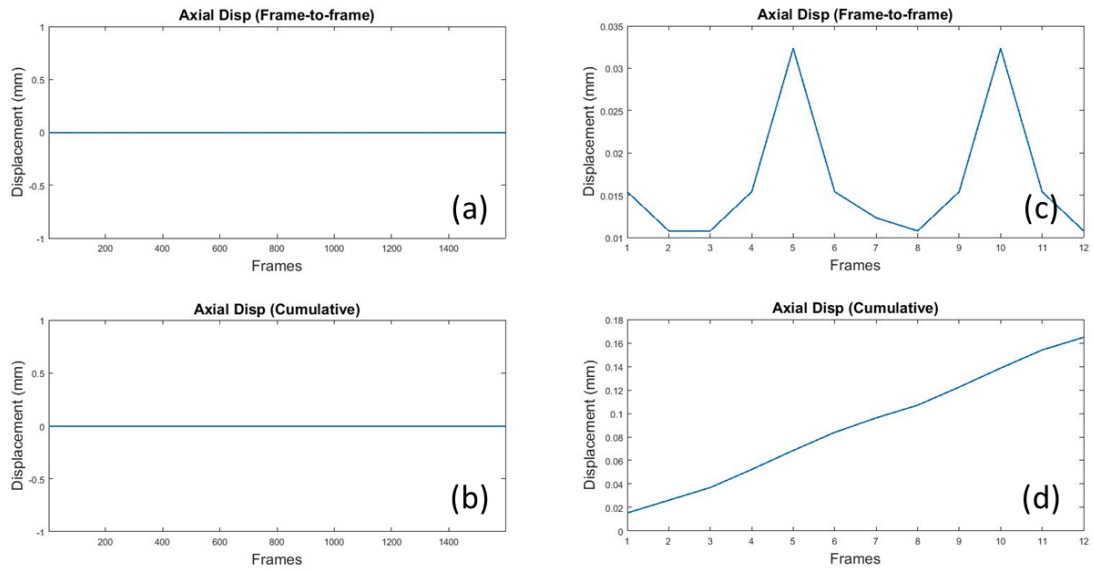
Figure 6.6 Displacement estimates. (a, c) frame-to-frame displacement; (b, d) cumulative displacement; (a, b) full ensemble, skip size equal to 1; (c, d) non-redundant ensemble, customized frame intervals.

Figure 6.7 shows the displacement estimates in mm for a Doppler ensemble of 400 frames. The upper plots *(a, c)* display the frame-to-frame displacements whereas the lower plots *(b, d)* the cumulative displacements. *(a, b)* were obtained applying the previous approach whereas *(c, d)* were obtained applying the new approach. Using the former algorithm, the final estimate was 0.0 mm. Conversely, the non-redundant ensemble and the optimal skip size provided a final estimate of 0.1525 mm.

Figure 6.7 Displacement estimates. (a, c) frame-to-frame displacement; (b, d) cumulative displacement; (a, b) full ensemble, skip size equal to 1; (c, d) non-redundant ensemble, customized frame intervals.

Figure 6.8 shows the displacement estimates in mm for a Doppler ensemble of 800 frames. The upper plots *(a, c)* display the frame-to-frame displacements whereas the lower plots *(b, d)* the cumulative displacements. *(a, b)* were obtained applying the previous approach whereas *(c, d)* were obtained applying the new approach. Using the former algorithm, the final estimate was 0.0 mm. Conversely, the non-redundant ensemble and the optimal skip size provided a final estimate of 0.1463 mm.

Figure 6.8 Displacement estimates. (a, c) frame-to-frame displacement; (b, d) cumulative displacement; (a, b) full ensemble, skip size equal to 1; (c, d) non-redundant ensemble, customized frame intervals.

Figure 6.9 shows the displacement estimates in mm for a Doppler ensemble of 1600 frames. The upper plots *(a, c)* display the frame-to-frame displacements whereas the lower plots *(b, d)* the cumulative displacements. *(a, b)* were obtained applying the previous approach whereas *(c, d)* were obtained applying the new approach. Using the former algorithm, the final estimate was 0.0 mm. Conversely, the non-redundant ensemble and the optimal skip size provided a final estimate of 0.1648 mm.

Figure 6.9 Displacement estimates. (a, c) frame-to-frame displacement; (b, d) cumulative displacement; (a, b) full ensemble, skip size equal to 1; (c, d) non-redundant ensemble, customized frame intervals.

In *figure 6.10 (a, c, e, g, i, k)* are the motion matrices computed after motion correction of the non-redundant ensembles, MM No Red Moco. *(b, d, f, h, j, l)* are the motion matrices computed after motion correction, MM Post, of the full Doppler ensembles of 50, 100, 200, 400, 800 and 1600 frames, respectively.

NO RED MOCO - Mean CC = 0.91877

MM POST - Mean CC = 0.88878

NO RED MOCO - Mean CC = 0.79069

MM POST - Mean CC = 0.69644

NO RED MOCO - Mean CC = 0.72143

MM POST - Mean CC = 0.6503

NO RED MOCO - Mean CC = 0.75779

MM POST - Mean CC = 0.6762

NO RED MOCO - Mean CC = 0.69154

MM POST - Mean CC = 0.62372

NO RED MOCO - Mean CC = 0.89768

MM POST - Mean CC = 0.8247
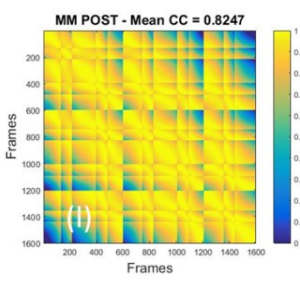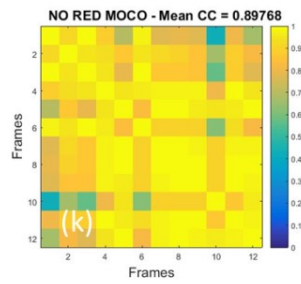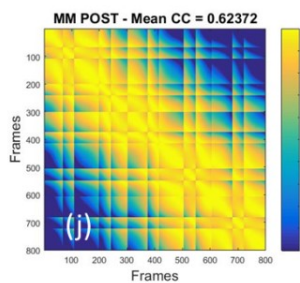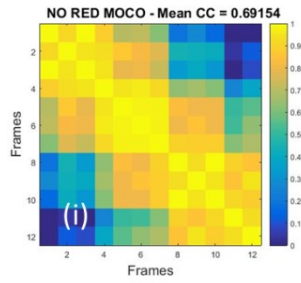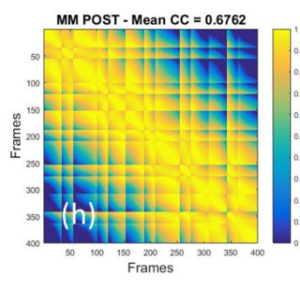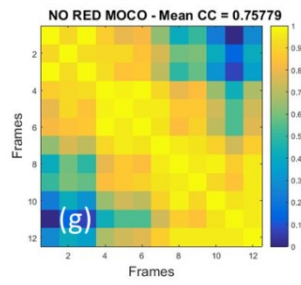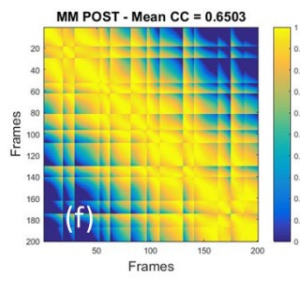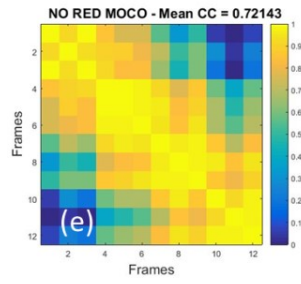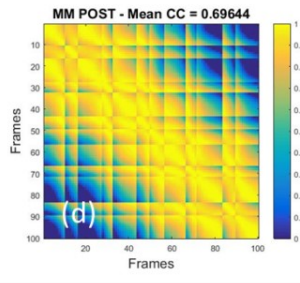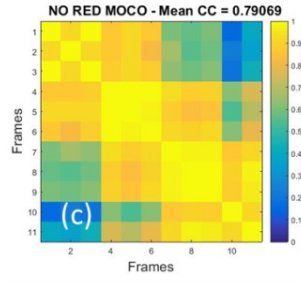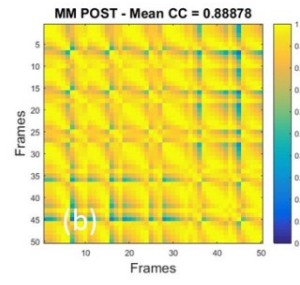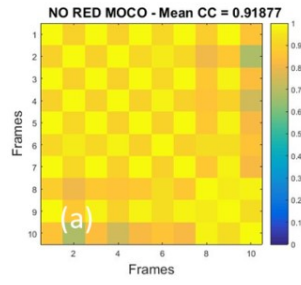
Figure 6.10 Motion matrices and associated mean correlation coefficients computed after motion correction of the non-redundant, MM No Red Moco, (a, c, e, g, i, k) and full, MM Post, (b, d, f, h, j, l) Doppler ensembles of 50, 100, 200, 400, 800 and 1600 frames.

Figure 6.11 (a-f) illustrates the motion matrices, for different ensemble length, computed after motion correction using the former algorithm. These motion matrices are referred to as MM Post*. The values of the mean correlation coefficient for Doppler ensembles of 400, 800 and 1600 frames were unaltered compared to those obtained before motion correction because of null displacement estimation. Slightly differences were addressed to noise related issues.
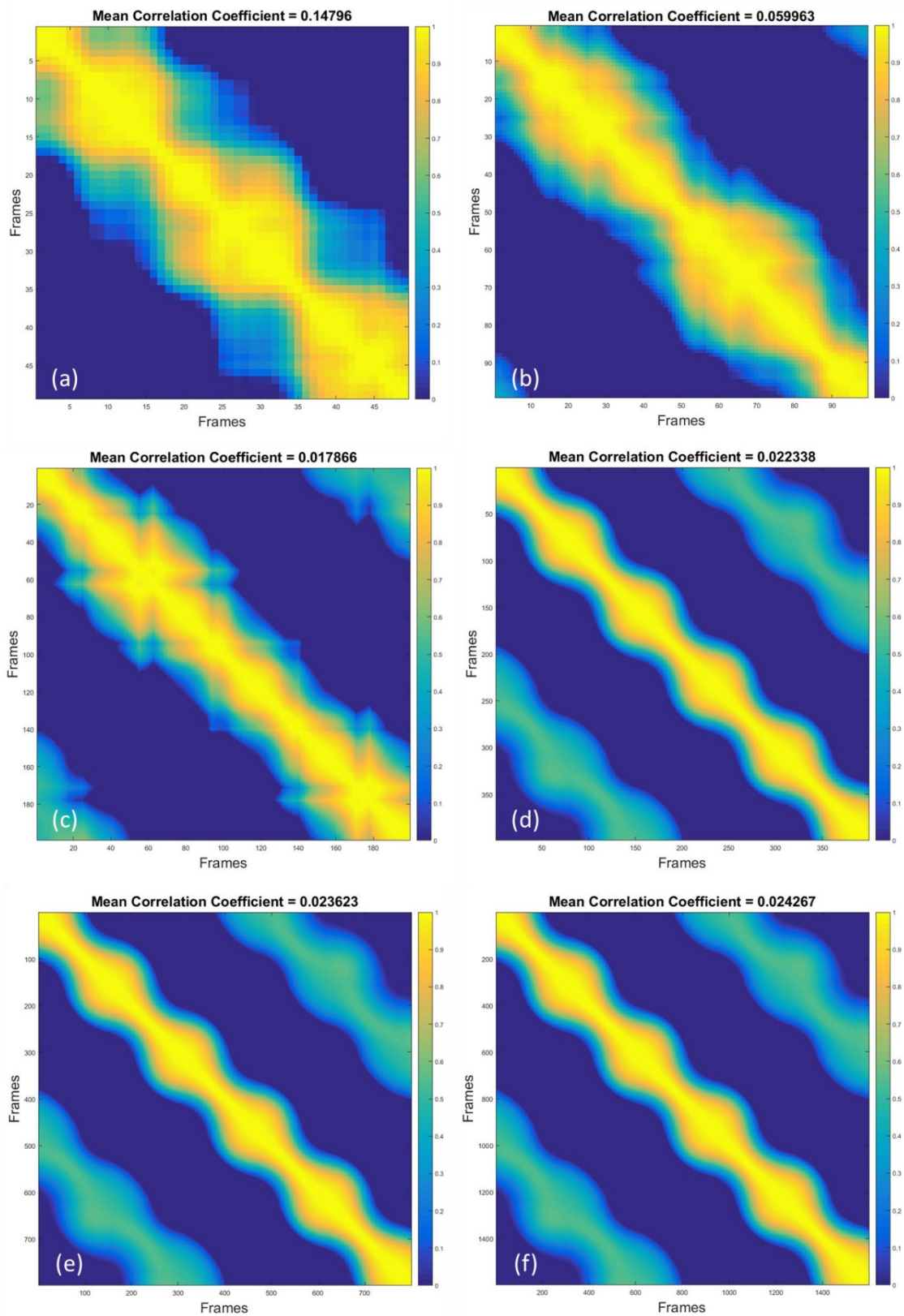
Figure 6.11 MM Post* and associated mean correlation coefficients after performed motion correction using the former algorithm, for Doppler ensembles of dimension: (a)

50 frames, (b) 100 frames, (c) 200 frames, (d) 400 frames, (e) 800 frames and (f) 1600 frames.

Table 6.1 synthetizes the values of the mean correlation coefficient of MM pre, MM No Red, MM No Red Moco, MM Post and MM Post* for all the Doppler ensembles. As noticeable, MM Post showed higher mean correlation coefficients than MM Post* for all the ensemble sizes.

Table 6.1 Mean correlation coefficients associated to Doppler ensembles of different size. Numbers between brackets indicates the number of frames in the non-redundant ensembles.

Ensemble Size	Mean Correlation Coefficients				
	MM Pre	MM No Red	MM No Red Moco	MM Post	MM Post*
50 (11)	0.0046454	0.0046454	0.91877	0.88878	0.14796
100 (12)	0.014618	0.014518	0.79069	0.69644	0.059963
200 (13)	0.019728	0.019728	0.72143	0.6503	0.017866
400 (13)	0.02231	0.02231	0.75779	0.6762	0.022338
800 (13)	0.023609	0.023609	0.69154	0.62372	0.023623
1600 (13)	0.02426	0.02426	0.89768	0.8247	0.024267

6.1.2 Instance of Lateral Motion

The proceeding subsection includes results obtained for a simulated motion of 5 pixels or 1 mm in the lateral direction.

In *figure 6.12 (a-f)* are the motion matrices before motion correction, MM Pre, for ensembles of 50, 100, 200, 400, 800 and 1600 frames.
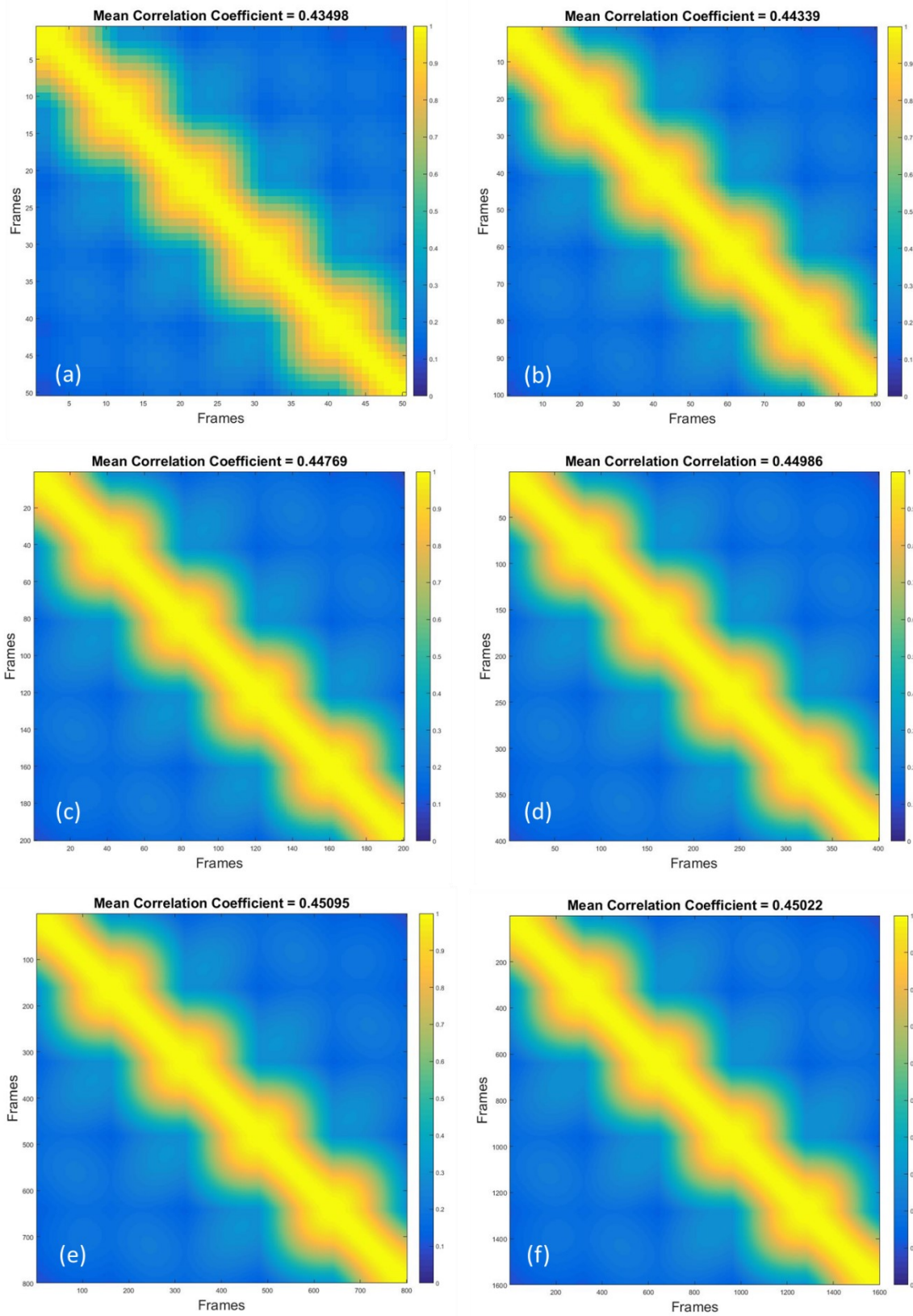
Figure 6.12 MM Pre and associated mean correlation coefficients for Doppler ensembles of: (a) 50 frames, (b) 100 frames, (c) 200 frames, (d) 400 frames, (e) 800 frames and (f) 1600 frames.

In *figure 6.13 (a-f)* are the Motion matrices, MM No Red, and relative mean correlation coefficients computed on the new non-redundant ensembles of 11, 12, 13, 13, 13 and 13 frames, respectively.
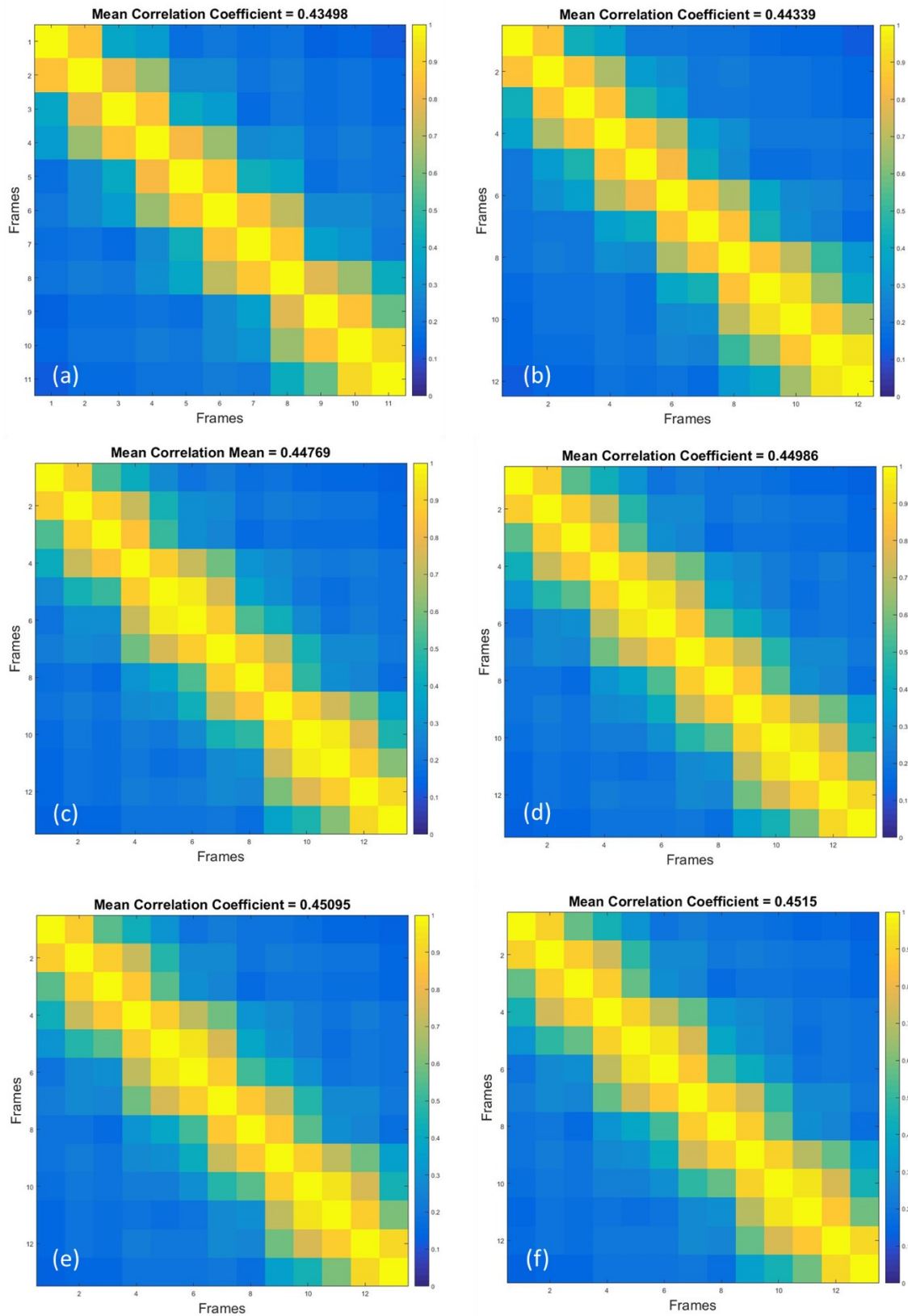
Figure 6.13 MM No Red and relative mean correlation coefficients for the new non-redundant ensembles of: (a) 11 frames, (b) 12 frames, (c) 13 frames, (d) 13 frames, (e) 13 frames and (f) 13 frames.

Figure 6.14 displays the optimal skip size associated to each frame of the non-redundant ensembles of: *(a)* 11 frames, *(b)* 12 frames, *(c)* 13 frames, *(d)* 13 frames, *(e)* 13 frames and *(f)* 13 frames. The optimal skip size vector was not uniform at all, suggesting a medium-high level of similarity throughout the ensembles. Remind that, in simulations of lateral displacement, while generating the non-redundant ensembles, the threshold was set to 0.9, meaning that only frames with a strongly level of similarity were rejected.
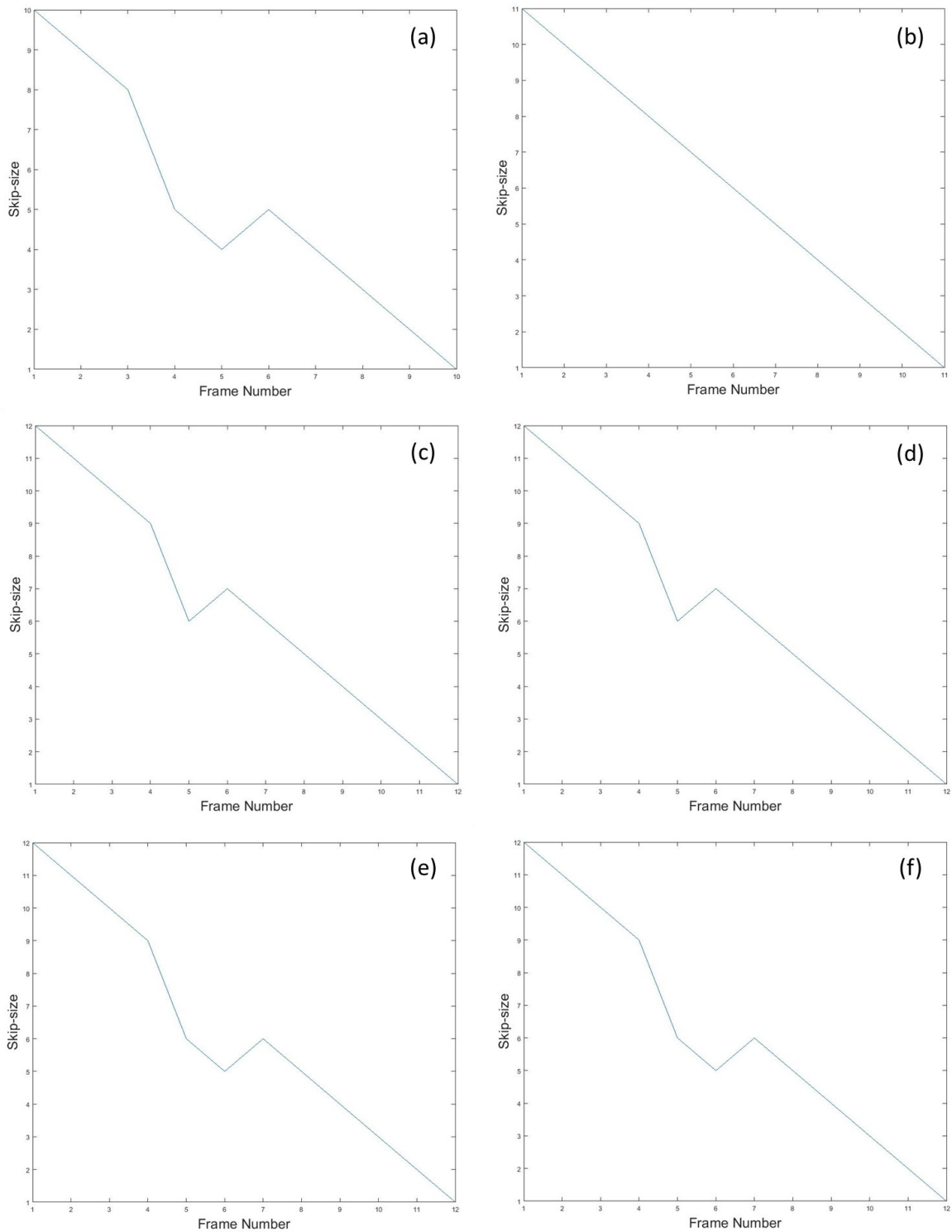
Figure 6.14 Customized frame intervals for Doppler ensembles of: (a) 11 frames, (b) 12 frames, (c) 13 frames, (d) 13 frames, (e) 13 frames and (f) 13 frames.

Figure 6.15 shows the displacement estimates for a Doppler ensemble of 50 frames. The upper plots *(a, c)* display the frame-to-frame displacement. Estimates in *(a)* are in mm,

whereas, those in *(c)* are in pixels. The lower plots *(b, d)* display cumulative displacements, both in mm. *(a, b)* were obtained applying the previous approach whereas *(c, d)* were obtained applying the new approach. Using the former algorithm, the final estimate was 0.568 mm. Conversely, the non-redundant Doppler ensemble and the optimal skip size provided a final estimate of 0.9136 mm.
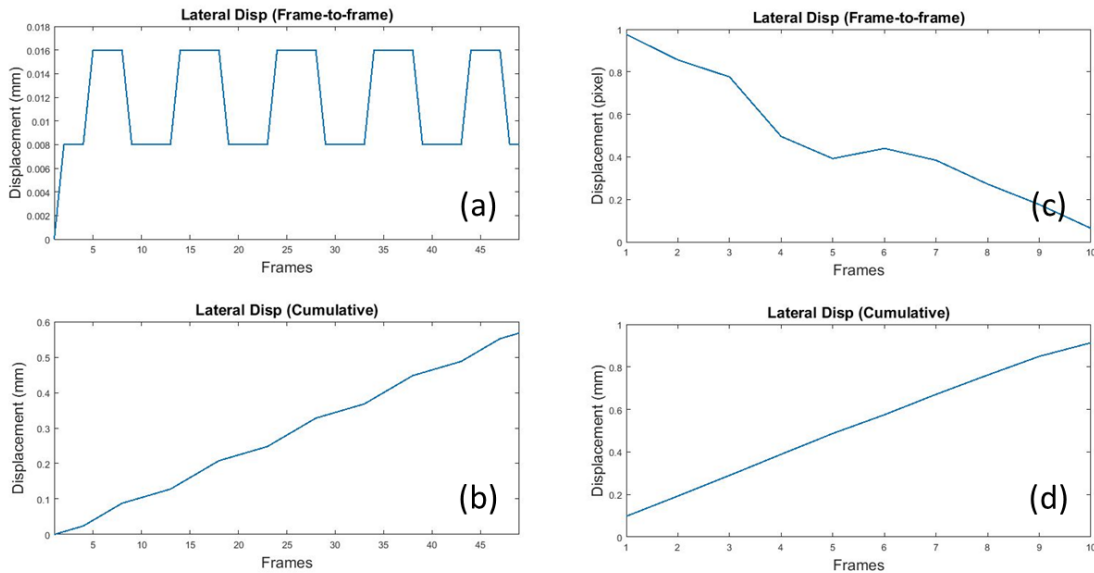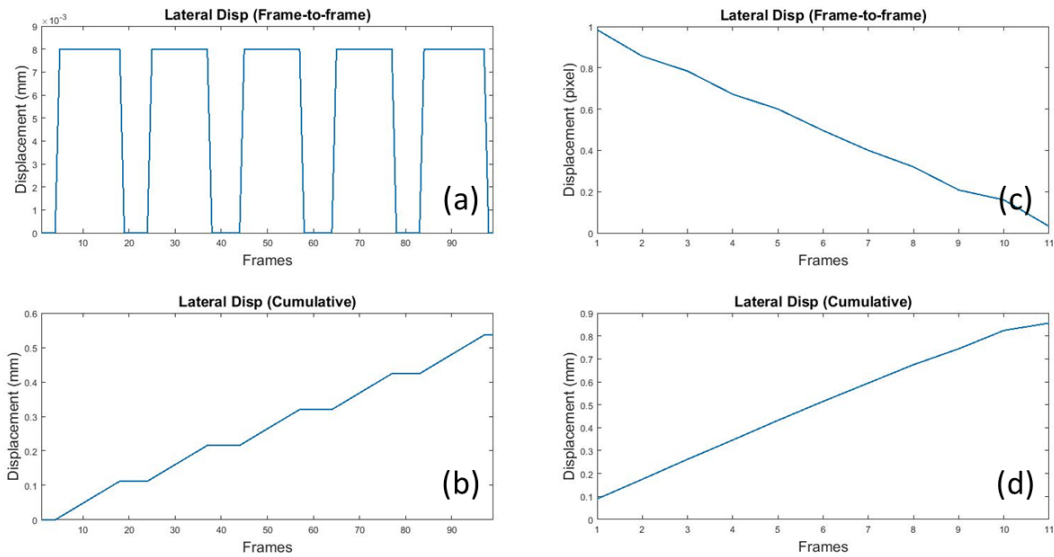

Figure 6.15 Displacement estimates. (a, c) frame-to-frame displacement; (b, d) cumulative displacement; (a, b) full ensemble, skip size equal to 1; (c, d) non-redundant ensemble, customized frame intervals.

Figure 6.16 shows the displacement estimates for a Doppler ensemble of 100 frames. The upper plots *(a, c)* display the frame-to-frame displacements. Estimates in *(a)* are in mm, whereas, those in *(c)* are in pixels. The lower plots *(b, d)* display the cumulative displacements, both in mm. *(a, b)* were obtained applying the previous approach whereas (c, d) were obtained applying the new approach. Using the former algorithm, the final estimate was 0.536 mm. Conversely, the non-redundant Doppler ensemble and the optimal skip size provided a final estimate of 0.8559 mm.

Figure 6.16 Displacement estimates. (a, c) frame-to-frame displacement; (b, d) cumulative displacement; (a, b) full ensemble, skip size equal to 1; (c, d) non-redundant ensemble, customized frame intervals.

Figure 6.17 shows the displacement estimates for a Doppler ensemble of 200 frames. The upper plots *(a, c)* display the frame-to-frame displacements. Estimates in *(a)* are in mm, whereas, those in *(c)* are in pixels. The lower plots *(b, d)* display the cumulative displacements, both in mm. *(a, b)* were obtained applying the previous approach whereas *(c, d)* were obtained applying the new approach. Using the former algorithm, the final estimate was 0.352 mm. Conversely, the non-redundant Doppler ensemble and the optimal skip size provided a final estimate of 0.9046 mm.
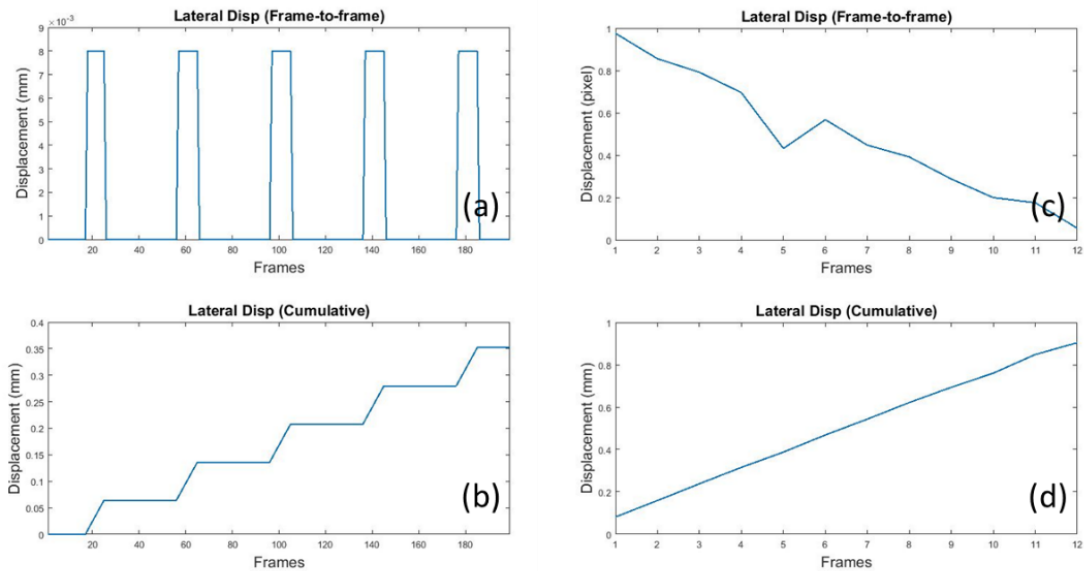
Figure 6.17 Displacement estimates. (a, c) frame-to-frame displacement; (b, d) cumulative displacement; (a, b) full ensemble, skip size equal to 1; (c, d) non-redundant ensemble, customized frame intervals.

Figure 6.18 shows the displacement estimates for a Doppler ensemble of 400 frames. The upper plots *(a, c)* display the frame-to-frame displacements. Estimates in *(a)* are in mm, whereas, those in *(c)* are in pixels. The lower plots *(b, d)* display the cumulative displacements, both in mm. *(a, b)* were obtained applying the previous approach whereas *(c, d)* were obtained applying the new approach. Using the former algorithm, the final estimate was 0.352 mm. Conversely, the non-redundant Doppler ensemble and the optimal skip size provided a final estimate of 0.9046 mm.
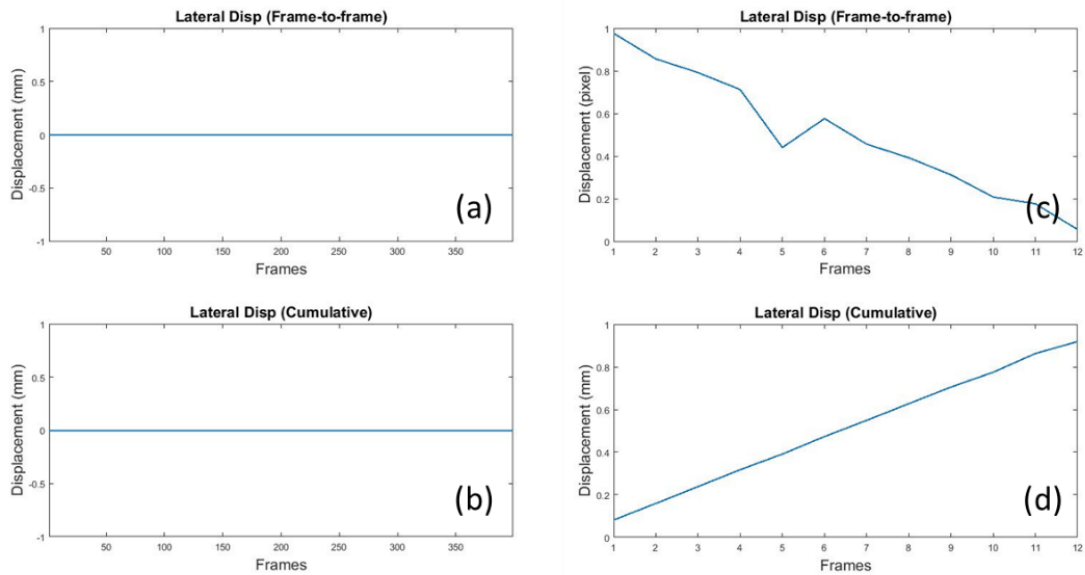
Figure 6.18 Displacement estimates. (a, c) frame-to-frame displacement; (b, d) cumulative displacement; (a, b) full ensemble, skip size equal to 1; (c, d) non-redundant ensemble, customized frame intervals.

Figure 6.19 shows the displacement estimates for a Doppler ensemble of 800 frames. The upper plots *(a, c)* display the frame-to-frame displacements. Estimates in *(a)* are in mm, whereas, those in *(c)* are in pixels. The lower plots *(b, d)* display the cumulative displacements, both in mm. *(a, b)* were obtained applying the previous approach whereas *(c, d)* were obtained applying the new approach. Using the former algorithm, the final estimate was 0.0 mm. Conversely, the non-redundant Doppler ensemble and the optimal skip size provided a final estimate of 0.9185 mm.
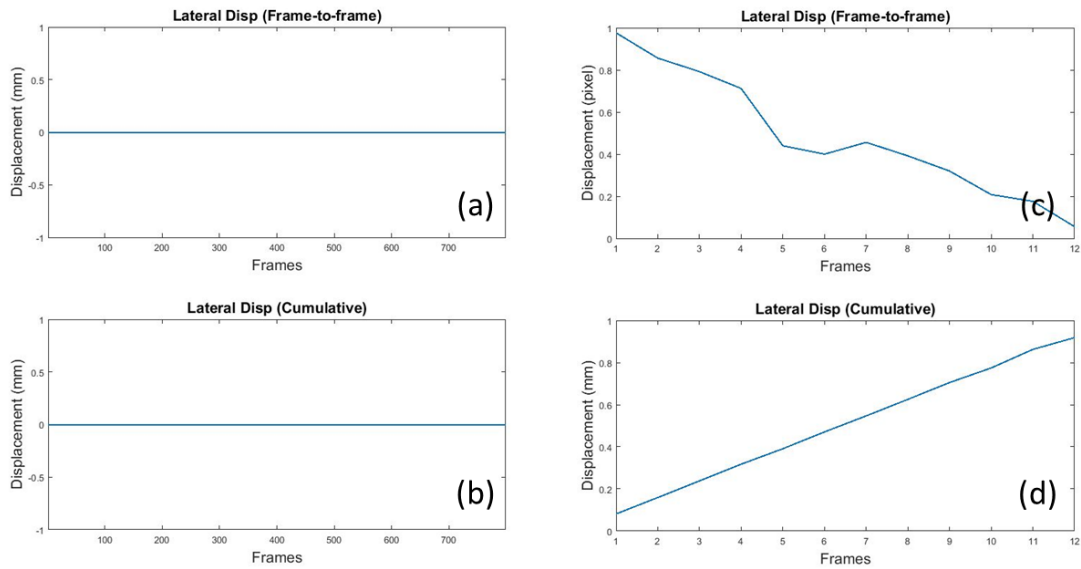
Figure 6.19 Displacement estimates. (a, c) frame-to-frame displacement; (b, d) cumulative displacement; (a, b) full ensemble, skip size equal to 1; (c, d) non-redundant ensemble, customized frame intervals.

Figure 6.20 shows the displacement estimates for a Doppler ensemble of 1600 frames. The upper plots *(a, c)* display the frame-to-frame displacements. Estimates in *(a)* are in mm, whereas, those in *(c)* are in pixels. The lower plots *(b, d)* display the cumulative displacements, both in mm. *(a, b)* were obtained applying the previous approach whereas *(c, d)* were obtained applying the new approach. Using the former algorithm, the final estimate was 0.0 mm. Conversely, the non-redundant Doppler ensemble and the optimal skip size provided a final estimate of 0.9194 mm.
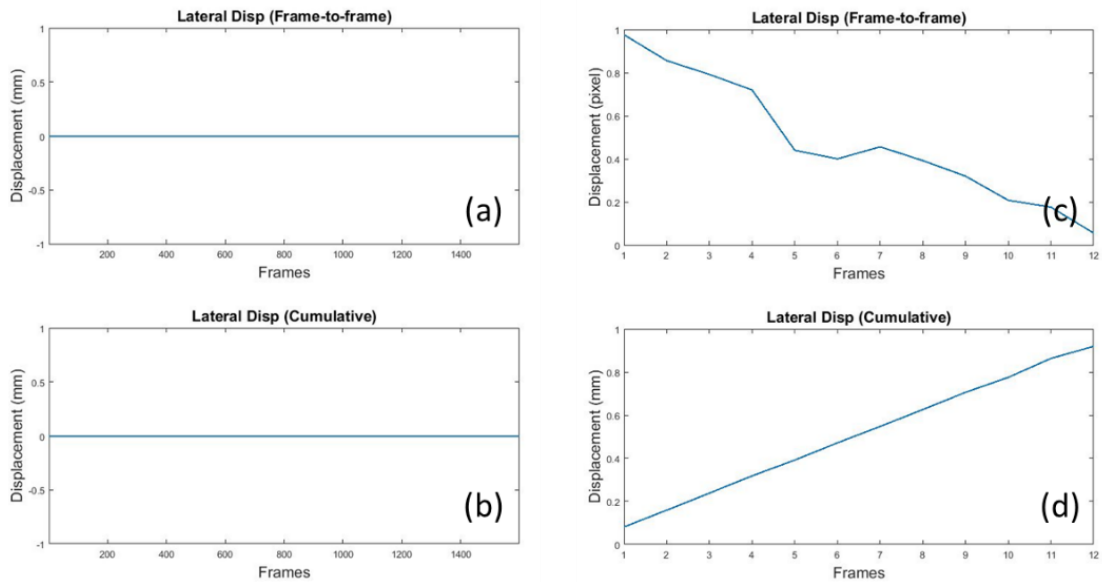
Figure 6.20 Displacement estimates. (a, c) frame-to-frame displacement; (b, d) cumulative displacement; (a, b) full ensemble, skip size equal to 1; (c, d) non-redundant ensemble, customized frame intervals.

In *figure 6.21 (a, c, e, g, i, k)* are the motion matrices computed after motion correction of the non-redundant ensembles, MM No Red Moco. *(b, d, f, h, j, l)* are the motion matrices computed after motion correction, MM Post, of the full Doppler ensembles of 50, 100, 200, 400, 800 and 1600 frames, respectively.
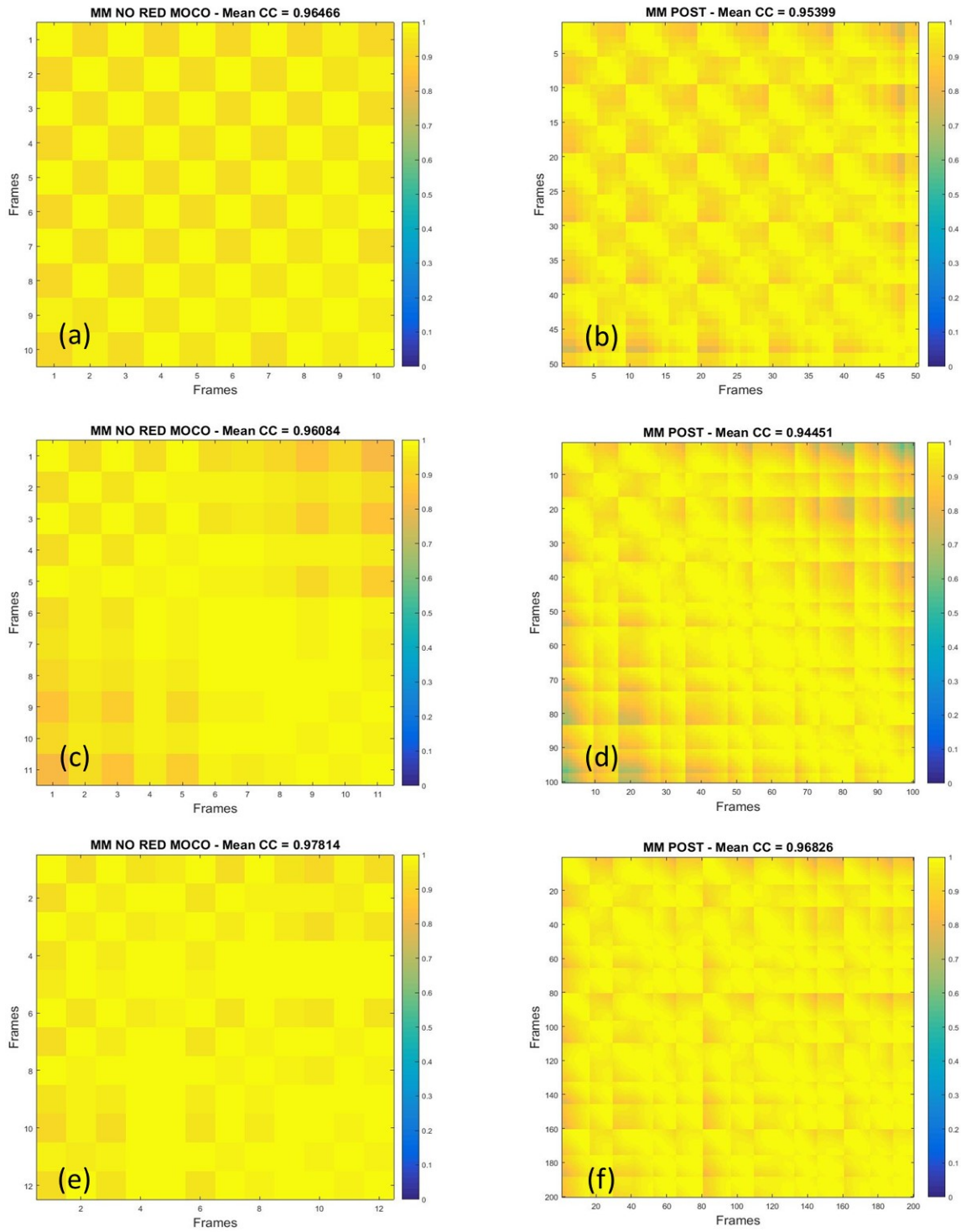
Figure 6.21 Motion matrices and associated mean correlation coefficients computed after motion correction of the non-redundant, MM No Red Moco, (a, c, e) and full, MM Post, (b, d, f) Doppler ensembles.
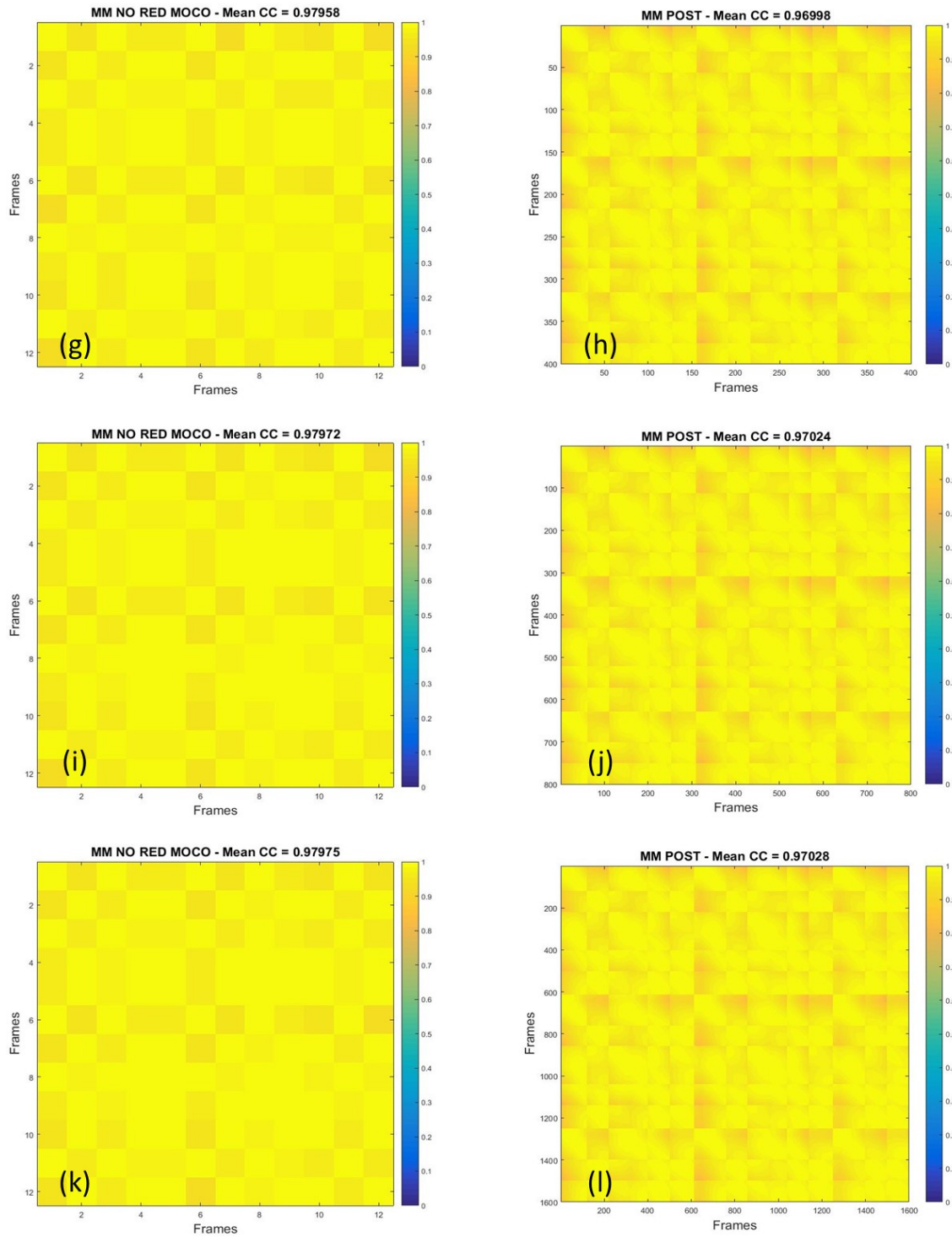
Figure 6.21 Motion matrices and associated mean correlation coefficients computed after motion correction of the non-redundant, MM No Red Moco, (g, i, k) and full, MM Post, (h, j, l) Doppler ensembles.

Figure 6.22 (a-f) illustrates the motion matrices, for ensembles of different size, computed after motion correction using the former algorithm. These motion matrices are referred to as MM Post*. The values of the mean correlation coefficient for Doppler ensembles of 400, 800 and 1600 frames were unaltered compared to those obtained before motion correction because of the null displacement estimations. Slightly differences were addressed to noise related issues.
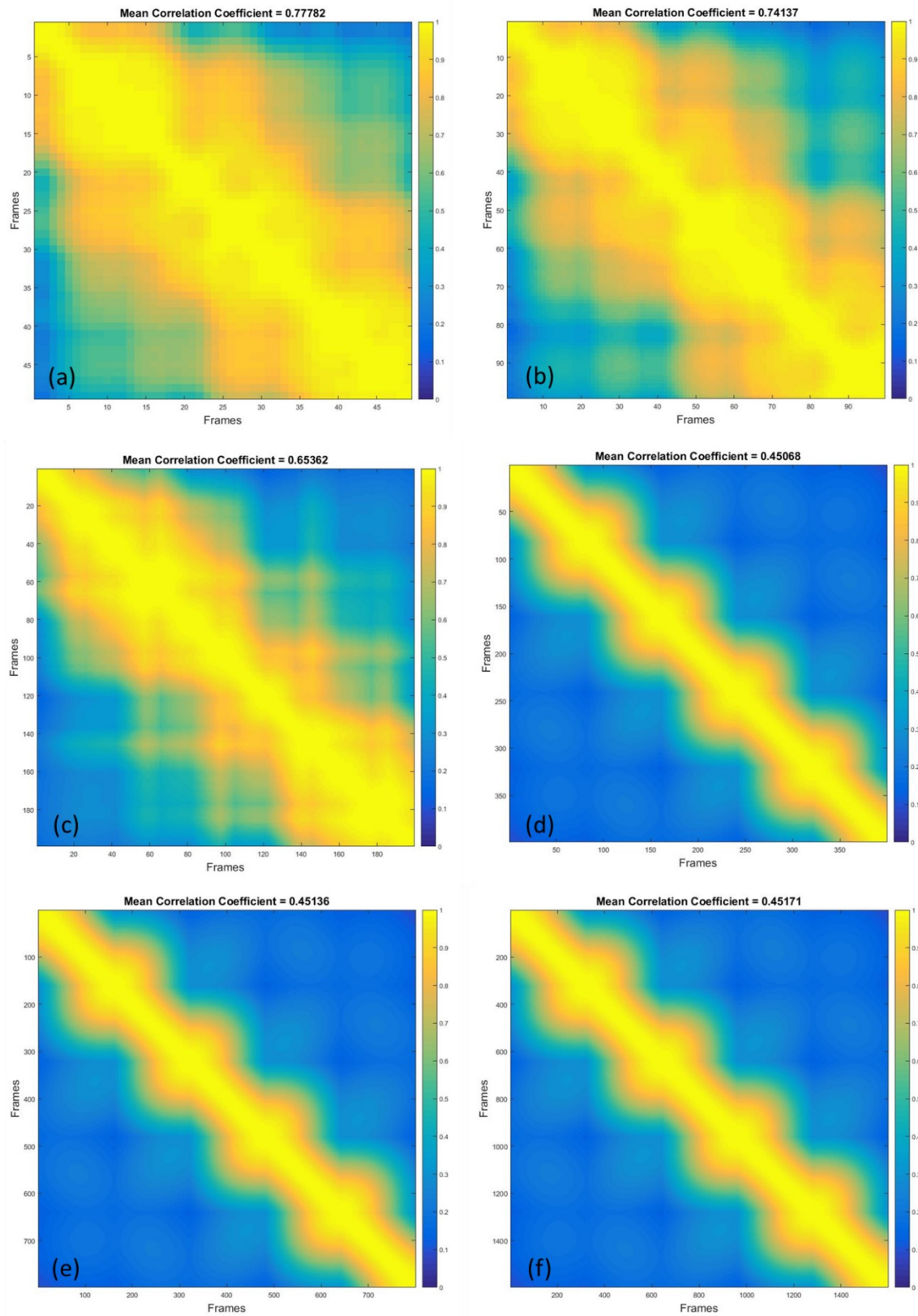
Figure 6.22 MM Post* and associated mean correlation coefficients after performed motion correction using the former algorithm, for Doppler ensembles of: (a) 50 frames, (b) 100 frames, (c) 200 frames, (d) 400 frames, (e) 800 frames and (f) 1600 frames.

Table 6.2 synthetizes the values of the mean correlation coefficient of MM pre, MM No Red, MM No Red Moco, MM Post and MM Post* for all Doppler ensembles. As noticeable, MM Post showed higher mean correlation coefficients than MM Post* for all the ensemble sizes.

Table 6.2 Mean correlation coefficients associated to the Doppler ensembles. Numbers on the brackets indicates the number of frames in the non-redundant ensembles associated to the original ones.

	Mean Correlation Coefficients				
Ensemble Size	MM Pre	MM No Red	MM No Red Moco	MM Post	MM Post*
50 (11)	0.43498	0.43498	0.96466	0.95399	0.77782
100 (12)	0.44339	0.44339	0.96084	0.94451	0.74137
200 (13)	0.44769	0.44769	0.97814	0.96826	0.65362
400 (13)	0.44986	0.44986	0.97958	0.96998	0.45068
800 (13)	0.45095	0.45095	0.97972	0.97024	0.45136
1600 (13)	0.45022	0.4515	0.97975	0.97028	0.45171

6.1.3 Instance of Periodic Motion

The proceeding subsection includes results obtained for an instance of periodic motion, realized as a combination of multiple lateral displacements of 5 pixels or 1 mm on a Doppler ensemble of 1800 frames.

The motion matrix before motion correction, MM Pre, is shown in *figure 6.23*. Correlation moved alongside axes and motion was repeated every 200 frames. The mean correlation coefficient was 0.31433.
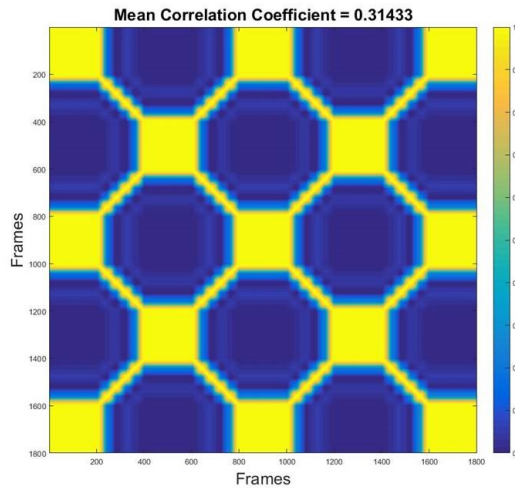
Figure 6.23 MM pre and mean correlation coefficient for a simulated motion of 1 mm, or 5 pixels, repeated every 200 frames in a Doppler ensemble of 1800 frames.

Figure 6.24 displays the motion matrix and the mean correlation coefficient of the non-redundant ensemble, MM No Red. After highly correlated frames rejection, periodicity was removed and thus correlation moved in diagonal. The new ensemble of 21 frames showed a mean correlation coefficient of 0.29958.
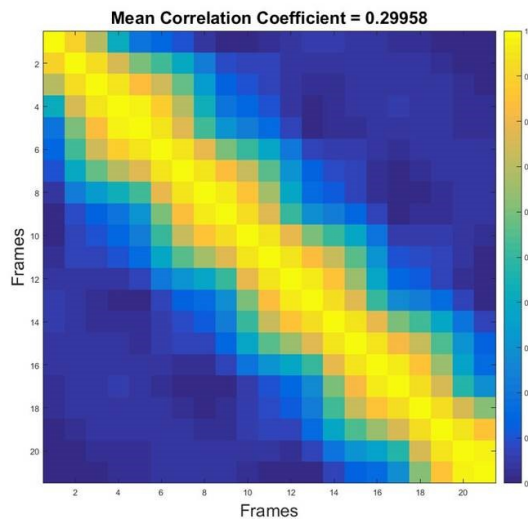

Figure 6.24 MM No Red and mean correlation coefficient.

A graphical representation of the optimal skip sizes associated to the frames of the non-redundant ensemble is given in *figure 6.25.*
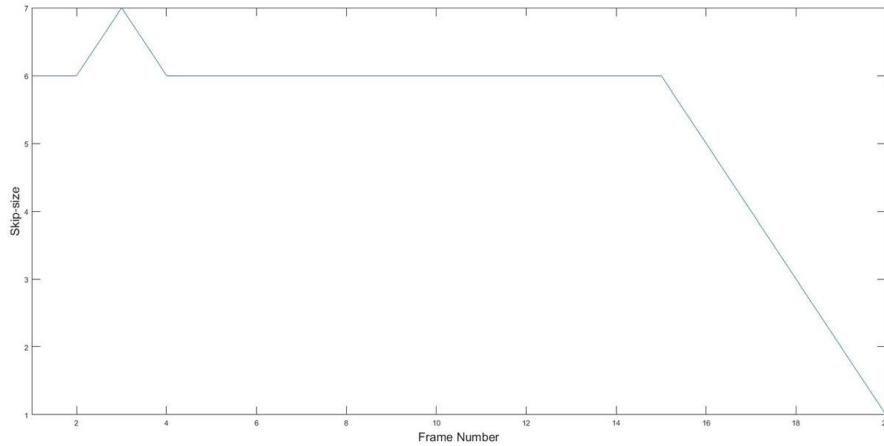
Figure 6.25 Customized inter frame intervals.

Figure 6.26 illustrates the displacement estimates for the Doppler ensemble. The upper plots *(a, c)* display the frame-to-frame displacements. Estimates in *(a)* are in mm, whereas, estimates in *(c)* are in pixels. The lower plots *(b, d)* display the cumulative displacements, both in mm. *(a, b)* were obtained applying the former algorithm whereas *(c, d)* were obtained applying the new optimized one. When the ensemble was reduced, periodic displacements became just translational displacements. That justified the different trends between *(a, b)* and *(c,d)*.
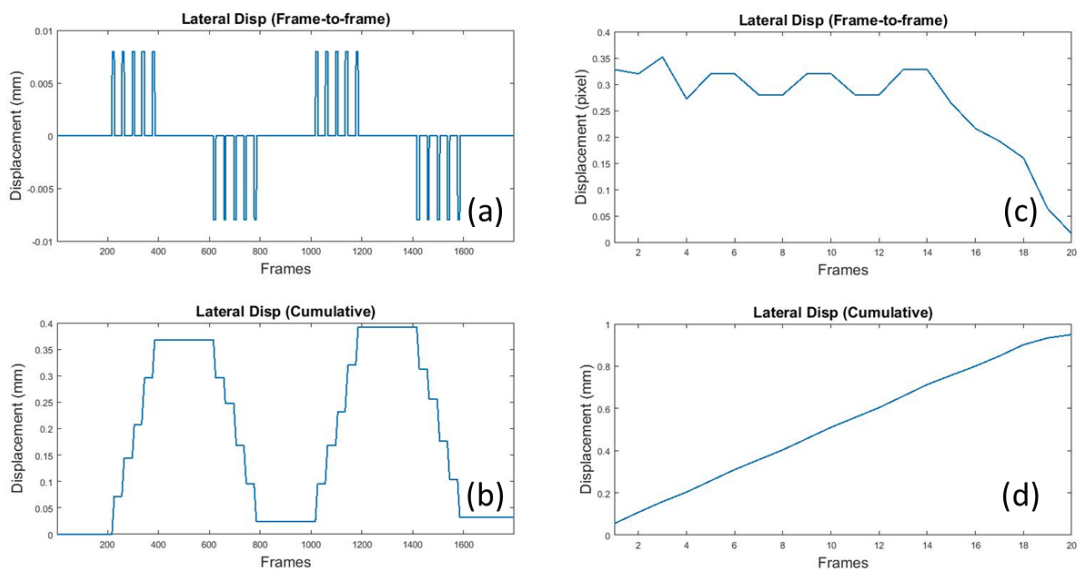

Figure 6.26 Displacement estimates. (a, c) frame-to-frame displacement; (b, d) cumulative displacement; (a, b) full ensemble, skip size equal to 1; (c, d) non-redundant ensemble, customized frame intervals.

Figure 6.27 (a) displays the motion matrix obtained after motion correction was performed on the non-redundant ensemble; *figure x26 (b)* shows the motion matrix after motion correction of the full ensemble.
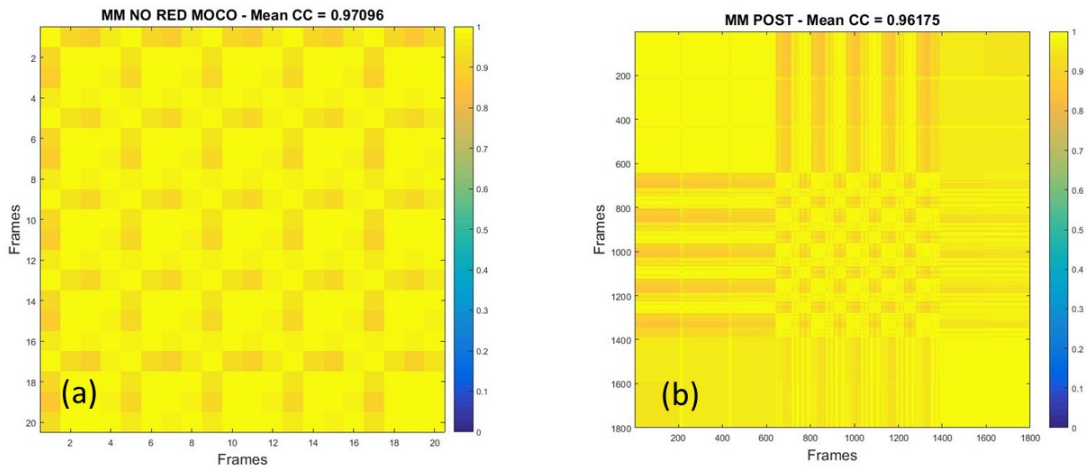

Figure 6.27 (a) MM No Red Moco and mean correlation coefficient; (b) MM Post and mean correlation coefficient.

The motion matrix in *figure 6.28* illustrates motion matrix, MM Post*, and mean correlation coefficient obtained applying the previous motion correction algorithm.
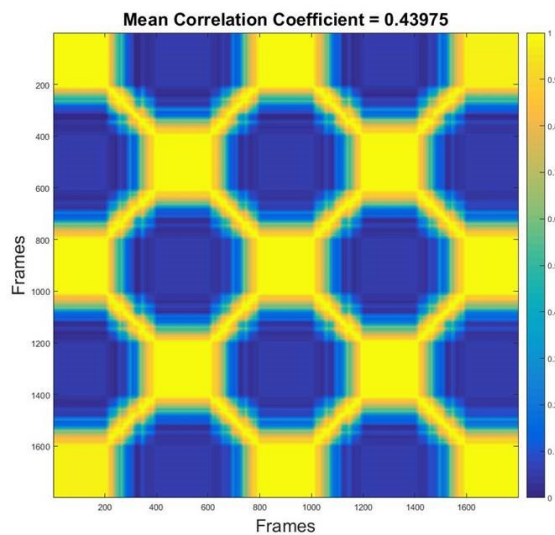

Figure 6.28 Motion Matrix after motion correction, attained applying the former algorithm.

Table 6.3 synthetizes the values of the mean correlation coefficient of MM pre, MM No Red, MM No Red Moco, MM Post and MM Post* for the analyzed instance of periodic motion. As noticeable, MM Post showed higher mean correlation coefficients than MM Post*.

Table 6.3 Mean correlation coefficients. The value between brackets indicates the number of frames in the non-redundant ensemble.

Mean Correlation Coefficients					
Ensemble Size	MM Pre	MM No Red	MM No Red Moco	MM Post	MM Post*
1800 (21)	0.31433	0.29958	0.97096	0.96175	0.43975

6.2 In Vivo Results

Figure 6.29 shows the motion matrices before *(a, b)* and after *(c, d)* motion correction for the full *(a, d)* and non-redundant *(b, c)* Doppler ensembles, obtained from patient 1. X28 *(a)* provided a qualitative descriptor of the thyroid gland motion. The large pulsating motion of the carotid artery can be observed in the black boxes. The non-redundant motion corrected Doppler ensemble showed a mean correlation coefficient equal to 0.91324. However, because of interpolation error, the full-ensemble mean correlation coefficient was 0.84319. The noticeably increased similarity among frames proved the efficacy of the motion correction performance. Specifically, after motion correction PD signals were well aligned and coherently integrated. This improved signal strength and minimized motion artifacts in the PD images.
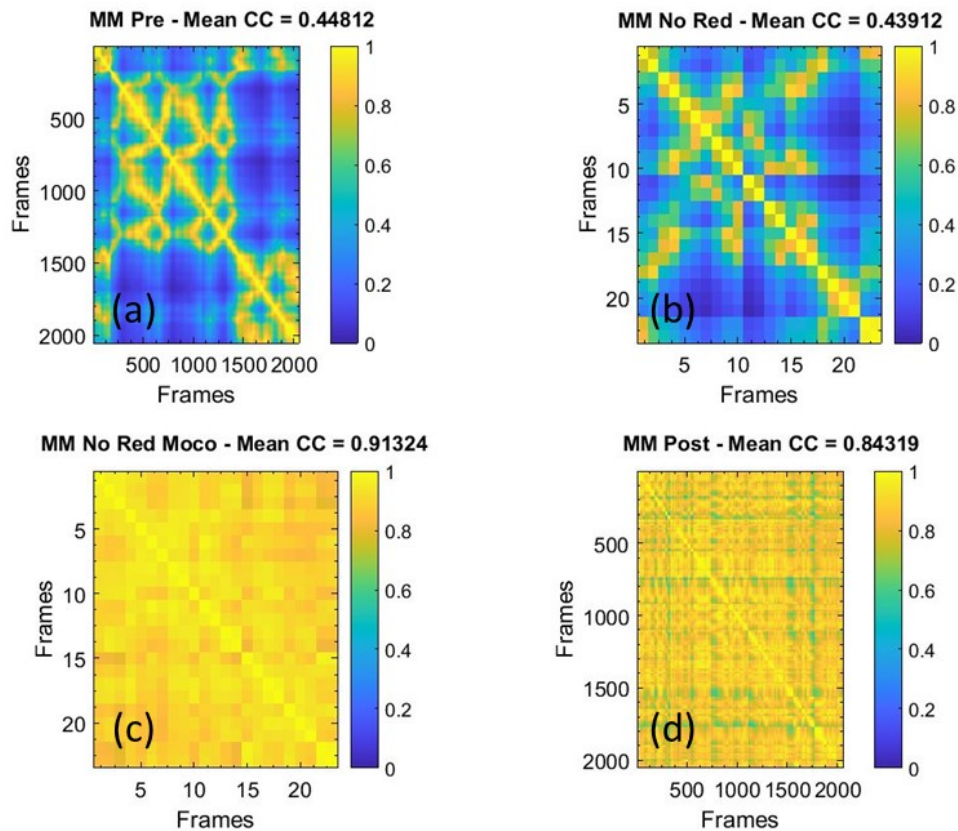
Figure 6.29 Motion matrices and mean correlation coefficients. (a) MM Pre, (b) MM No Red, (c) MM No Red Moco, (d) MM Post.

Figure 6.30 (a) shows the B-mode sonogram of thyroid gland from patient 1. Specifically, the B-mode image was computed from the IQ data using the standard Hilbert function in Matlab. The corresponding PD images obtained without and with motion correction are in figure *6.30 (b)* and *6.30 (d)*, respectively. *6.30 (c)* and *6.30 (e)* display background-suppressed PD images before and after motion correction. The results indicated that the motion-corrected PD image *(d)* noticeably improved the visualization of the small vessels compared with that of the non-motion-corrected image *(b)*. These observations were consistent with previously reported studies involving contrast agent micro-bubbles that used a similar motion correction technique to improve visualization of renal micro vessels in rats *(Foiret, 2017; Hingot, 2017).* Motion induced signal distortion, blurring and appearance of shadow vessel that corrupted the PD image were considerably reduced upon motion correction. However, the background noise bias *(d)* increased with depth and severely impacted the visualization of blood vessels. Specifically, the large dynamic

range of the background noise field saturated the display, preventing blood flow visualization since the later has a relatively smaller dynamic range. Background-suppressed PD image *(e)* showed improved noise suppression, which allowed a better visualization of blood flow, without affecting vessel morphology.
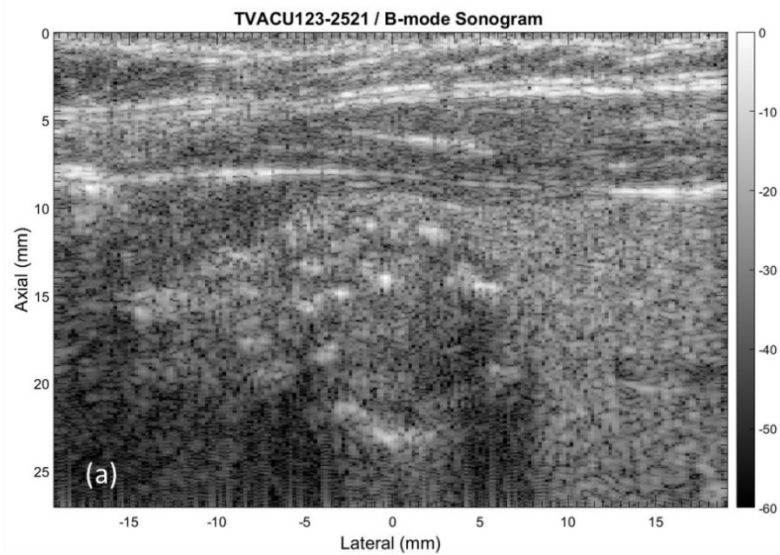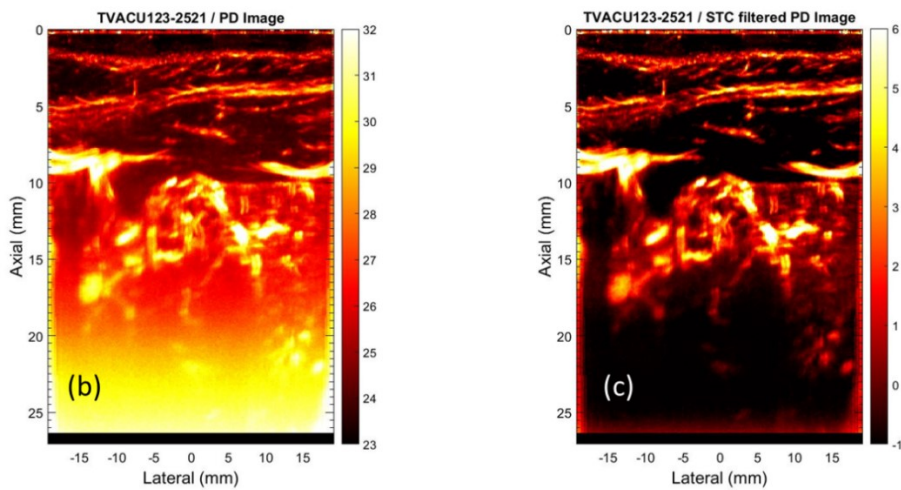
Figure 6.30 (a) B-mode sonogram, (b) PD image without motion correction, (c) STC filtered PD image without motion correction, (d) PD image with motion correction, (e) STC filtered PD image with motion correction.

Figure 6.31 illustrates the motion matrices before (a, b) and after (c, d) motion correction for the full (a, d) and non-redundant (b, c) Doppler ensembles, obtained from patient 1. 6.31 (a) provided a qualitative descriptor of the thyroid gland motion. The non-redundant motion corrected Doppler ensemble showed a mean correlation coefficient equal to 0.9057. The final full-ensemble mean correlation coefficient was 0.87587.

TVACU181-3619
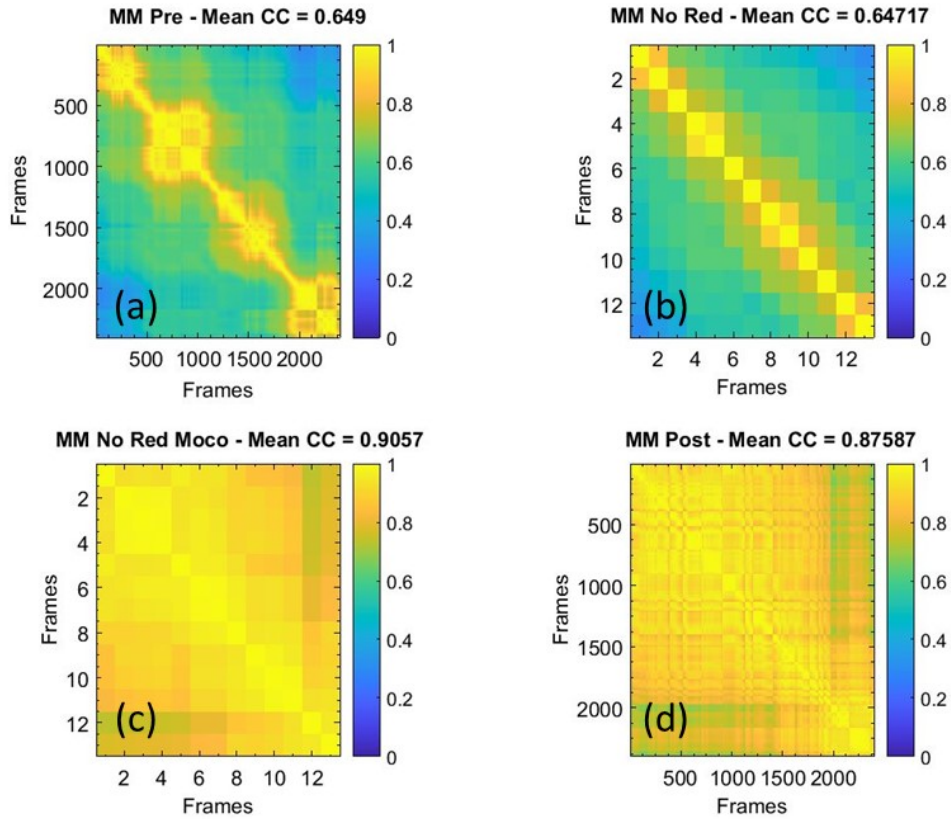
Figure 6.31 Motion matrices and mean correlation coefficients. (a) MM Pre, (b) MM No Red, (c) MM No Red Moco, (d) MM Post.

Figure 6.32 (a) shows the B-mode sonogram of thyroid gland from patient 2. The PD images obtained without and with motion correction are in figure 6.32 (b) and 6.32 (d), respectively. 6.32 (c) and 6.32 (e) display background-suppressed PD images before and after motion correction. The motion-corrected PD image (d) noticeably improved the visualization of thyroid microvasculature compared with that of the non-motion-corrected image (b). Background-suppressed PD image (e) displayed improved noise suppression, which allowed a better visualization of blood flow, with the vascular features preserved.
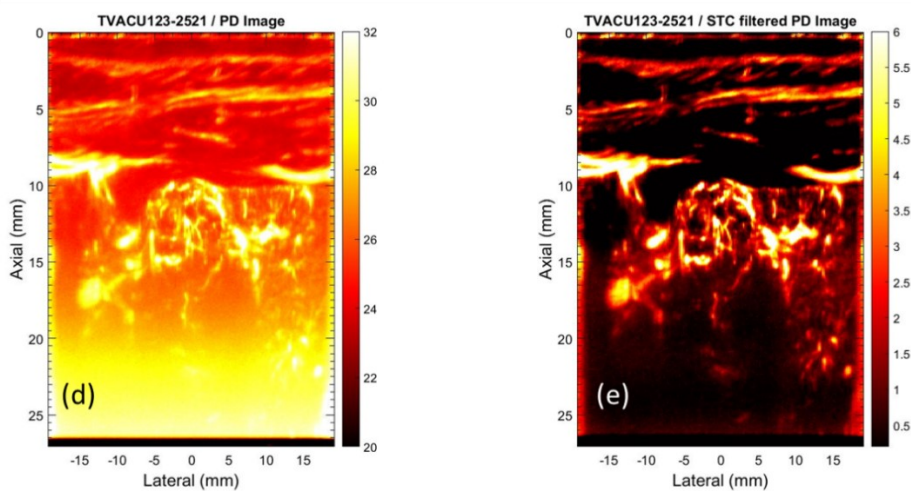
Figure 6.32 (a) B-mode sonogram, (b) PD image without motion correction, (c) STC filtered PD image without motion correction, (d) PD image with motion correction, (e) STC filtered PD image with motion correction.

Discussion

Imaging of microvascular pathways plays a significant role in detection and diagnosis of metastasis of cancerous masses in human thyroid. Contrast-free ultrasound based Doppler blood flow imaging appears to be p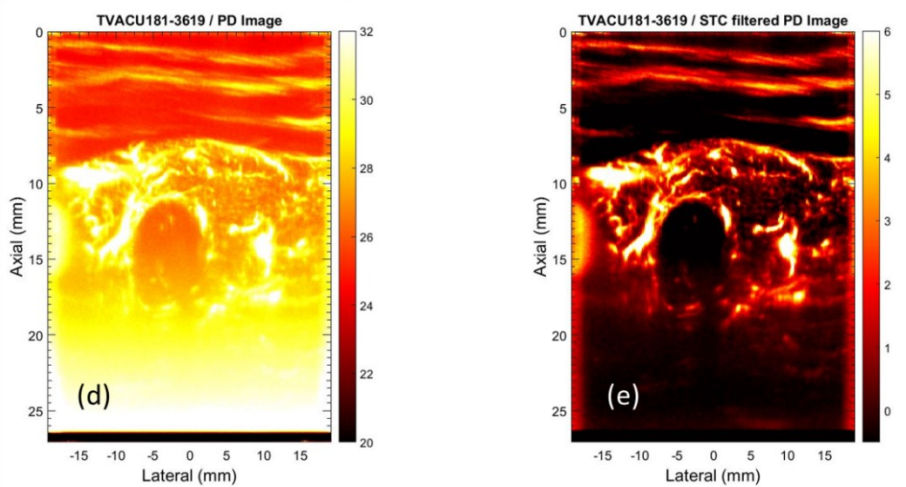otentially useful to reduce the large number of FNA benign findings of suspicious thyroid nodules. However, in thyroid applications, the large pulsatile motion induced by the proximal carotid artery can significantly limit the visualization of small vessels blood flow.

Recent studies have demonstrated that SVD-based spatio-temporal clutter filtering of ultrasonic data acquired at ultrafast frame rate can be more effective in detection of slow blood flow and rejection of moving tissues than conventionally used frequency-based filters *(Demanè, 2015; Baranger, 2018)*. Indeed, ultrafast acquisition enables tissue components to acquire low rank in the Casorati matrix because of its higher spatial and temporal coherence compared with the incoherent blood flow.

However, large motion - which is unavoidable in thyroid imaging - can increase the rank of the tissue components, and thus, a higher SV threshold could be necessary to efficiently suppress tissue clutter *(Nayak, 2018)*. Furthermore, estimation of the cumulated PD signal from the motion affected clutter filtered data can be demanding because of the miss-registration of the ultrasound frames in the Doppler ensemble *(Nayak, 2018)*.

To address these issues, Nayak et al. proposed to estimate thyroid motion as components of axial and lateral displacements using a 2D NCC - based speckle tracking of the Doppler ensemble, prior to SVD clutter filtering *(Nayak, 2018)*. Initial promising and encouraging results on ten human subjects with thyroid nodules suspicious of malignancy suggested and warrant further developments and more *in vivo* validation.

Thus, the present study aimed to the optimization of the motion correction procedure in contrast-free PD ultrasound small vessels imaging of human thyroid.

Specifically, the goal of this study was to evaluate the feasibility of using proper reduced non-redundant ensembles to track small-inter frame displacements, whose quantitative estimation could be challenging because of the poor lateral resolution of ultrasonic images.

That hypothesis was corroborated by applying a rigid body-based motion correction technique on phantom and in vivo data. Specifically, non-redundant Doppler ensembles were generated by rejecting couples of frames displaying a CC above a certain threshold. Then, a 2D NCC-based speckle tracking algorithm was used to estimate tissue displacements, which were subsequently used for motion correction. Specifically, motion correction of the non-redundant Doppler ensemble was performed by globally shifting the rows and columns by the estimated displacements. The original full Doppler ensemble was then corrected by clustering twin frames together. Finally, PD images associated to the in vivo data were obtained by suppressing the estimated noise field in the original PD images. The Motion Matrix was computed at each step and used as a quantitative descriptor of displacement tracking accuracy and motion correction efficacy.

Increased values of mean CC after motion correction in phantom instances guaranteed the efficiency of the proposed optimized technique in detecting small inter-frame displacements and encouraged its validation on the in vivo dataset.

The results from the in vivo study *(figures 6.30, 6.32)* indicated that the motion-corrected PD images importantly improved the visualization of the small vessels. In fact, motion induced signal distortion, blurring and appearance of shadow vessel were considerably reduced upon motion correction. In addition, background-suppressed PD images showed improved noise suppression, which allowed a better visualization of blood flow, without affecting vessel morphology.

As clearly visible, the suspicious nodule of patient 1 was characterized by a predominant central vascular distribution. This worried it was malignant. Conversely, the suspicious nodule of patient 2 showed a peripheral vascular distribution, suggesting it was benign. The FNA biopsies confirmed.

Although further in vivo validation in a larger dataset is needed, these first outcomes suggested that motion-corrected PD imaging could effectively detect tumor malignancy by assessing vessels distribution.

Conclusion

In the present thesis, an upgraded motion-corrected spatiotemporal clutter filtering technique was proposed. The advanced algorithm reliably tracked and corrected small inter-frame displacements, therefore enhancing the visualization of small vessels blood flow in thyroid glands. The improvement in image quality upon motion correction and noise suppression was significant for all the patients, both qualitatively *(figures 6.30, 6.32)* and quantitatively *(figures 6.29, 6.31)*. In the contest of contrast-free PD imaging, these outcomes are particularly valuable since physiological motion can easily corrupt the low intensity of flow signal. These preliminary but encouraging results suggested that motion-corrected PD ensembles could effectively assess thyroid malignancy based on intranodular and peripheral vascularity. Nevertheless, further investigations and in vivo validations are recommended.

Acknowledgements

My deep gratitude goes first to my Italian Mentor Dr. Lorenzo Scalise, who expertly guided me through my graduate education.

Secondly, I would like to thank my Mayo Mentors, Dr. Mostafa Fatemi and Dr. Azra Alizad, for their valuable guidance and support for completion of this project.

Lastly, I would like to express a special thanks to Dr. Rohit Nayak for his constant supervision and for always listening and giving me words of encouragement.

References

Appetecchia M., And Solivetti F., "The Association Of Colour Flow Doppler Sonography And Conventional Ultrasonography Improves The Diagnosis Of Thyroid Carcinoma", Hormone Res. Paediatrics Vol.66, Pp.249–256, 2006.

Akiyama J., Hayama A., And Nakajima M., "Movement Analysis Of Soft Tissues By Speckle Patterns' Fluctuation", JSUM Proceeding, Pp. 615-616, Oct. 1986.

Akiyama J., Nakajima N., And Yuta S., "Movement Analysis Using B-Mode Images", Acoustic Imaging, Vol. 17, Pp. 499-505, 1988.

Bae U. et al. "Ultrasound thyroid elastography using carotid artery pulsation", J. Ultrasound Med. Vol. 26, Pp.797–805, 2007.

Baranger J., Arnal B., Perren F., Baud O., Tanter M., And Demene C., "Adaptive Spatiotemporal SVD Clutter Filtering For Ultrafast Doppler Imaging Using Similarity Of Spatial Singular Vectors", IEEE Transactions On Medical Imaging, Vol. 37, No. 7, Jul. 2018.

Bercoff J., Ultrafast Ultrasound Imaging, Ultrasound Imaging – Medical Applications, Prof. Oleg Minin (Ed.), Intech, 2011.

Bercoff J., Chamak-Bercoff J., Fraschini C., Guiffard E., Loupas T., Savery D., et al., "Ultrafast[tm] Doppler", Supersonic Imagine, Aix-En-Provence, France.

Bjærum S., Torp H., And Kristoffersen K., "Clutter Filter Design For Ultrasound Color Flow Imaging", IEEE Transactions On Ultrasonic, Ferroelectrics, And Frequency Control, Vol.49, No. 2, Pp. 204-216, Feb. 2002.

Bjærum S., Torp H., "Optimal Adaptive Clutter Filtering In Color Flow Imaging", IEEE Ultrasonic Symposium Proceedings, Vol. 2, Pp. 1223-1226, 1997.

Bjærum S., Torp H., And Kristoffersen K., "Clutter Filters Adapted To Tissue Motion In Ultrasound Color Flow Imaging", IEEE Transactions On Ultrasonic, Ferroelectrics, And Frequency Control, Vol.49, No. 6, Pp. 693-704, Jun. 2002.

Bjorn A.J. Angelsen, "Ultrsound Imaging, Waves, Signals And Signal Processing", Vol I, Emantec As, Trondheim, Norway, Dec 2000.

Bohs L.N. And Trahey G.E, "A Novel Method For Angle Independent Ultrasonic Imaging Of Blood Flow And Tissue Motion", IEEE Transactions On Biomedical Engineering, Vol. 38, Pp. 271-286, Mar. 1991.

Brunese L. et al., "A New Marker For Diagnosis Of Thyroid Papillary Cancer", J. Ultrasound Med. Vol. 27, Pp.1187–1194 ,2008.

Bude R.O., And Rubin J.M., "Power Doppler Sonography", Radiology, Vol. 200, Pp. 21-23, 1996.

Carmeliet P., And Jain R.K., "Angiogenesis In Cancer And Other Diseases", Nature 407, Pp. 249, 2000.

Cerbone G. et al., "Power Doppler Improves The Diagnostic Accuracy Of Color Doppler Ultrasonography In Cold Thyroid Nodules: Followup Results", Hormone Res. Paediatrics Vol. 52, Pp. 19–24 ,1999.

De Jong P.G.M., Arts T., Hoeks A.P.G., And Reneman R.S., "Determination Of Tissue Motion Velocity By Correlation Interpolation Of Pulsed Ultrasonic Signals", Ultrasound Imaging, Vol. 12, Pp. 84-98, 1990.

Demanè C., Deffieux T., Pernout M., Osmanski B.F., Biran V., Gennisson J.L. et al., "Spatiotemporal Clutter Filtering Of Ultrafast Ultrasound Data Highly Increases Doppler And Fultrasound Sensitivity", IEEE Transactions On Medical Imaging, Vol. 34, No. 11, Pp. 2271-2285, Nov. 2015.

Denarie, B. et al. "Coherent Plane Wave Compounding For Very High Frame Rate Ultrasonography Of Rapidly Moving Targets", IEEE Trans Med Imaging Vol. 32, P.P 1265–76, Https://Doi.Org/10.1109/TMI.2013.2255310, 2013.

Evans D.H., And Mcdicken W.N., Doppler Ultrasound: Physics, Instrumentation And Signal Proceeding, 2nd Edition, West Sussex, 2000.

Evans D.H., "Color Flow Imaging And Motion Imaging", Proc. Imeche Vol.224 Part H: Engineering In Medicine, Special Issue Paper, Pp. 241-253, Apr. 2009.

Foiret J., Zhang H., Ilovitsh T., Mahakian L., Tam S., And Ferrara K.W. "Ultrasound Localization Microscopy To Image And Assess Microvasculature In A Rat Kidney", Scientific Reports Vol. 7 13662, 2017.

Frates M. C., Benson C. B., Doubilet P. M., Cibas E. S., And Marqusee E., "Can Color Doppler Sonography Aid In The Prediction Of Malignancy Of Thyroid Nodules?", J. Ultrasound Med. Vol.22, Pp. 127–131, 2003.

Gardiner W.M., And Fox M.D., "Color-Flow US Imaging Through The Analysis Of Speckle Motion", Radiology, Vol. 172, Pp. 866-868, 1989.

Hein A., O' Brien W.D., "Current Time-Domain Methods For Assessing Tissue Motion By Analysis From Reflected Ultrasound Echoes – A Review". IEEE Transactions Of Ultrasonic, Ferroelectrics, And Frequency Control, Vol.40, No.2, Pp. 84-99, Mar. 1993.

Hingot V., Errico C., Tanter M., And Couture O., "Subwavelength Motion-Correction For Ultrafast Ultrasound Localization Microscopy", Ultrasonics Vol. 77 Pp. 17–21, 2017.

Huntzicker S., Nayak R., Doyley M.M., "Quantitative Sparse Array Vascular Elastography: The Impact Of Tissue Attenuation And Modulus Contrast On Performance", Journal Of Medical Imaging, 2014.

Konofagou E., Ophir J., "A New Elastographic Method For Estimation And Imaging Of Lateral Displacements, Lateral Strains, Corrected Axial Strains And Poisson's Ratios In Tissues", Ultrasound Medicine And Biology, Vol. 24, Pp. 1183-1199, 1998.

Kremkau F. W., Diagnostic Ultrasound. Principles And Instruments, 7th Edition, Saunders Elsevier, Missouri, 2006.

Kruse D.E., And Ferrara K.W., "A New High Resolution Color Flow System Using An Eigendecomposition-Based Adaptive Filter For Clutter Rejection", IEEE Transactions On Ultrasonic, Ferroelectrics, And Frequency Control, Vol.49, No. 12, Pp. 1739-1754, 2002.

Ledoux L.A.F., Brands P.J., And Hoeks A.P.G., "Reduction Of The Clutter Component In Doppler Ultrasound Signals Based On Singular Value Decomposition: A Simulation Study", Ultrasonic Imaging, Vol.19, Pp. 1-18, 1997.

Lovstakken L., Bjærum, Kristoffersen K., Haaverstad R., And Torp H.,"Real-Time Adaptive Clutter Rejection Filtering In Color Flow Imaging Using Power Methods Iterations", IEEE Transactions On Ultrasonic, Ferroelectrics, And Frequency Control, Vol.53, No. 9, Pp. 1597-1608, 2006.

Lu R. et al., "Superb Microvascular Imaging (Smi) Compared With Conventional Ultrasound For Evaluating Thyroid Nodules", BMC Med. Imaging Vol. 17, Pp. 65, 2017.

Luo J., And Konofagou E.E., "A Fast Normalized Cross-Correlation Calculation Method For Motion Estimation", IEEE Transactions Of Ultrasonic, Ferroelectrics, And Frequency Control, Vol.57, No.6, Pp. 1347-1357, Jun. 2010.

Mace E. et al., "Functional Ultrasound Imaging Of The Brain: Theory And Basic Principles", IEEE Transactions On Ultrasonic, Ferroelectrics, And Frequency Control, Vol. 60, No. 3, Pp. 492-506, Mar. 2013.

Martinoli C., Derchi L.E., Rizzato G.And Solbiati L., "Power Doppler Sonography: General Principles, Clinical Applications, And Future Prospects', European Radiology, Vol. 8, Pp. 1224-1235, 1998.

Mcfarlin B.L., Kumar V., Bigelow T.A., Simpson D.G., White-Traut R.C.,Abramowicz J.S., O'Brien W.D, "Beyond Cervical Length: A Pilot Study Of Ultrasonic Attenuation For Early Detection Of Preterm Birth Risk", Ultrasound Medicine And Biology Vol. 41, Pp. 3023–3029, 2015.

Montaldo G., Tanter M., Bercoff J., Benech N., And Fink M., "Coherent Plane-Wave Compounding For Very High Frame Rate Ultrasonography And Transient Elastography", IEEE Transactions On Ultrasonic, Ferroelectrics, And Frequency Control, Vol.56, No. 3, Pp. 489-506, Mar. 2009.

Namekawa K., Kasai K., Tsukamoto C., And Koyano A., "Real Time Bloodfolw Imaging System Utilizing Autocorrelation Techniques", Ultrasound, Pp. 203-208, 1982.

Nayak, R., Schifitto, G., And Doyley, M. M., "Noninvasive Carotid Artery Elastography Using Multielement Synthetic Aperture Imaging: Phantom And *In Vivo* Evaluation", Medical Physics Vol. 44, Pp. 4068–4082, 2017.

Nayak, R. et al., "Non-Contrast Agent Based Small Vessel Imaging Of Human Thyroid Using Motion Corrected Power Doppler Imaging", Scientific Reports Vol. 8, 15318, 2018.

Nayak, R., Kumar, V., Webb, J., Fatemi, M. And Alizad, A., "Non-Invasive Small Vessel Imaging Of Human Thyroid Using Motion-Corrected Spatiotemporal Clutter Filtering", Ultrasound Medicine And Biology Vol. 45, Pp. 1010–1018, 2019.

Parker J.A., Kenyon R.V., Troxel D.E. "Comparison Of Interpolating Methods For Image Resampling", IEEE Transactions On Medical Imaging, Vol. 2, Pp. 31–39, 1983.

Powalawski T., "Ultrasonic System For Noninvasive Measurement Of Hemodynamic Parameters Of Human Arterial Vascular System", Archives Of Acoustics, Vol. 13, No. 1-2, Pp. 89-108, 1988.

Ramamurthy B.S. And Trahey G.E, "Potential And Limitations Of Angle-Independent Flow Detection Algorithms Using Radio-Frequency And Detected Echo Signals", Ultrasonic Imaging, Vol. 13, Pp. 252-268, 1991.

Robinson D.E., Chen F., And Wilson L.S., "Measurement Of Velocity Of Propagation From Ultrasonic Pulse-Echo Data", Ultrasound In Medicine And Biology, Vol. 8, No. 4, Pp. 413-420, 1983.

Rubin J.M., And Adler R.S, "Power Doppler Expands Standard Color Capability", Diagnostic Imaging, Vol. 12, Pp. 66-69, 1993.

Rubin J.M., Bude R.O, Carson P.L., Bree R.L., And Adler R.S., "Power Doppler US: A Potentially Useful Alternative To Mean Frequency-Based Color Doppler US", Radiology, Vol.190, Pp. 853-856, 1994.

Saslow D. et al., "American Cancer Society Guidelines For Breast Screening With MRI As An Adjunct To Mammography", CA: A Cancer Journal For Clinicians Vol. 57, Pp. 75–89, 2007.

Trahey G.E.,. Allison J.W, And Von Ramm O.T., "Angle Independent Ultrasonic Detection Of Blood Flow", IEEE Transactions On Biomedical Engineering, Vol. BME-34, Pp. 965-967, Dec. 1987.

Trahey G.E., Hubbard S.M., And. Von Ramm O.T, "Angle Independent Ultrasonic Blood Flow Detection By Frame-To-Frame Correlation Of B-Mode Images", Ultrasonic, Vol. 26, Pp. 271-276, Sept. 1988.

Tysoe C.And Evans D.H., "Bias In Mean Frequency Estimation Of Doppler Signals Due To Wall Clutter Filters", Ultrasound In Medicine And Biology, Vol. 29, No. 5, Pp. 671-677, 1995.

Vaupel P., Kallinowski F., And Okunieff P. "Blood Flow, Oxygen And Nutrient Supply, And Metabolic Microenvironment Of Human Tumors: A Review ", Cancer Res. 49, Pp. 6449–65, 1989.

Willemetz J.C., Nowicki A., Meister J.J., De Palma F., And Pante G., "Bias And Variance In The Estimate Of The Doppler Frequency Induced By A Wall Motion Filter", Ultrasonic Imaging, Vol. 11, No. 2, Pp. 215-225, Jun. 1989.

Yu A.C.H.,. Cobbold R.S.C, "A New Eigen-Based Clutter Filter Using Hankel-SVD Approach", IEEE Ultrasonic Symposium Proceedings, Pp. 1079-1082, 2006.

Yu A.C.H., And Lovstakken L., "Eigen-Based Clutter Filter For Color Flow Imaging: Single Ensemble Vs. Multi-Element Approaches", IEEE Ultrasonic Symposium Proceedings, Pp. 1101-1104, 2007.

Yu A.C.H., Cobbold R.S.C., "A New Eigen-Based Clutter Filter Using Hankel-SVD Approach", IEEE Ultrasonic Symposium Proceedings, Pp. 1079-1082, 2006.

Zahiri-Azar R., Salcudean S.E., "Motion Estimation In Ultrasound Images Using Time Domain Cross Correlation With Prior Estimates", IEEE Transactions On Biomedical Engineering, Vol. 53, Pp. 1990-2000, No. 10, Oct.2006.